Characterization of iron oxide thin films as a support for catalytically active nanoparticles

Dissertation

zur Erlangung des Grades

Doktor der Naturwissenschaften (Dr. rer. nat.)

eingereicht im Fachbereich Physik
der Freie Universität Berlin

Vorgelegt in Mai 2013 von

Alessandro Sala

1. Gutachter: Prof. Dr. Hans-Joachim Freund
2. Gutachter: Prof. Dr. Paul Fumagalli

Tag der Disputation: 24 Juni 2013

Hierdurch versichere ich, dass ich in meiner Dissertation alle Hilfsmittel und Hilfen angegeben habe und versichere gleichfalls auf dieser Grundlage die Arbeit selbstständig verfasst zu haben.

Die Arbeit habe ich nicht schon einmal in einem früheren Promotionsverfahren verwendet und ist nicht als ungenügend beurteilt worden.

Berlin, 8. Mai 2013

Diese Arbeit wurde von Juli 2008 bis April 2013 am Fritz-Haber-Institut der Max-Planck-Gesellschaft in der Abteilung Chemische Physik unter Anleitung von Prof. H.-J. Freund angefertigt

Acknowledgements

My biggest and sincerest thanks go to Prof. Hans-Joachim Freund for the great opportunity to work in his department. I have really appreciated his competence, his interest in my work, his help and his great patience, especially for a work that took an unexpected amount of time. The proposed project and the opportunity to join the IMPRS have been of great value for my professional and personal growth. I cannot tell how much I praise your support.

Many thanks go to Prof. Paul Fumagalli, which has accepted to be my second supervisor. Thank you for the interest in my work, for your sharp review and for your kindness.

I want to thank particularly Dr. Thomas Schmidt, my team leader, not only for his great competence in physics and his unmatched knowledge of LEEM/PEEM system, but also for teaching me how to make science, collaborate with people, write, analyze and much much more. You have been an example of rigor, tolerance and humanity.

Since the first day I came to the Fritz-Haber-Institut, I received a lot of help from Dr. Helder Marchetto. I really thank him for the time we spent together, at work and elsewhere. I am honored to be your friend.

I cannot forget the other people that were or are in the Spectro-microscopy group: Marcel Springer, Dr. Florian Maier, Dr. Giuseppe Rombolà , Francesca Genuzio, Hagen Klemm and Gina Peschel. Being part of this group has been an honor and a pleasure. Thank you for the help and the smiles you gave me during all this time.

I would like to thank the International Max Planck Research School (IMPRS) for the financial support, helpful block courses and lectures, outstanding workshop and countless opportunities to learn.

I am grateful to Dr. Helmut Kuhlenbeck, Prof. Klaus Heinz and Dr. Lutz Hammer for

their help in the I/V-LEED calculations, to Dr. Shamil Shaikhutdinov and Dr. Zhi-Hui Qin for the help in the Pt nanoparticles project and to Dr. Swetlana Schauermann and Dr. Aditja Savara for the fruitful discussion about iron oxide thin films.

Thanks to the other past and present team leaders at the CP department, Prof. Thomas Risse, Dr. Martin Sterrer, Dr. Markus Heyde and Prof. Niklas Nilius. I have learned a lot from any of you.

I am thankful to Manuela Misch, Gabi Menhert, Bettina Menzel and Daniela Nikolaus, for their invaluable work at the department office and at the IMPRS office.

Special thanks to all the people I have met at the FHI and at the IMPRS, for the friendly atmosphere and the productive environment. Thanks to Laura, Michele, Marco, Fabio, Mariana, Nicola, Mathias, Dagmar, Leo, Steffi, Christine, Thomas, Georg, Esther, Anastasia, Philipp, Kim, Jan-Frederik, Leandro, Christian, Fernando, Rhys, Bill, Andreas, Franziska, Hui-Feng, Yuichi, Sebastian, Wiebke, Jan-Henrik, Aditya, Kalle, Casey, Elena, Osman, Martin, Emre, Irene, Mikolaj, Anibal, Bo Hong, Yulia, Xin and many many more.

During my time in Berlin, I met a lot of extraordinary people; the list would be too long to enunciate here. Thank you for the great time together, I will never forget you all.

Finally, I want to thank my family and my closest friends, in Berlin, in Trieste and spread across the world. They know why I thank them. No distance could affect our bond, now or ever.

Abstract

This work presents a systematic study of $Fe_3O_4(111)$ thin film grown on Pt(111) surface, by applying the powerful capabilities of SMART microscope. With an improved aligning procedure, a lateral resolution of 18 nm in XPEEM could be shown, the worldwide best value achieved up to now. This performance is limited by space-charge phenomena; the origin and the possible interventions to overcome such effect are discussed. With this technical improvement, LEEM, XPEEM, LEED, SPA-LEED, I/V-LEED and XPS methods, as well as LEEM simulations, were applied to characterize $Fe_3O_4(111)$ thin films, with particular attention on the changes induced by the preparation conditions. The films presented christallographic, morphological and surface inhomogeneities; their relation with changes in the preparation conditions is analyzed. Moreover, the layer-by-layer growth enabled by a new preparation recipe allowed a more precise study of the thin film growth. Such recipe creates flatter and more regular $Fe_3O_4(111)$ thin films. Above a certain thickness the film presents several kinds of line defects ascribable as sub-surface dislocations. One particular type, with Burgers vector perpendicular to the surface, contributes to the thin film growth as a growth channel. Furthermore, a study of the rotational domains at the different preparation stages proves that the Fe and O deposition modifies the shape of the rotational domain boundaries. Finally, Pt nanoparticles are deposited on these $Fe_3O_4(111)$ films. Different preparation recipes are tested in real-time and *in-situ*. This approach brought new insight into the strong metal-support interaction and the encapsulation of Pt nanoparticles by a FeO monolayer. A study of Pt deposition at different temperatures suggests that the encapsulation mechanism could be the progressive sinking of the deposited material under the first oxygen layer of the bulk.

Zusammenfassung

Die folgende Arbeit behandelt eine systematische Studie des $Fe_3O_4(111)$ Dünnschichtwachstums auf der Pt(111)-Oberfläche unter Anwendung der beträchtlichen Möglichkeiten, die das SMART-Mikroskop bietet. Durch eine verbesserte Justage konnte eine laterale Auflösung von 18 nm in XPEEM erreicht werden. Diese bislang weltweit beste Auflösung ist durch Raum-Ladungseffekte begrenzt. Ihre Ursprünge und mögliche Lösungansätze, um diesen Effekt zu überwinden, werden diskutiert. Mit diesen technischen Verbesserungen wurden die $Fe_3O_4(111)$ Dünnschichten mit den Methoden LEEM, XPEEM, LEED, SPA-LEED, I/V-LEED und XPS, sowie mit LEEM-Simulationen charakterisiert, wobei ein besonderes Augenmerk dem Einfluss der Präparationsbedingungen galt. Die Filme zeigen kristallographische, morphologische und oberflächliche Inhomogenitäten, deren Zusammenhang mit Änderungen in den Präparationsbedingungen analysiert wird. Darüberhinaus konnte durch das lagenweise Wachstum, ermöglicht durch eine neue Präparationmethode, eine präzissere Studie zum Dünnfilmwachstum durchgeführt werden. Diese Methode führt zu flacheren und gleichmäßigeren $Fe_3O_4(111)$ Filmen. Oberhalb einer bestimmten Dicke weist der Film verschiedene Arten von Liniendefekten auf, beschreibbar als unter der Oberfläche liegende Versetzungen. Ein spezieller Typ, dessen Burgers-Vektor senkrecht zur Oberfläche steht, trägt zum Dünnschichtwachstum als Wachstumskanal bei. Des Weiteren belegt die Untersuchung von Rotationsdomänen bei verschiedenen Präpapationsstufen, dass Fe- und O-Abscheidungen die Form deren Grenzflächen verändern. Zum Abschluss wurden Pt-Nanopartikel unter verschiedenen Präparationsmethoden, in Echtzeit und *in-situ*, auf die $Fe_3O_4(111)$-Filme abgeschieden. Dieses Vorgehen brachte neue Einblicke in die starke Metallsubstrat-Wechselwirkung und die Einkapselung der Pt-Nanopartikel durch FeO Monolagen. Eine Studie zur Pt-Abscheidung bei verschiedenen Temperaturen deutet an, dass der Einkapselungsmechanismus das fortlaufende Absinken des abgeschiedenen Materials unter die oberste Sauerstoffschicht sein könnte.

Contents

Preface

Thought surface science is a relatively young branch of science, it has known in the last decades a surprising expansion which still endures. Historically it rose up from Davisson' and Germer's experiment in 1927, but not before the sixties, with the construction of LEED optics and ESCA spectroscopy, and the development of ultrahigh vacuum technology, the scientific productions starts. During the first years, the scientific demand of surface physics and surface chemistry was to study from a fundamental point of view the principles which govern the heterogeneous catalysis. From this ongoing seminal work, the versatility and power of surface physics led to embrace soon several other fields: the awareness that one can study and control matter on atomic scale set the tone for invention, construction and improvement of a batch of miniaturized devices which nowadays are named under the word nanotechnology. The impact of this new technological revolution can be easily seen at the diffusion of this technology around us and at its application even in our daily life. In this revolution, surface physics plays a crucial role, because any improvement needs first the understanding of the single processes.

Manifold techniques to investigate surfaces and interfaces have been developed in the last decades, each of which is specially designed for certain conditions and systems. No singular tool exists that can characterize a system under every aspect. Therefore, a coherent and substantial picture is obtained by the combination of different tools, by knowing their strong points and their limitations. In experimental surface physics, probing tools may be divided in three groups. *Microscopy* images complex surfaces by e.g. illuminating with X-rays, electrons or ions, or by scanning with a probe. *Spectroscopy* studies the emission of electromagnetic radiation or particles from a surface, in function of their energy and mass. In the *diffraction*, the deviation of waves scattered by the surface is used to obtain complementary information about structure and morphology. With these three methods, almost every kind of known material has been investigated:

from single crystals to powders and glasses, from insulators to semiconductors and metals, from long-range structures to thin films, nano-particles and single atoms, up to very complicated systems like high temperature superconductors, fluids and catalysts.

The surface physics uses the *bottom up* approach: starting from a very simple system, the complexity is increased stepwise, until the configuration used in real devices is reached. The *leit-motif* is the control of all involved processes, starting with the simplest model system, typically the surface of a single crystal that has to be kept clean under ultra-high vacuum conditions. This model system can be well characterized; however, problems arise with increasing complexity. For a real device, many parameters play a role, e.g. temperature, pressure, size, purity, space orientation, chemical composition, thickness, heterogeneity, roughness. The influence and the correlation of so many factors are so hard to understand, that *bridging the gap* between models and real systems is still *the* challenge of surface physics for the future. The solution can only be to optimize the existing tools and to simultaneously develop new techniques.

In this frame, the presented work is a little but significant example for various subjects and problems one has to cope with, in the field of surface physics. It includes several aspects: first of all the presentation of the experimental apparatus. SMART is a spectromicroscope which combines techniques from all the three groups described above, and which boosts the capabilities of this instrument class with the introduction of important technical improvements. A detailed description will be given in Chapter **1**. The experimental part starts with the characterization of a complicated surface, produced by a thin film of Fe_3O_4 deposited on a Pt(111) surface. In this chapter, one can see the bottom-up approach, analyzing the construction step by step (Chapter **2**). This knowledge is used to improve the thin film preparation (Chapter **3**). The final chapter (**4**) is dedicated to the deposition of Pt nanoparticles on this film, to study the particular phenomena which render this system a good catalyst.

Chapter 1

SMART

SMART is an acronym for Spectro-Microscope with Aberration-correction for many Relevant Techniques. The project to build up the first aberration-corrected Low Energy Electron Microscope / Photo-Emitted Electron Microscope (LEEM/PEEM) started in the mid-nineties[1], as a collaboration of Universität Würzburg, Technische Hochschule Darmstadt, Fritz-Haber-Institut der Max Planck Gesellschaft and Technische Universitt Clausthal, and with LEO Elektronenmikroskopie GmbH (later Carl Zeiss NTS GmbH, Oberkochen) as the industrial partner. The aim was electron spectroscopy of individual nanometer sized surface objects. Therefore, the limitations of hitherto existing spectro-microscopes had to be overcome to improve the lateral resolution, the transmission and the energy resolution. This could be only done by the development of three new sections projected and built specifically: a fully non-dispersive beam separator made by magnetic dipoles[2], an electrostatic tetrode mirror acting as an aberration corrector and an imaging energy analyzer called Omega-filter[3]. The final assembly was realized at the Fritz-Haber-Institut. SMART is operating at BESSY-II, the synchrotron radiation facility of Helmholtz-Zentrum-Berlin, and connected to a dedicated high flux density beamline. In the following, technical aspects of the spectro-microscope are discussed which are important for this thesis, with particular emphasis on the instrumental configuration, the newly developed procedures for improved performance and the experimental methods to optimize the aberration correction and therefore the lateral and energy resolution.

1.1 Technical introduction

The spectro-microscope SMART uses electrons as a probe. The electrons emitted or reflected at the sample surface are accelerated by an electric field and focused by electrostatic and magnetic lenses. The focal length of such lenses can be controlled by changing the potential of electrostatic lenses, or the current of magnetic lenses. In this way, one can switch easily between several different operation modes. The SMART instrument can be divided into seven main modules: (1) the main chamber, with sample manipulator and objective lens, but also evaporators, gas dosing system and light sources, (2) the magnetic beam splitter, connected with (3) the aberration correcting electron mirror, (4) the transfer optics with variable image magnification, (5) the omega-type energy filter and (6) the projection optics with the 2-dimensional electron detection system. On the bottom of the beam splitter, an electron gun (7) with its illumination optics is connected, which is used for reflected electrons measurements. Two kinds of electrons can be used for imaging: either electrons reflected at the specimen surface via backscattering, using the electron gun, or photo-emitted electrons, excited either by an UV laboratory source (Hg short arc lamp) or by a soft X-rays of the UE49-PGM beamline, specially designed for this experimental station. A scheme of the entire setup is shown in **Fig. 1.1**. Additionally, a preparation chamber with sputtering station and fast entry lock is connected to the main chamber. The entire microscope rests on active dampers at the four corners to avoid vibrations. The main chamber is connected to the beamline illumination the sample under grazing incidence of 20°.

The samples are typically disks with 10 mm diameter and about 2 mm thickness. They are mounted on a transferable sample holder made by ELMITEC GmbH, which provides also a W5%Re/W26%Re thermocouple spot-welded on the sample support and a W filament for backside heating. Once transferred into the main chamber, the sample is approached towards the objective lens until the distance is 2.3 mm. In the operating conditions, the sample potential is kept at about -15 kV referred to the ground of the microscope: in this way the emitted electrons are accelerated into the microscope and travel through the lenses with high velocity. The sample potential can be reduced with high accuracy by a second voltage device (called $< ug >$) floating on the -15 kV bias

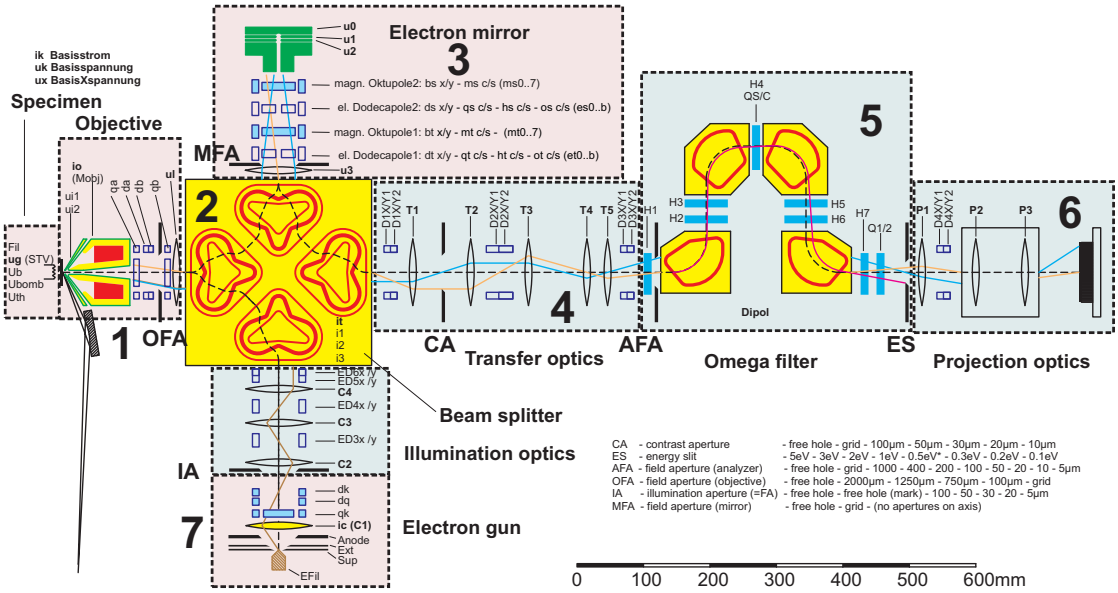

Figure 1.1: Scheme of SMART setup.

potential $< uk >$; since the lenses are designed and excited for electrons with exactly 15 keV of kinetic energy, only the electrons with a starting kinetic energy equal to the additional potential (with opposite sign) pass through the energy filter. With this layout, a scan of the kinetic energy at the sample surface is done simply by changing the sample potential $< ug >$ and the objective lens, while the rest can stay constant. The manipulator has full control of x, y and z direction, as well as the two tilt angles. The z direction is the surface normal, pointing towards the microscope.

The main UHV chamber with a base pressure of 1x10^{-10} mbar is pumped by an ion pump and a titanium sublimation pump. Apart from two big ports along the principal axis for manipulator and objective lens, there are other 17 ports pointing radially to the principal axis. Nine are perpendicular and pointing towards the loading position and eight are pointing towards the observing position with an angle of 20° respect to the sample normal. In the first are accommodated the linear drives for the preparation chamber, the gas line for filling the chamber with pure gases and the pumps in the bottom, while the last are used for devices that need to be pointed towards the sample during the observation, like the evaporators, the beamline and the UV lamp. The magnetic objective lens sets the image plane at the entrance of the beam splitter. Between objective

lens and beam splitter two dipoles and quadrupoles are used for the alignment. In front of the beam splitter a set of field apertures can be inserted for moulding the image and removing the outer electrons which are not detected at high magnification.

The beam splitter, specially designed for this instrument[2], consists of two quadratic plane pole plates separated from each other by a distance of 7 mm. Four coil triplets are placed on the inner surface of each pole plate; the triplets are placed with fourfold symmetry. The current through the coils generates a magnetic field with a particular spatial arrangement, which provides a 90° deflection of the electron beam with a perfect imaging equivalency (”one to one” imaging of the entrance plane at the splitter edge to the exit plane and ”parallel in to parallel out” imaging); due to the highly symmetrical path, no aberrations up to the second order (and several to the third) are introduced.

The electrostatic mirror is the device responsible for the spherical and chromatical aberration correction. It is made by four different electrodes (tetrode), placed at different potentials and with cylindrical form. The last mirror electrode, $< u0 >$, is set at a potential of about -2 kV with respect to the bias voltage $< uk >$; in this way the electrons are slowed down, reflected in the field in front of $< u0 >$ and reaccelerated back to 15 kV with opposite direction. The optical mirror plane is physically the equipotential plane at 15 kV in front of the last electrode. The three potential settings of the tetrode (the forth electrode is at ground) determine the shape of the reflection plane, and consequently the compensation for the aberrations. An electrostatic einzel lens ($< u3 >$) between beam splitter and tetrode images the diffraction plane (backfocal plane of the objective lens) just on the reflection plane of the mirror. Between this lens and the mirror two dipoles and quadrupoles are used for the alignment and correction of stigmatism and distortion. A more detailed discussion about the aberration principles and the mirror setup can be found in Section 1.3.

The electrons traveling back from the mirror pass again through the beam splitter and are deflected into the transfer optics. Here five einzel lenses provide a variable final magnification factor. The electron beam is aligned through the lenses by two pairs of dipoles. A set of contrast apertures is located in the fixed backfocal plane of the first lens and limit the acceptance angle of the electron beam. The transfer optics places the magnified image or diffraction plane to the entrance of the energy filter, where another

set of field apertures can be inserted.

The energy filter is made by four magnetic 90° deflectors which are arranged to each other in a way that the resulting optic axis has the shape of the Greek capital letter Omega[3]. Electrons with different kinetic energies pass through the omega-filter on different trajectories. At the exit, a slit in the dispersion plane of the filter selects the electrons on the central trajectory with an energy width set by the variable slit size. The mirror symmetry plane perpendicular to the optic axis of the microscope and the different multipoles (quadrupoles and hexapoles) between the modules correct the first and second order aberrations and possible distortions induced by the filtering, resulting in an energy resolution of better than 100 meV and a lateral resolution of more than 1000 pixel of resolution.

Finally, the aberration-corrected and energy-filtered electron beam is projected by three einzel lenses to the detector, which consists of a pair of microchannel plates of 40 mm of diameter with a gain factor of 10^6, and a phosphorus screen that converts the electric signal into light. The image produced on the screen is captured by a Peltier cooled CCD camera with a resolution of 2 megapixel (1600x1200) and a dynamic range of 14 bit.

In the bottom entrance of the beam splitter, a Schottky field emitter electron gun provides a continuous beam of electrons under conditions of high brilliance and stability of kinetic energy (15 keV). The illumination optics creates a parallel beam at the entrance plane of the beam splitter with control over the diameter and the incident angle on the sample surface. The illuminated area on the sample has typically a diameter of about 25 μm.

The beamline, installed at the UE49 undulator source, provides soft X-rays in an energy range between 80 and 2000 eV and with selectable linear and circular (elliptical) polarization. The photon beam passes through a high flux plane gratings monochromator (resolving power of $E/\Delta E$ = 8000 at hν = 200 eV) and is focused on the sample by an elliptical mirror, which demagnifies the beam source by a factor of 20. The final beam has a maximum flux of 1x10^{12} ph/(s*100mA*ΔE), concentrated in a surface spot with a size of 11x7 μm^2.

The entire microscope optics is controlled by two PCs: on the first the so-called DAS software controls the general voltage, the objective lens, the beam splitter, the electro-

static mirror and all multipoles in these modules; on the second the so-called Omega software controls the lenses and deflectors of transfer optics, omega-filter, projector and electron gun optics. Special devices like the microchannel plate voltage, the CCD camera and the active dampers are controlled separately with manual or computer controlled supplies. The beamline control software operates on a third PC provided by BESSY-II user service. DAS and Omega software have been written specifically for SMART and allow full control over every parameter which can be stored and reloaded in setting files. During this PhD work some special aligning and testing routines have been developed. A substantial part of the experimental time has been dedicated to the improvement of these optimization routines and to resolution tests.

1.2 Aligning Techniques

The microscope is built up by a series of electrostatic and magnetic lenses and multipoles, which were produced and mechanically adjusted to each other with high accuracy. However, an even finer alignment can be obtained by using the electron beam as a probe. Therefore, the different modules of the microscope have been switched on separately and aligned one after the other by the deflectors. After this first setup, the further alignment requires only the fine tuning of the lens excitation (potentials and currents) that govern the different elements of the microscope. Here, only the final procedures will be discussed, with particular emphasis on those developed during my doctorate.

The alignment techniques can be divided into two categories: *frequent alignment* at the beginning of every experimental session; and *general alignment* for parameters which do not require a continuous check and can be kept for a longer period.

1.2.1 Frequent alignment

After a new sample is introduced in the microscope, first of all, the tilt angle i.e. the angle between the surface normal and the optical axis has to be reduced by a margin lower than 0.1°. The tilt angle of the sample can be set with two screws on the rear of the manipulator. Assuming that most of the electrons are emitted isotropically and

mainly normal to the sample surface, one can set the tilt by observing the shift of the image induced by a change of the objective lens excitation and therefore of the position of the focal plane along the axis: only if the sample surface is perfectly perpendicular to the microscope axis the image objects do not move by changing the lens focus. Unfortunately, this criterion is valid only for photo-emitted electrons, i.e. in PEEM. In LEEM mode, electrons are elastically reflected at the sample surface. In spite of a wrong mechanical tilt angle the out-coming beam can be on the optical axis just when the incoming angle compensates perfectly the effect of the wrong tilt angle (see **Fig. 1.2**). As a consequence, one needs two independent criteria to optimize the mechanical sample tilt and the perpendicular illumination. For the mechanical tilt alignment in LEEM the excitation of the objective lens is reduced so much, that the back focal plane is shifted into the intermediate image plane at the beam splitter entrance, i.e. the electron beam is concentrated in one point which has to be brought to the position of central surface point (rotation center of objective lens) by the mechanical tilt adjustment screws. On the other hand, when increasing the objective lens excitation, the incident beam is concentrated at the center of the image, i.e. the back focal plane is imaged onto the specimen surface. This crossover point has to be brought to the central surface point by the illumination deflectors and therefore by optimizing the illumination angle. By iterations of the over and under focus procedures one can reach the optimum setting for mechanical tilt and illumination angles. The optimum is reached when both changes in focus concentrate the beam in the same point.

Next step is the identification of the physical axis of the microscope and its intercept on the sample surface. This is done using the fact that the objective lens is a magnetic lens, which turns the image along the axis by about 60° because of the Lorentz force. If the objective lens current is inverted in sign, the image rotates by about 120°. The rotation point on the image is the intersection between the axis of the objective lens and the sample surface. This turning point will be the reference for the following alignments: the other lenses of the microscope should be centered on this point as well. Before this, it is necessary to refine the tilt alignment, by making sure that the electron beam concentrates in the turning point when the image is far out of focus.

The alignment of the electrostatic lenses is performed by modification of the electron beam trajectory. The electron beam is deflected by dipoles and quadrupoles; in the mi-

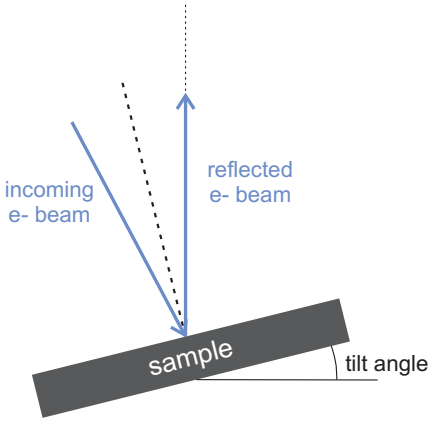

Figure 1.2: Scheme of tilt alignment in LEEM. A wrong incoming angle and a non-zero mechanical tilt angle can produce a beam reflected correctly on axis.

croscope the deflectors are always organized in pairs and they are combined together in order to affect the trajectory of the beam through a pair of lenses. With this combination two deflectors for two lenses it is possible to adjust the optical path through one lens without changing it for the other[4].

For the frequent alignment it is necessary to check only the transfer optics system (see **Fig. 1.3**). It consists of two sets, each one with two lenses (marked as T) and two dipoles (marked as D), and a fourth set with one lens, the omega-filter and two dipoles. In the second an extra lens, T4, is activated only when the omega-filter is switched on. The alignment procedure follows the electron path, so the first lens to be aligned is T1, then T2 and so on. The reference point on the surface is still that one identified before, where the microscope axis intercepts the surface. When the transfer optics is aligned, the microscope is ready to use.

1.2.2 General alignment

In the general alignment the remaining devices are adjusted, i.e. the objective lens, the beam splitter, the electrostatic mirror and the omega-filter. This is stable in time and requires no further check if the frequent alignment was set correctly. As described before, the procedure follows again the electron path. The alignment of the omega-filter has been already addressed and fully described, theoretically as well as experimentally[3].

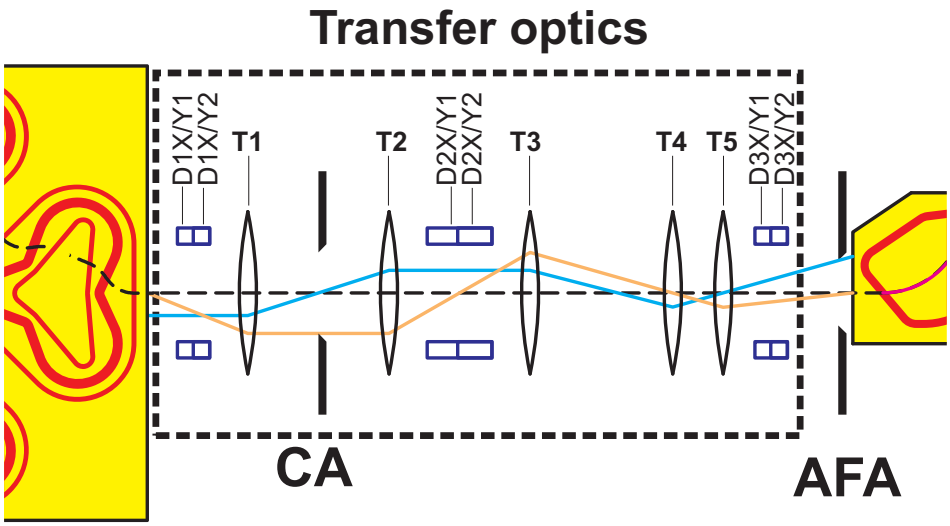

Figure 1.3: Scheme of the transfer optics. CA is the contrast aperture put on the back-focal plane of the lens T1.

The general procedure has to be performed only in PEEM mode: in LEEM mode the electrons pass twice through the objective lens and a misalignment in the electron gun optics can propagate through the following lens systems. In addition, the omega-filter should be switched off, in order to avoid possible distortions coming from its misalignment.

Setting the correct value for $< ul >$ and $< u3 >$

As shown in **Fig. 1.1**, two lenses, labeled as $< ul >$ and $< u3 >$, are put in front of the entrances of the beam splitter. The first one has to produce a parallel beam at the beam splitter entrance, while the second has to transfer the backfocal plane on the electrostatic mirror plane. Electrons pass through $< u3 >$ twice, before and after reflection in the mirror. In **Fig. 1.4** the optical layout is simplified: here the mirror is described as a concave lens and the beam splitter as a box with 1:1 correspondence between entrance and exit. Since $< ul >$ and $< u3 >$ are subsequent, a correct position of the final image plane can be obtained even if both are diametrically misaligned. The fact that, due to the mirror presence, the electrons pass twice through $< u3 >$ permits to decouple the effect of the lenses if one introduces two different criteria for the selection of $< ul >$

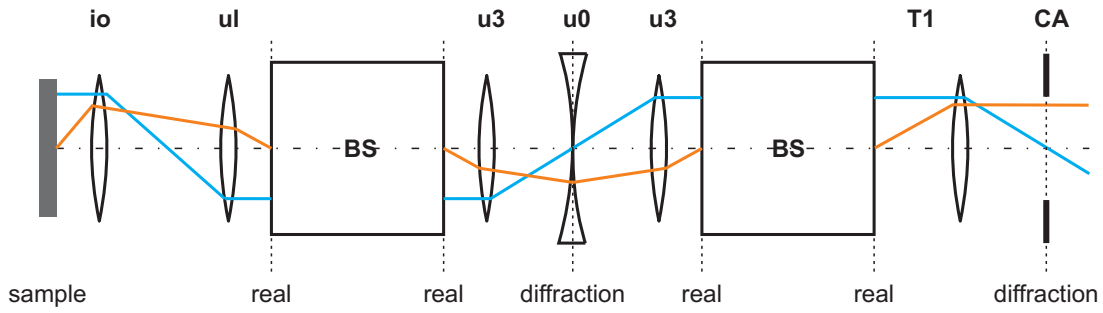

Figure 1.4: Scheme of the SMART lens system with the electrostatic mirror $< u0 >$ represented as a concave lens. The orange trajectory ray starts at the center of the sample with an angle, whereas the blue trajectory starts off-center and parallel to the axis.

and $< u3 >$. The chosen criteria are the position of the diffraction plane in $< u0 >$ and the contrast aperture plane in the transfer optics. For the first, if the diffraction plane is not in $< u0 >$ the image is distorted, so one can choose a value for $< ul >$, oscillate periodically (i.e. wobble) the potential of $< u0 >$ and evaluate the value of $< u3 >$ that gives the minimum movement of the image. For the second, a circular contrast aperture of 30 μm is put in the transfer optics. By changing $< ul >$, the diffraction plane is moved away and the aperture becomes visible in the image plane; the corresponding value of $< u3 >$ is set when the aperture is not visible anymore. The two sets of couples are displayed in **Fig. 1.5**; every set has been fitted with a line. The correct value for $< ul >$ and $< u3 >$ that satisfied both criteria is the intercept of the line fits. It is interesting to notice that the slopes of the fit are related by a factor ~ 2. This is related to the fact that the electrons are traveling only once through $< u3 >$ before they reach the test position for the first criterion ($< u0 >$) and twice before that for the second criterion (contrast aperture); therefore in the last case the correction amplitude on $< u3 >$ should be half. Once the correct values of $< ul >$ and $< u3 >$ have been set, it is possible to align the beam splitter.

Setting the correct value of $< it >$ and $< qb >$

The magnetic field inside the beam splitter can be set with only one parameter, $< it >$, the current through the coils. The wished situation is when no image shift and beam tilt

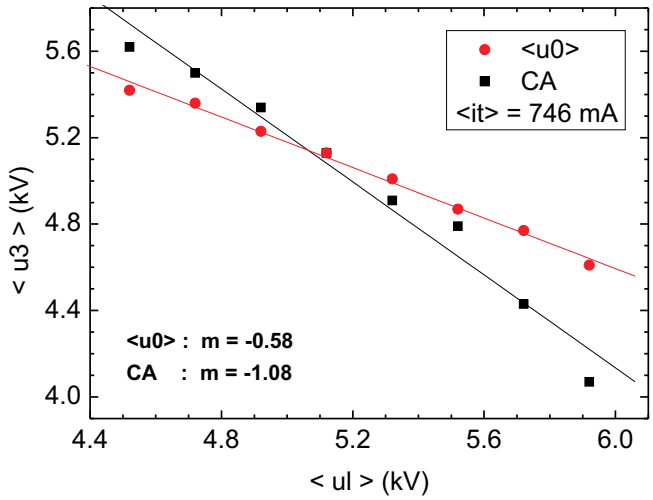

Figure 1.5: Values of $< ul >$ and $< u3 >$ that guarantee a correct position of the diffraction plane in $< u0 >$ (in red) and at the contrast aperture (in black). The optimum values are at the crossing of the linear fits. The slopes m for both linear fits are depicted.

is produced when $< it >$ is changed. Assuming that the sample tilt and $< ul >$ are set correctly, it is achieved when the electron beam comes out from the splitter perpendicularly. This condition can be checked by looking at the image for different $< it >$ values: if this is not correct, the image comes out from the beam splitter distorted along one axis, and/or moved. This distortion can in principle be compensated with electrostatic quadrupoles at the entrance or at the exit of the splitter, but the best would be that no further compensation is required. The presence of the mirror helps to establish the alignment criterion: one can use the compensative distortion induced by the quadrupole $< qt >$ inside the mirror to evaluate the influence of $< it >$. The trick is to have two benchmarks, one inside the mirror (beam splitter crossed only once) and one in the transfer optics (beam splitter crossed twice). The first is wobbling the mirror surface $< u0 >$ and minimize the distortion; the second is to insert a contrast aperture which is perfectly round by construction and correct its shape in the image until is a perfect circle. In this way one obtains two sets of values $< qt >$ versus $< it >$, with the optimum at the crossing where both criteria are satisfied. For the first criterion, a correction

in the value of $< u3 >$ is also required: a changed deflection of the beam splitter moves the position of the diffraction plane inside the mirror. In **Fig. 1.6a** the relation between $< it >$ and the cosine and sine values of $< qt >$ for both criteria is shown. Clearly, the $< it >$ values for sine and cosine are not identical. This can only be explained by assuming an intermediate image at the beam splitter entrance already distorted by the objective lens and/or by $< ul >$. For this reason, another quadrupole, $< qb >$, is set between these two lenses. $< qb >$ is linked with $< qt >$ in a way that they compensate each other and the electron trajectory remains untouched inside the mirror. In this way one can act on $< qb >$ to bring the optimum $< it >$ values for sine and cosine to convergence. The effect of $< qb >$ is visible in **Fig. 1.6b** and **c**: a change in $< qb >$ affects only the optimum value of $< qt >$ set with the evaluation of the contrast aperture (empty dots), whereas it is constant with the criterion of the wobbling of $< u0 >$. With this setting, the effect of $< qb >$ is to introduce an offset in the values of $< qt >$ that satisfy the first criterion, while it has almost no effect for the values identified with the second. At correct $< qb >$ value for the crossovers in the plot of the cosine and sine values of $< qt >$ versus $< it >$ occur at the same value of $< it >$. In this way, also the correct value for the beam splitter current is found: 746.5 mA with a $< qb >$ value of (0.0; -2.8) for cosine and sine, respectively.

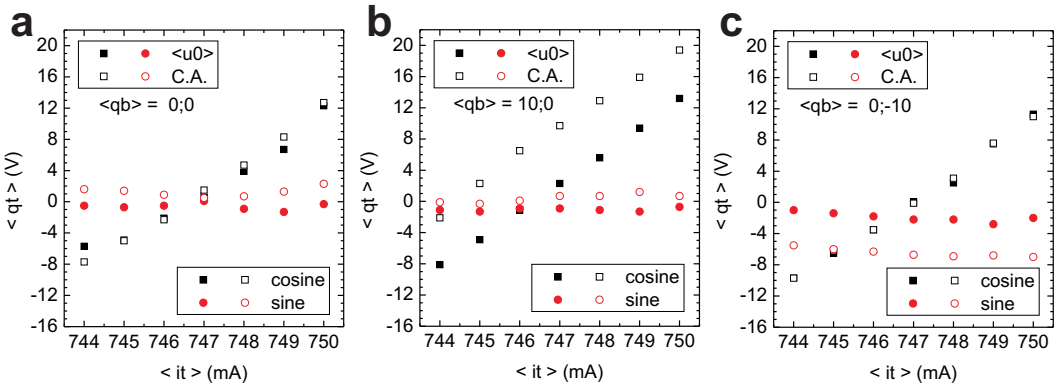

Figure 1.6: Values of sine and cosine of $< qt >$ for several $< it >$ and $< qb >$ values. The full dots are obtained when the wobbling of $< u0 >$ is concentric, the empty dots when the contrast aperture after the lens T1 has a perfectly rounded shape. A change in $< qb >$ has effect only on the empty dots.

Set the correct value of $< u0 >$

In principle, the mirror voltage $< u0 >$ regulates its focal length. Therefore, for every value of $< io >$ it is always possible to find a value of $< u0 >$ that compensates a misplacement of the image plane between objective lens and mirror and gives a final sharp image. Among all these pairs, only the one that displace the image plane at the beam splitter entrance is correct, for the reasons explained in the previous paragraph. In an ideal case, one would insert a diagnostic grid inside the desired plane and try to find the pair of values where both, the grid and the surface image, appear sharp. That means, change $< u0 >$ until the grid is sharp (i.e. mirror focuses onto the grid) and then change $< io >$ until the surface image is sharp as well. Unfortunately, due to technical reasons it is not possible to insert a grid in the desired plane. Instead, two grids are used, which are both 49 mm away from the beam splitter entrance, one in front and one behind the beam splitter. The grids are used to estimate the estimate the exact position of the image plane with the following procedure. First of all, set the objective lens current $< io >$ to get a sharp sample image. In a second, the first grid in front of $< ul >$ is inserted and $< u0 >$ changed until the image of the grid is sharp; in this way the source plane of the mirror is shifted until it reaches the grid position. Now $< io >$ is changed until the sample image is sharp again; that means, the image plane is located in the position of the first grid (**Fig. 1.7a**). This procedure can be applied analogously to the second grid as well: due to the 1:1 correspondence of the beam splitter between entrance and exit, inserting a grid outside the exit is equivalent to put a grid inside the entrance (**Fig. 1.7b**). The two $< io >$ values found with this procedure correspond to the image plane put 49 mm in front and behind the beam splitter entrance; setting the objective lens $< io >$ to the average value brings the surface image plane in to the beam splitter entrance. With this, it is sufficient to modify $< u0 >$ until the image is sharp and the condition where both planes are in the right position is achieved.

Once the general alignment is done, the frequent alignment is sufficient to achieve the best performance of the microscope: with the correct mirror settings a resolution below 5 nm can be easily and routinely obtained in LEEM.

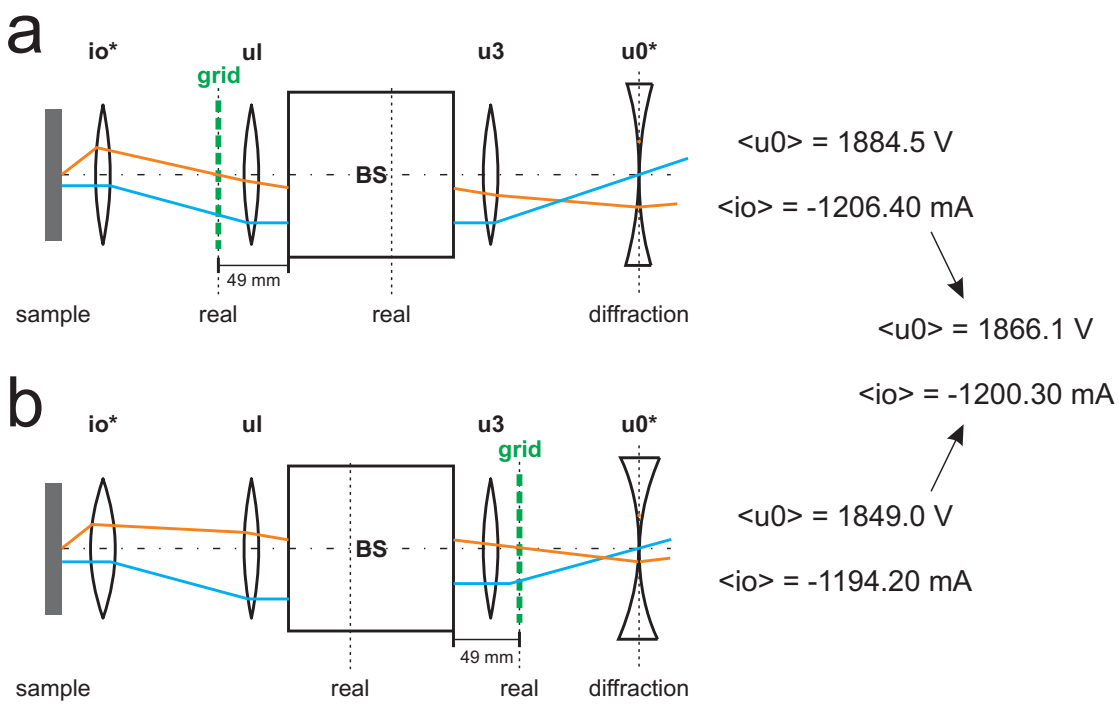

Figure 1.7: Configuration of the microscope in case (a) the grid before the beam splitter and the sample image are sharp and in case (b) the grid after the beam splitter and the sample image are sharp.

1.3 Measurement of the aberration compensation

The aberrations are the deviations from the theoretical position of the image point; these deviations may depend on the incoming angle (spherical aberration) or the energy (in light optics: color, therefore called chromatic aberration) of the incoming rays. Known since the nineteenth century, the theory of spherical and chromatic aberration in optics is applied to build correction systems. In light optics, most of the correction systems are made by combining convex and concave lenses, since the two types of lenses produces aberrations of opposite sign. That means, one can construct an optical system in which the aberrations produced by the convex lenses compensate those caused by the concave ones. In electron optics, the aberration compensation cannot be done in this easy way, because concave electron lenses do not exit (Scherzer's theorem[5]); but only convex lenses with fixed sign for the aberrations, so a new compensation method is required.

Among the alternative methods known, the introduction of a mirror is the right choice for several aspects, not at least the relatively low technical demanding and the absence of limitations introduced in the normal use. The principle, how a mirror can compensate spherical and chromatic aberrations, is shown in **Fig. 1.8**.

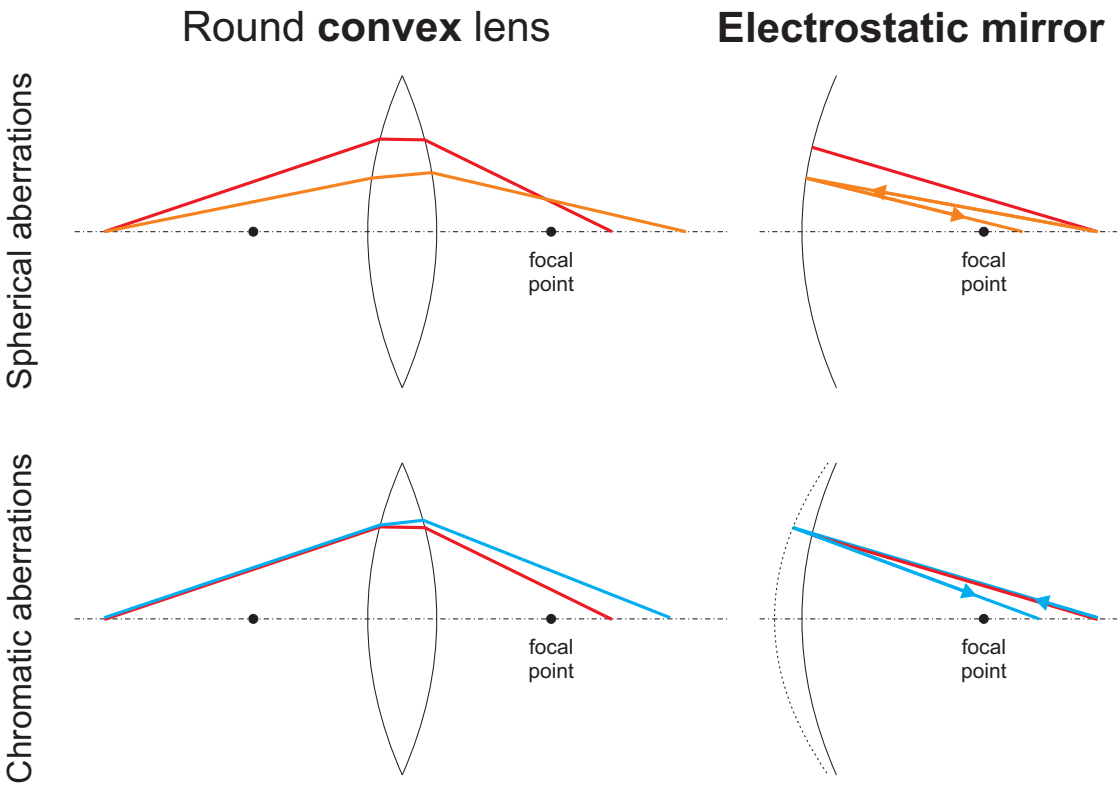

Figure 1.8: Scheme of the effect of spherical and chromatic aberration on a round convex lens and on an electrostatic mirror.

The electrostatic mirror operating in SMART is schematized in **Fig. 1.9**. The mirror plane for an electron is the equipotential plane where the electron is reflected. The shape of the equipotential plane can be controlled by the potentials $< u0 >$, $< u1 >$ and $< u2 >$, in a way to reproduce different spherical and chromatic aberrations. Because the electrons are accelerated in the objective lens, the aberrations depend on the initial kinetic energy of the electrons at the sample surface. Therefore, the mirror settings have to be tuned as a function of $< ug >$ to reach the optimal compensation. The range of the aberration coefficients that can be compensated in the mirror is wide, between 0

and 70 m for the chromatic and between 0 and 50 km for the spherical; in this case one can reach the optimum compensation for electrons with an initial kinetic energy ranging from 0 to several hundreds of eV.

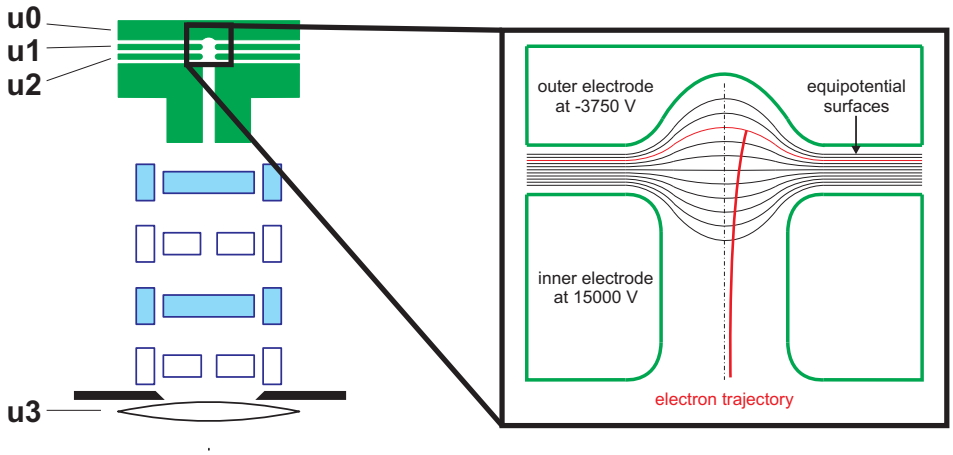

Figure 1.9: Simplified scheme of the internal structure of the electrostatic mirror. The shape of the equipotential surfaces can be changed by the potentials of the electrodes.

1.3.1 Resolution limit

In the ideal case of an aberration-free system the image of a point-like source is again a point. Aberrations blur this image and the point becomes a so-called disk of confusion. The radius of this is a measure for the aberration effect on the lateral resolution and their dependence on different parameters like acceptance angle and energy spread of the electron beam. Since the coma and the distortion of the field effects can be neglected in a system like SMART, the resolution d_0 is given by the width of the disks of confusion caused by chromatic and spherical aberration and the diffraction limit and therefore depends only on the acceptance angle, the energy width ΔE and the start energy E_0[6]. The resolution can be expressed as a Gaussian convolution up to the fifth order as:

$$d_o = \sqrt{d_d^2 + \left(\frac{d_s}{2}\right)^2 + d_c^2 + d_{ss}^2 + d_{cc}^2 + d_{sc}^2} \tag{1.1}$$

with

$$
\begin{aligned}
d_d &= \frac{0.61\sqrt{\frac{1.5}{E_0}}}{\sin\alpha} \\
d_s &= C_s \sin^3\alpha \\
d_c &= C_c \frac{\Delta E}{E_0} \\
d_{ss} &= C_{ss} \sin^5\alpha \\
d_{cc} &= C_{cc} \left(\frac{\Delta E}{E_0}\right)^2 \sin\alpha \\
d_{sc} &= C_{sc} \frac{\Delta E}{E_0} \sin^3\alpha
\end{aligned} \tag{1.2}
$$

Here d_d is the diffraction term, due to the cutoff of high frequency Fourier components in the image by an aperture in the diffraction plane that limits the acceptance angle α. The other components are the effect of the spherical and chromatic aberrations. Due to the small value of the diffraction limit d_d in standard experimental conditions (less than 1 nm), the resolution is mainly determined by the spherical and chromatic aberrations; the effect of the first one is typically dominant for higher kinetic energy, while the second is more significant at lower kinetic energy, or when the energy filter is not active.

The tetrode mirror can compensate the aberration effect by reducing the lower order coefficients C_s and C_c to zero. In this case, only higher rank aberrations remain, and the resolution limit can be significantly improved (**Fig 1.10**). In parallel, the compensation of the aberrations up to the third order allows to increase the acceptance angle without loss of resolution; in fact, for improving the resolution the acceptance angle has to be increased to avoid diffraction limitations. This increases the transmission (T $\sim \alpha^2$) up to two orders of magnitude compared to uncorrected systems.

1.3.2 Measurement of the spherical aberration

The spherical aberration can be effectively measured in SMART by exploiting the fact that in LEEM the electrons are elastically reflected only with certain out-coming angles (which generate the LEED spots). Due to the very narrow angular distribution of a sin-

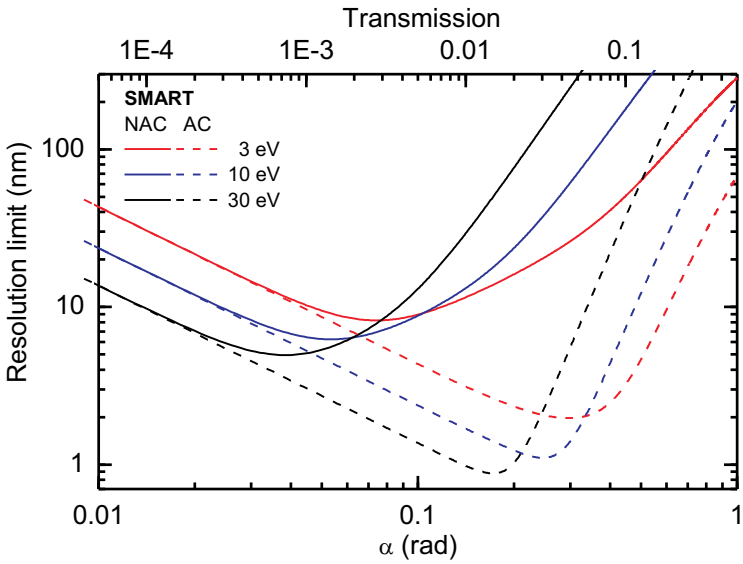

Figure 1.10: Resolution limit calculations for non-aberration-corrected (NAC) and aberration-corrected (AC) regimes and for different electron kinetic energies. In AC regime, the minimum resolution is reached at larger acceptance angles than in NAC, determining simultaneous increase in transmission.

gle diffraction spot, the specularly reflected beam is used to scan precisely the angular dependence of the object position in the image, and based on this the C_s coefficient of the overall system is calculated. Therefore, the inclination of the incoming electron beam is changed with respect to the surface normal by using the last dipole in the illumination optics of the electron gun; the outgoing beam is reflected with the same angle, and will form a final image of the surface which is shifted in the xy plane. The relation between shift and deflection angle contains the information over the C_s value.

For a quantitative evaluation of the spherical aberration coefficient the deflection angle has to be calibrated. The real input is the deflection voltage applied to the last electrostatic dipole in the illumination optics. Consequently, this value has to be correlated to the deflection angle. One method to find the correlation is to measure in LEED mode the shift of the (0;0) diffraction spot induced by the deflection. The change in the re-

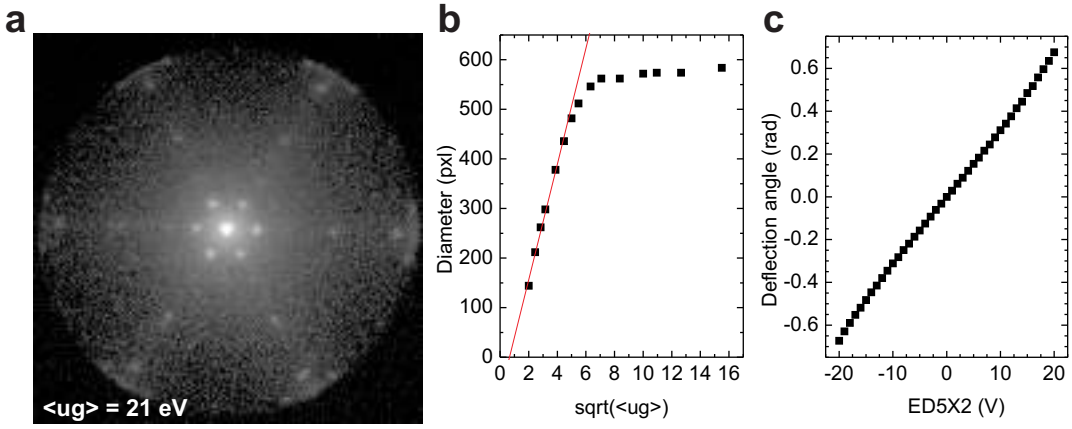

Figure 1.11: (a) Example of a LEED pattern of a mixed phase (FeO+Fe_3O_4)/Pt(111); the Ewald sphere is visible as the circle with higher background. (b) Relation between the diameter of the Ewald sphere and the square root of $< ug >$. The trend is linear until it reaches a saturation value imposed by an aperture in the lens system. The non-zero intercept of the linear fit on the x axes indicates an offset between $< ug >$ and the initial kinetic energy of the electrons E_0, quantifiable in 0.8 eV. (c) Deflection angle of the incoming electrons in function of the potential of the deflecting dipole ED5.

flection angle corresponds to this shift in position r_{pixel} (distance from center of the LEED pattern measured in pixel on the detector) which can be calibrated by the radius of the Ewald sphere r_{pixel}^{max} (clearly visible on the detector as a circular area with higher background, **Fig 1.11a**), which corresponds to the 90° deflection at the sample surface. Since the radius of the Ewald sphere changes with the square root of the initial kinetic energy at the surface E_0 (**Fig. 1.11b**), the deflection induced by the dipole needs to be related to this energy dependence. One finds the relation between the voltage of the dipoles and the deflection angle by measuring the ratio between the shift of the LEED spots and the radius of the Ewald sphere (**Fig. 1.11c**).

$$\frac{r_{pixel}}{r_{pixel}^{max}} = \frac{\tan \alpha_1}{\tan \alpha_1^{max}} \tag{1.3}$$

This angular deflection, however, occurs at the sample surface; the corresponding angle α_1 in the intermediate image plane can be calculated as follows. Once reflected,

the electron beam is accelerated by the electric field between sample surface and microscope ground (i.e. potential of the first electrode), gaining in kinetic energy from initially E_0 at sample surface to finally E_k, the base energy of 15 keV in our case. Here, the image is magnified by the objective lens with M = 18. As a consequence, the corresponding angle α_1 at the first intermediate image plane is related to the deflection α_0 on the sample surface by:

$$\sin\alpha_1 = \frac{1}{M}\sqrt{\frac{E_0}{E_k}}\sin\alpha_0 \tag{1.4}$$

The deflector ED5 in the gun is effectively placed in a virtual image plane, therefore the deflector voltage U_{defl} changes the incoming angle α_1 by:

$$\sin\alpha_1 = C_{defl}\,U_{defl} \tag{1.5}$$

Because the angle α_1 is very small, we use the approximation $\sin\alpha_1 \simeq \tan\alpha_1 \simeq \alpha_1$ in the following. Combining eqs. 1.3 and 1.4 and taking into account that the maximum α_0 = 90°, one has that:

$$\frac{r_{pixel}}{r_{pixel}^{max}} = \sin\alpha_0 \tag{1.6}$$

With this, the deflection angle in **Fig. 1.11c** was calculated. From the linear dependence in this plot, the relation between the deflection voltage U_{defl} and the deflection angle α_0 can be directly extracted:

$$\sin\alpha_0 = \tilde{C}_{defl}\,U_{defl} \tag{1.7}$$

The constant $\tilde{C}_{defl}$ depends on the chosen kinetic energy E_0 at the sample surface. The dependence can be evaluated by comparing eq. 1.7 with 1.5, using eq 1.4, where the constant is independent on the surface energy:

$$\tilde{C}_{defl} = M\sqrt{\frac{E_k}{E_0}}\,C_{defl} \tag{1.8}$$

Therefore, in the case of $\tilde{C}^*_{defl} = \tilde{C}_{defl}(E^*_0)$ known for a specific energy E^*_0, the value for the energy E_0 is:

$$\tilde{C}_{defl}(E_0) = \tilde{C}_{defl}(E^*_0)\sqrt{\frac{E^*_0}{E_0}} \tag{1.9}$$

With this relation, we could use eq. 1.7 to estimate the deflection angle α_0 at a given deflection voltage U_{defl} at every energy E_0.

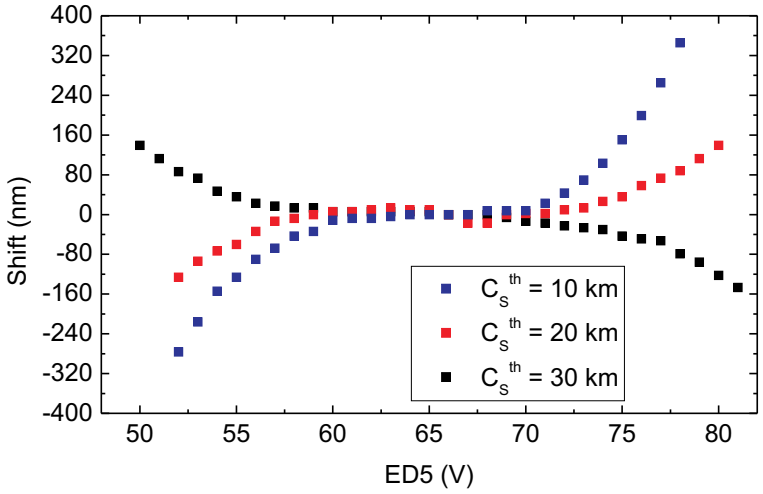

Figure 1.12: Image displacement as a function of the deflection voltage induced by the dipole ED5 (corresponding to a tilt of the illumination angle) for three different aberration compensations (C_s variable, C_c = 30 m). For the settings, the theoretical mirror voltages were used.

For the measurement of the image object shift induced by aberration combined with off-normal tilting of the electron beam, the surface potential $< ug >$ and therefore the kinetic energy has been chosen for optimal image contrast to visualize surface details. Additionally, the field of view has to fit to the maximum displacement possible. The im-

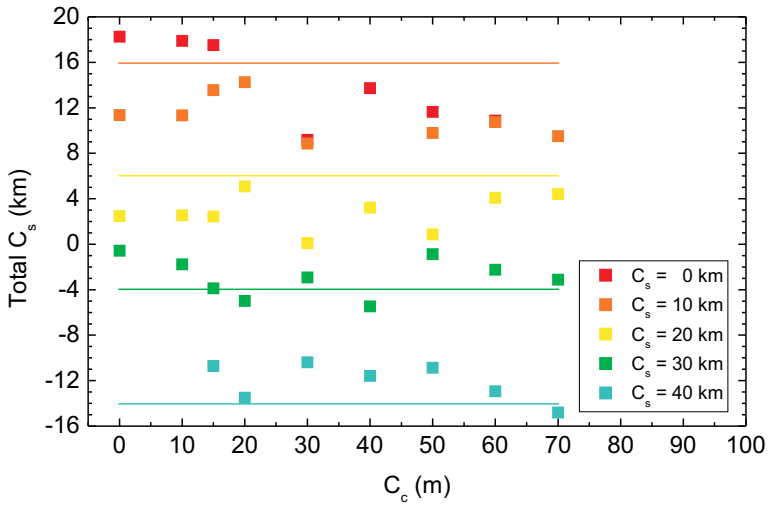

Figure 1.13: Overall C_s values measured for different theoretical C_s^{mirror} (colors) and C_c^{mirror} (x axis) values induced by the electrostatic mirror. E_0 = 19 eV. The optimum condition is when the mirror compensates the aberration of the lens system, i.e. when the total C_s is zero. The theoretical aberrations for the (uncompensated) objective lens at E_0 = 19 eV are C_s^{obj} = 26 km and C_c^{obj} = 20 m. The expected values of the overall C_s values are indicated with horizontal lines.

age object shifts were measured for two deflection directions (x and y direction) and for different mirror settings, in order to cover a wide range of not only C_s but also C_c values. The image displacements were converted in nm length scale, basing on the calibration of the used field of view, and then rescaled by a factor M, accordingly to the fact that the image is magnified by the objective lens. **Fig 1.12** shows the displacement as a function of the deflection angle at the sample surface for three different mirror settings. The data were fitted with a fifth-degree polynomial function, in order to extract the overall C_s and C_{ss} coefficients. In **Fig. 1.13** the extracted C_s values of the entire system (lenses plus mirror) are plotted for different theoretical C_s and C_c values induced by the mirror. The optimum spherical aberration correction is achieved when no displacement occurs over a wide range ED5-deflection (i.e. illumination angle). This is theoretically the case for a mirror setting of C_s = 24 km. It is important to notice that in a certain range the

electrostatic mirror allows a free choice of the total C_s value (quasi) independently of the actual C_c setting (and vice versa).

1.3.3 Measurement of the chromatic aberration

As in the case of spherical aberration, equation 1.1 indicates the strategy for this measurement: C_c can be evaluated from the change in the focus position caused by a change in the kinetic energy of the electrons at the sample surface. A contrast aperture of 10 μm was inserted in the image of the objective back-focal plane behind the T1 lens, to reduce the acceptance angle of the electrons down to a few degrees and avoid the effect of spherical aberrations. Before discussing the data, however, a more detailed insight into the system is required.

The chromatic aberration of a standard spectro-microscope is mainly produced by the magnetic objective lens. To figure out the system configuration, a schematic view of the initial stage is presented in **Fig. 1.14**. From the sample, fixed in position, an electron trajectory starts with an angle α_0 with respect to the surface normal and with fixed kinetic energy E_0. In front of the surface the electron is accelerated into the microscope by the electric field between the sample and the first electrode of the objective lens. The potential difference is 15 kV minus the selected $< ug >$ value. In first order, this accelerating field can be described as a homogeneous field[7–9], therefore the electron trajectories have approximately a parabolic shape. This uniform field introduces chromatic (and also spherical) aberrations, which can be analytically calculated and depend on the initial energy E_0 and on the acceleration field strength[8]. At the entrance of the lens, the electron trajectory appears as emitted by a virtual sample put at twice as large distance and with an equivalent angle α. The effect of the aberrations created by the electrostatic field can be seen as a different position of the virtual image for electrons with different initial kinetic energy (in the figure, the orange and the blue trajectories). The electrons are then deflected by the objective lens, which recreates an image plane at the entrance of the beam splitter. The lens introduces further chromatic aberrations, which determine a shift in the position of the final image plane in function of the final energy E_k.

For the evaluation of chromatic aberrations, one needs to measure the position of the focal length in function of E_0 and E_k values, by changing one while the other is fixed.

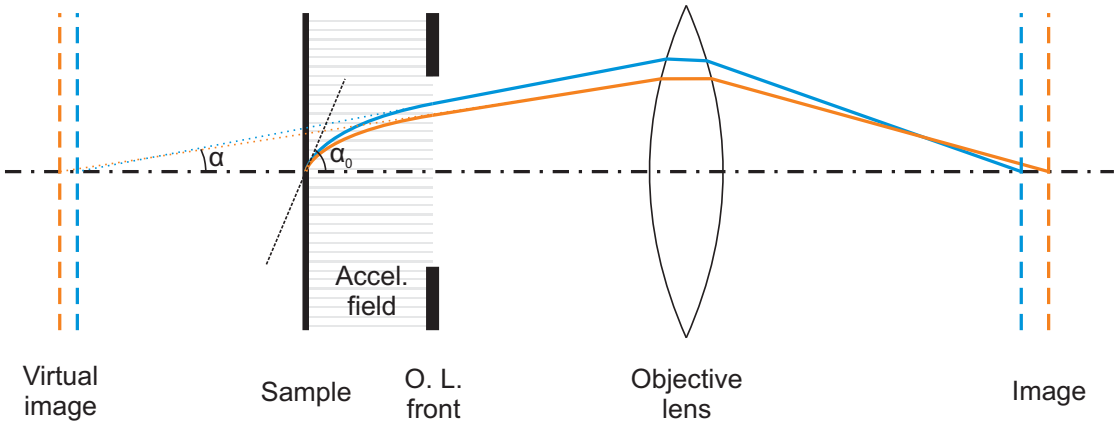

Figure 1.14: Scheme of the initial stage of the microscope. Two electron beams with different initial and final kinetic energy are displayed in different colors, together with the relative shifts in the image plane position determined by the chromatic aberrations.

Two different sources of electrons are required in the following. The first one is the electron gun: in LEEM mode, one can change the initial kinetic energy E_0 without changing the final E_k which equals the kinetic energy of the incoming beam[10]. In this way one can evaluate the aberration induced by the accelerating field between sample and objective lens. The second one should have a fixed and independent E_0; a change in E_k will then produce a shift in the focus position in function of the aberration induced by the objective lens and the electrostatic mirror[11]. An easy way to fulfill this condition is using a source of photo-emitted electrons, i.e. working in Hg-PEEM mode. Since the Omega-filter should be switched off (otherwise the image built with electrons at different E_k is shifted due to the deflection of the Omega-filter), the photo-emitted electron beam should be monochromatized from the beginning. This can be provided by using a Ag(111) sample with a work function of 4.74 eV which is slightly lower than the photon energy (4.85 eV) of the Hg lamp mounted on SMART. This yields in a photo-emitted electron beam with a narrow energy spread of only about 0.1 eV. Finally, the focus position can be extrapolated by the current value of the objective lens $< io >$ that give a sharp image. In fact, for small changes $< io >$ is linearly correlated with the shift of the image plane[11].

In LEEM mode, the behavior of the objective lens current $< io >$ as a function of $< ug >$ (which corresponds to E_0 plus an offset related to the work function of the

system) is depicted in **Fig. 1.15**. The theoretical prediction for this curve is expressed by the following equation[10] being y the position of the image plane,

$$y = y_0 + A\sqrt{E_0} \tag{1.10}$$

where y_0 is the nominal position of the image plane at zero kinetic energy and A is a normalization factor. The fit of the experimental data with this function is shown as the red curve. The derivative of this function, i.e. its slope at a certain $< ug >$, is proportional to the chromatic aberration coefficients induced for that kinetic energy by the accelerating field between sample and objective lens.

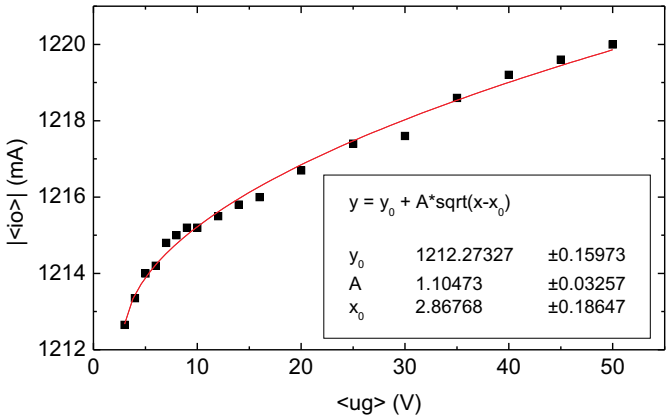

Figure 1.15: Objective lens current $< io >$ as a function of the start voltage $< ug >$.

In PEEM mode, the relation between image plane position and final kinetic energy is linear[10]; the angular coefficient is proportional to the chromatic aberration coefficients induced by the objective lens and the electrostatic mirror. In **Fig. 1.16a** is given an example of a typical $< ug >$ vs $< io >$ graph, in which the linear relation is clearly visible. The graph shows the data taken with fixed C_s value and for different C_c values induced by the electrostatic mirror. By taking data over all C_s and C_c values, one can check that a change in C_s has no influence on C_c (**Fig. 1.16b**) and can calculate the average slope value for different C_c (**Fig. 1.16c**).

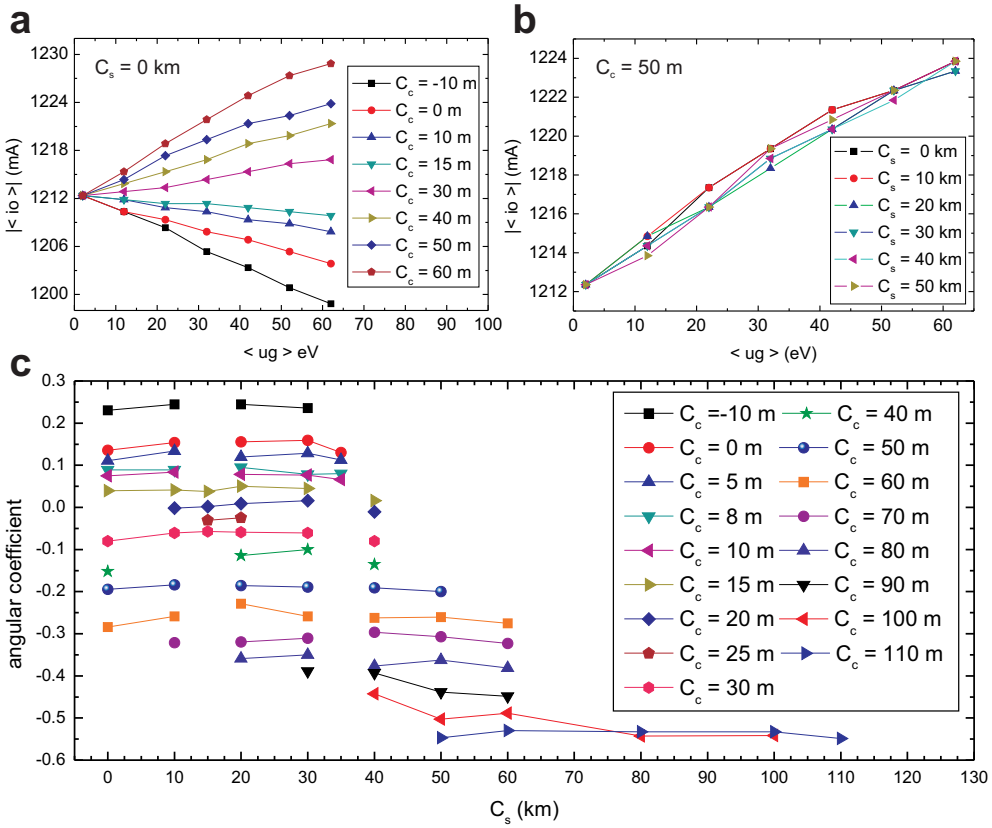

Figure 1.16: (a) Change of the focal plane position in function of $< ug >$ for different C_c values of the mirror. (b) Change of the focal plane position as a function of $< ug >$ for different theoretical C_s values of the mirror. (c) Diagram of the angular coefficient $< io >/< ug >$ for different theoretical C_s and C_c values.

As in the case of spherical aberration, a perfect compensation is achieved when the chromatic aberration coefficient induced by the mirror cancels the one of the objective lens, i.e. in the compensated system no shift in the image plane position is induced by a change of the electron kinetic energy. This condition is satisfied if the slope of $< io >$ vs $< ug >$ measured in the PEEM mode is equal, but opposite in sign, to the one in LEEM mode; in this way one effect compensates the other and the total chromatic aberration coefficient is zero. It is important now to remark that the chromatic aberration coefficient depends on the initial kinetic energy E_0. This means that a single setting of the mirror potentials can correct the chromatic aberration only for a particular $< ug >$. Therefore,

$< ug >$ (eV)	5	10	15	20	30	40	60	80	100	150	200	250
C_c^{mirror} (m)	80	55	48	43	39	36	33	31	30	28	27	26
C_c^{mirror} (m) th	39	29	24	22	19	17	15	13	12	11	10	10

Table 1.1: C_c value of the mirror that gives a perfect aberration compensation for a selected $< ug >$, in comparison with the theoretical values calculated via simulation.

in order to keep the maximum performance, one has to set up the mirror potential as a function of the $< ug >$ value required by the experiment. **Table 1.1** presents the theoretical values of C_c induced by the mirror that produce an aberration-free system, for different values of $< ug >$.

1.4 Resolution analysis

SMART has already demonstrated that an electrostatic mirror as aberration corrector improves the performance of the microscope. In LEEM mode, a lateral resolution of 2.6 nm has been achieved[11], by showing the well-known 22x$\sqrt{3}$ herringbone reconstruction of the Au(111) surface. This was the first direct observation by a LEEM instrument, what was only possible due to the aberrations correction. By that time, this was the world record for this kind of electron microscope. In parallel, the Omega-filter installed in SMART permits to achieve an energy resolution lower than 180 meV, which has been demonstrated with Ag 3d photo-emission core level electrons.

In the following, an extended analysis of the performances of SMART is presented, with particular focus on the lateral end energy resolution that can be achieved in XPEEM, and on the transmission enhancement in the case of perfect aberration compensation, that derives from the possibility to open the acceptance angle without deterioration of the lateral resolution.

1.4.1 Au on W(110)

One of the systems used as a benchmark for this kind of test is a sub-monolayer deposited film of Au on W(110) surface. There are several aspects that lean out towards

this system, for example the high cross section of Au atoms for X-rays, the very small thickness of the system, in order to avoid undesired distortions of the image due to local field enhancement, the kind of growth on the tungsten surface selectable with the temperature and the relatively easy procedure to clean the W surface.

The W sample was cleaned by keeping the specimen at 1300 K in an oxygen atmosphere (partial pressure 1x10^{-6} mbar) for 15 min, followed by annealing at about 2000 K in UHV for less than 30 s. After several cycles, the surface presented in LEEM no trace of carbon agglomerates at room temperature, but a well ordered step structure, while in LEED every diffraction spot was surrounded by satellites referable to the presence of some residual diffused CO on the surface. The sample was therefore kept at 1000 K to minimize the CO contamination after the cooling. At this temperature the Au deposited wets the surface, with the formation of large monolayer domains growing from the atomic step of the W sample. For the deposition a Focus EFM3 evaporator has been used, equipped with a Mo crucible in which the Au was melted. Typically, an overall amount of about 0.5 ML gold was deposited with a deposition rate of about 1 ML/min. This results in the growth of large domains of Au separated by broad areas of uncovered W(110), yielding in a strong chemical contrast in the XPEEM images. The border between these domains was used for testing the spatial resolution of the microscope: by fitting the edge profile with an error function (convolution of a Heaviside function with a Gaussian) one extracted the FWHM of the Gaussian, which is the instrumental resolution.

1.4.2 Effects of aberrations

As shown in Section 1.3.1, the resolution is limited by the aberrations of the lens system. SMART uses the electrostatic mirror to introduce additional aberrations which can compensate for the intrinsic ones. Due to the (nearly) free choice of the spherical and chromatic aberrations, the microscope can work in aberration-corrected (AC) or non-aberration-corrected (NAC) regime, depending of the mirror settings. LEEM and XPEEM images were taken in both cases with different contrast aperture size in the range between 10 and 100 μm (**Fig. 1.17**), corresponding to a variation of the acceptance angle between 28 and 280 mrad. The acquisition time for every XPEEM image

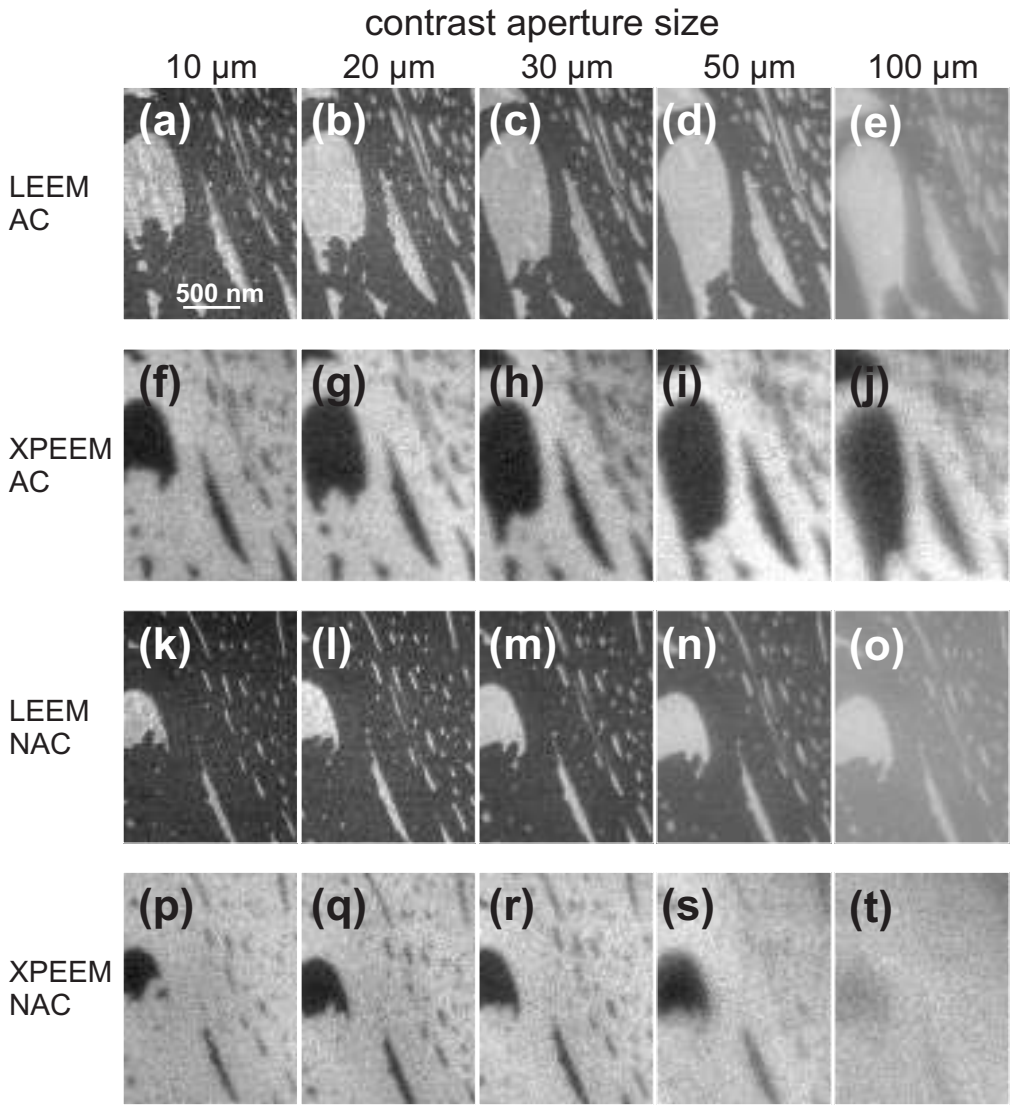

Figure 1.17: LEEM (a-e, k-o) and XPEEM (f-j, p-t) images of an incomplete Au layer on W(110). The kinetic electron energy was E_0 = 113 eV. XPEEM used the Au 4f photoemitted electron excited by photons with hν= 200 eV. The top two rows are aberration corrected (AC), the bottom two are not (NAC). From the left to the right column the contrast aperture was increased from 10 μm to 100 μm. The image intensity scaling for LEEM and XPEEM images was kept constant, respectively. To compensate the change in image intensity, the acquisition time of the XPEEM images was matched to the area of the contrast aperture: 1800 s, 450 s, 200 s, 72 s and 18 s for f-j and p-t. The acquisition time in LEEM is always 5 s. The displayed FoV is 1.5x2.0 μm^2, the images are cut out of an original FoV of 3.11 μm.

were matched to the aperture size to keep the overall image intensity constant. After the Au deposition, the temperature was lowered to 750 K to prevent fast desorption of gold atoms and the destruction of the film. Nonetheless, during the total measurement time of more than four hours, the Au film was not completely stable: the holes were reasonably shrinking. Every series of images show the sharpness worsens for larger aperture sizes. At large apertures (i.e. large acceptance angles) the effect of the aberration correction is clearly visible. The corresponding resolution values are summarized in **Fig. 1.18** for the corrected (blue data points) and non-corrected (black) mode, and for XPEEM (in full symbols) and LEEM (in open). The theoretically expected resolution limits are added as straight lines; for the dashed ones a constant offset is assumed.

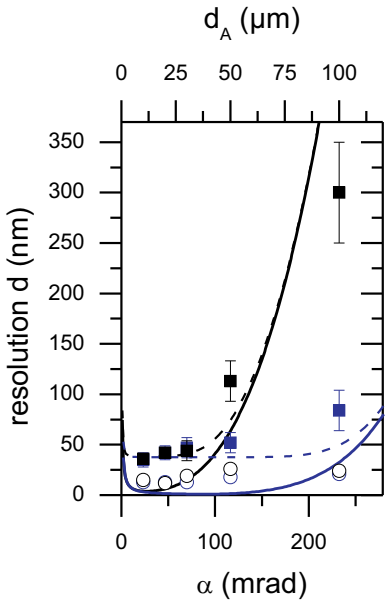

Figure 1.18: Lateral resolution for the LEEM (open symbols) and XPEEM (solid symbols) images in Fig. 1.17 for the aberration corrected (blue) and the non-corrected (black) case, plotted versus the aperture size d_A, from which the acceptance angle α is calculated. The experimental data points are well described by the theoretically expected resolution limits (solid lines), whereas two different constant offsets are additionally assumed (dashed and dash-dotted lines).

The graph in **Fig. 1.18** demonstrates two strong effects of the aberration corrector in XPEEM. Firstly, in the AC mode a moderate resolution (80 nm) can be achieved with an acceptance angle more than twice as large as in the NAC mode, i.e. the transmission is increased by a factor of five. Secondly, a drastic improvement of resolution is observed at large apertures. On the other hand, in LEEM the resolution data do not depend significantly on the acceptance angle, mainly because the reflected electrons are diffracted coherently with long range order[12]. However, for low acceptance angle the system did not response as expected, with the XPEEM resolution much worse than in the LEEM case, while they should be in principle the same because of the identical optical setting used at the same energy broadening of 0.5 eV for the imaged electron beam. In XPEEM an offset of 40 nm was observed, far away from the detection limitation of 10 nm for the used field of view and noticed in LEEM. A possible explanation can be the thermal drift, always present and even strong when the sample temperature is as high as in this case. Despite the very long acquisition time for small apertures (45 s for a single image), one can exclude that the thermal drift may have such a big influence, because a comparable resolution is measured even for a 50 μm contrast aperture at a correspondingly shorter acquisition time of 10 s. The real explanation for this behavior has been deduced by further experiments regarding the so-called space charge effect.

1.4.3 Space Charge Effect

The space charge effect is the Coulomb interaction that occurs within electrons compacted in a bunch. When electrons are emitted from a sample and collected on a detector via electrostatic or magnetic lenses, it could happen that the electrostatic repulsion is high enough to affect their trajectories and modify their kinetic energy, destroying therefore the carried information. This effect is regulated by the spatial density of electric charge: if the bunch of electrons is too concentrated the Coulomb interaction becomes not negligible. In literature the space charge effect has been reported among others in XPS[13] and UV-PEEM with pulsed lasers as photon sources[14,15]. In XPEEM the first article that addresses this effect has been published by Locatelli *et al.* in 2011[16], more or less one year after the experimental session in which the data presented here were collected and analyzed. The experimental procedure we used is similar to the one used by

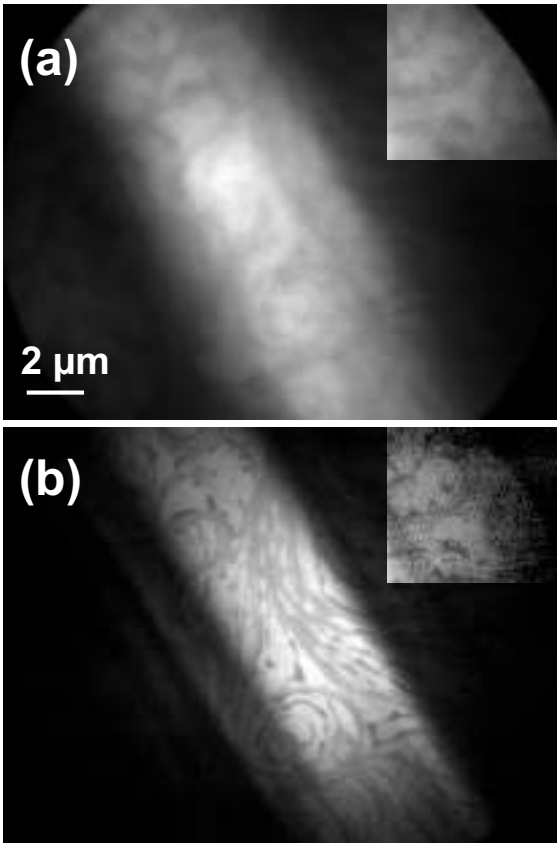

Figure 1.19: XPEEM images of the illuminated sample area, taken with secondaries at E_0 = 2 eV with an energy resolution of 0.5 eV, set with the energy filter, at a photon energy of hν = 167 eV. The photon flux is 9x10^{12} ph/s and 0.8x10^{12} ph/s in (a) and (b), respectively. The image intensity scaling is 0-4000 cts (inset: 0-600) for (a) and 0-600 cts (inset: 0-80) for (b).

Locatelli: measure the spatial resolution in function of the photon flux and for different conditions.

Fig. 1.19 shows two energy filtered XPEEM images taken at the intensity maximum of the secondaries, at E_0 = 2 eV and with an energy filter resolution set to 0.5 eV. The field for view a larger than the area illuminated by the soft x-rays; therefore one can directly see the elongated intensity profile of the illuminating beam. Both images show the same area on the surface, but with different X-ray beam intensity (the detected image intensities are rescaled to their maximum to improve the display). Clearly, the image with lower intensity (**Fig. 1.19b**) is much sharper than the one with higher intensity

(**Fig. 1.19a**). This proves that a space charge effect occurs in the electrons that are flowing from the sample to the detector: the high intensity of the photon beam leads to a blurring of the image. Once established that the resolution correlates with the intensity of the photon beam, we proceed to investigate the nature of this phenomenon and to determine the physical parameters that play a crucial role.

In **Fig. 1.19** we additionally compared the image resolution in the center of the illuminated area with the one found in a side area, with less intensity, about 10 μm away from the maximum. The sharpness of this side area is visible in the insets in the upper right corners of each image, where the intensity is rescaled. Remarkably, the lateral resolution for both areas is the same, what means, it is not determined by the local photon flux on the surface. From this we can conclude that the space charge effect is not produced at the sample surface, but during the entire flight from the objective lens to the detector.

The significant difference between LEEM and XPEEM resolution measurement leads to the different time structure of the resulting electron beam. Despite the total electron current on the detector is comparable, the electron beam intensity is continuous in time in LEEM, while pulsed in XPEEM. This time structure reflects that of the synchrotron radiation source, which consists of periodic X-ray pulses of some tens of picosecond of length separated by a delay time of about 2 ns. This means that the overall intensity in XPEEM is condensed in 2 to 4% of the total time, while the rest of time is darkness. Therefore, the electron current in the short XPEEM pulse is 25 to 50 times higher than in LEEM: this leads to a much stronger Coulomb interaction that can explain the resolution offset between the two imaging modes. In order to verify this and to study the influence of the time structure, we compare the intensity dependence of the lateral resolution for different regimes of pulsation. During a semester, BESSY provides several different modes of synchrotron radiation, among others the multi-bunch (MB) and the single-bunch (SB) (**Fig. 1.20**). In the first one, 320 of 400 possible bunches per circle are filled with electrons and emit light; in the second one only one bunch is used. In both cases the resolution decreased with intensity. Normalizing the flux per bunch for the data collected in the multi-bunch (see MB*, black filled data points in **Fig 1.20**), the two datasets converge well together to a single trend. The slight discrepancy might be explained either by the assumption that the pulse in the SB mode was broader than the MB mode leading to weaker maximum peak intensity or the photon detection in the

two beam times was slightly different. Anyway, from this observation we conclude that the overall beam intensity does not automatically determine the space charge effect, but the photon flux, i.e. the intensity per time, which is very crucial for pulsed sources.

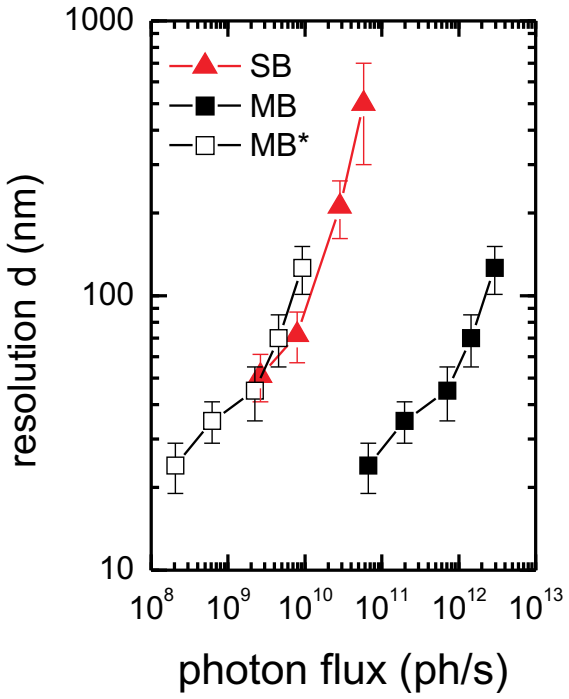

Figure 1.20: Effect of the pulsed time structure: resolution dependence in XPEEM on photon flux for multi-bunch (MB) and single bunch (SB) operation mode. For MB* the photon flux of one bunch was calculated.

Once established the presence and the nature of the space charge effect in SMART, the next step is to study in which element of the microscope this effect is produced and, with this knowledge, which strategies can be set to avoid it and bring the resolution to its physical limit. The scheme of the SMART setup showed in **Fig. 1.1** helps to figure out the possible elements in which the electron cloud is dense enough to produce space charge effect. One can straightaway notice several possible cross-over points: interme-

diate image planes in which all electrons emitted from a particular area are concentrated in one point, and diffraction planes where electrons the same emission angle are focused in one point. One might expect that the space charge occurs exclusively in these special regions. This option can be rejected for two reasons. Firstly, we have already shown that there is no additional blurring proportional to the intensity in the source plane (**Fig 1.19**). Secondly, the reduction in size of the contrast aperture and the consecutive cut of the electrons with larger emission angle does not lead to a big improvement when the system is aberration corrected (**Fig. 1.18**). After the aperture there are still a few image and diffraction planes, but the reduction in intensity by a factor of 25 (obtained with a reduction in size from 50 to 10 μm of the contrast aperture) does not enhance significantly the resolution. The other critical points in the SMART setup are the ones in which the electrons have a very low kinetic energy: the objective lens and the mirror. In both the electrons are not passing through with 15 keV of kinetic energy, but are slowed down or accelerated by a field. Therefore there is a certain amount of time in which electrons are compressed in a very small region of space and standing still or move with very low speed. In this moment the Coulomb repulsion can greatly change the trajectory of the electrons and degrade the carried information. In order to differentiate whether the objective lens or the electrostatic mirror is mainly responsible for the blurring, we have compared the resolution of XPEEM images collected with and without a field aperture placed near the entrance of the beam splitter (i.e. between the objective lens and the mirror) and for different intensities of the photon beam. The field aperture is 100 μm wide (which correspond to a selected area of 5 μm in the image plane) and permits to cut away a large fraction of the electrons photo-emitted from the side areas (**Fig. 1.21a**), which are not used for imaging at high magnification. Its introduction brings an evident improvement of the resolution, particularly with high X-ray intensity in which 90% of the electrons are emitted from side areas. In **Fig. 1.21b** the resolution d is plotted versus the initial electron beam current j_0 at the sample surface (in linear scale), while in **Fig. 1.21c** the identical data d versus the electron beam current j_1 behind the field aperture (in logarithmic scale). Clearly, for the same photon flux, and, therefore, the same initial electron flux j_0, the field aperture improves the lateral resolution by a factor of about 2. This demonstrates that a strong contribution to space charge effects occurs on the electron path behind the field aperture, very likely at the cross-overs in the beam splitter and at the reverse point in the electron mirror. Nevertheless, the number of electrons

between the sample surface and the field aperture still plays a role. This is documented by the increase of resolution with field aperture j_0 = 1500 cts in **Fig. 1.21b** or correspondingly at j_1 = 80 cts in **Fig. 1.21c** (red open data points). Here the opening of the ID apertures causes only a broadening of the illuminated spot, but no intensity increase in the center of the spot. This means, the initial intensity j_0 is increased, but not the intensity j_1 passing the field aperture.

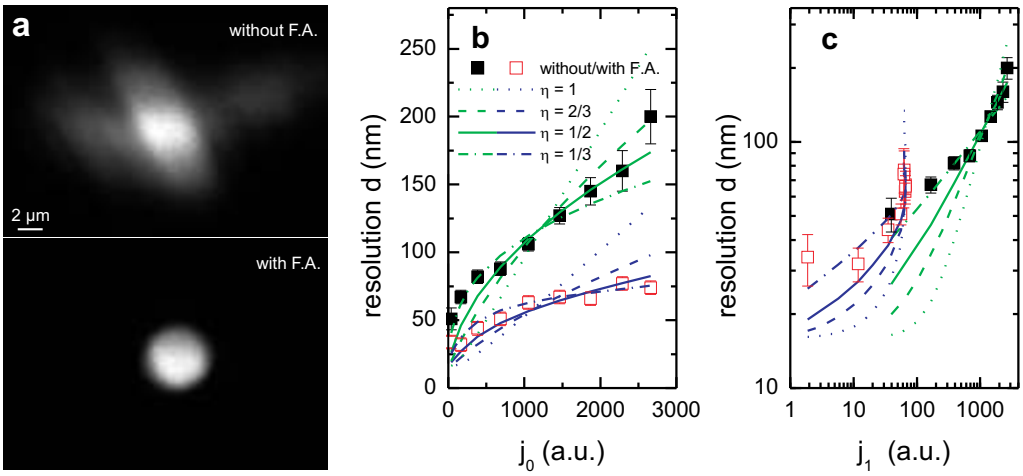

Figure 1.21: Influence of the electron beam current on the lateral resolution. (a) XPEEM images of the secondaries without and with the field aperture. (b) and (c) intensity of the electron beam in front of and behind the field aperture (F.A.), respectively. For the full black data points the entire beam intensity j_0 passes the system up to the contrast aperture, whereas for the open red data the F.A. was introduced into the first intermediate image plane, reducing the overall beam current to j_1. Kinetic energy of the electrons was E_0 = 2.8 eV, photon energy hν= 180 eV, the energy slit was set to 0.5 eV, and the contrast aperture had a diameter of 30 μm. The photon flux was varied between j_{ph} = 1x10^{11} ph/s and 7x10^{12} ph/s. In the XPEEM image, the photon flux is 1x10^{11} ph/s. The various lines on the graphs depend on the choice of the exponent and are described by the formula for d given in the text.

The resolution data d can be described by a Gaussian convolution of two power laws and the detection limit d_0 (see Section 1.3.1):

$$d = \left((Aj_0^{\eta})^2 + (Bj_1^{\eta})^2 + d_0^2\right)^{1/2} \tag{1.11}$$

where $j_1 = j_0$ for the case when no field aperture is used. The best fitting exponent to describe both curves in **Fig. 1.21b** and **1.21c** is η = 1/2, which is in agreement with the theoretical prediction of Refs. 17,18. In contrast, the experimental data in Ref. 16 can be described by a linear dependence. For η = 1/2 the ratio B/A is about 2, indicating a stronger influence of the space charge on the path behind the field aperture compared to the path between sample and field aperture.

The residual effect, present even if the field aperture is inserted, can be produced by other two factors. The field aperture selects indeed only the useful electrons in the space region, but it does not in the diffraction region and in energy. One has to remember that electrons with different emission angle are all collected by the microscope, and as well all electrons with different kinetic energy, which are filtered only at nearly the end of the path by the Omega-filter. Unfortunately the SMART setup does not allow an intervention on these before the electrons pass through the beam splitter and the mirror. In principle, acting on the diffraction plane and the energy distribution could reduce the density of the electron cloud by an additional factor of 100 (cutting 90% of the electrons with a large angle photoemission angle and removing the secondary electrons for XPEEM images). If a reduction of a factor 10, as demonstrated in the case of the field aperture, bring the resolution from 100 to 40 nm, it is reasonable to think that the action on the other two factors could improve the XPEEM resolution to values comparable to LEEM, i.e. below 10 nm.

1.4.4 Final resolution and further improvement

Basing on this knowledge, we optimized the setup to gain a better lateral resolution, e.g. by reducing the photon flux and increasing the acquisition time and the magnification to reduce the limitation by the detector. To avoid the influence of the thermal drift, sets of images were taken at shorter acquisition time and afterwards summed up with numerical shift compensation. **Fig 1.22** displays the result of 100 images of 30 s each. The images were taken with the W 4f XPS-peak, which represents pure chemical contrast. The

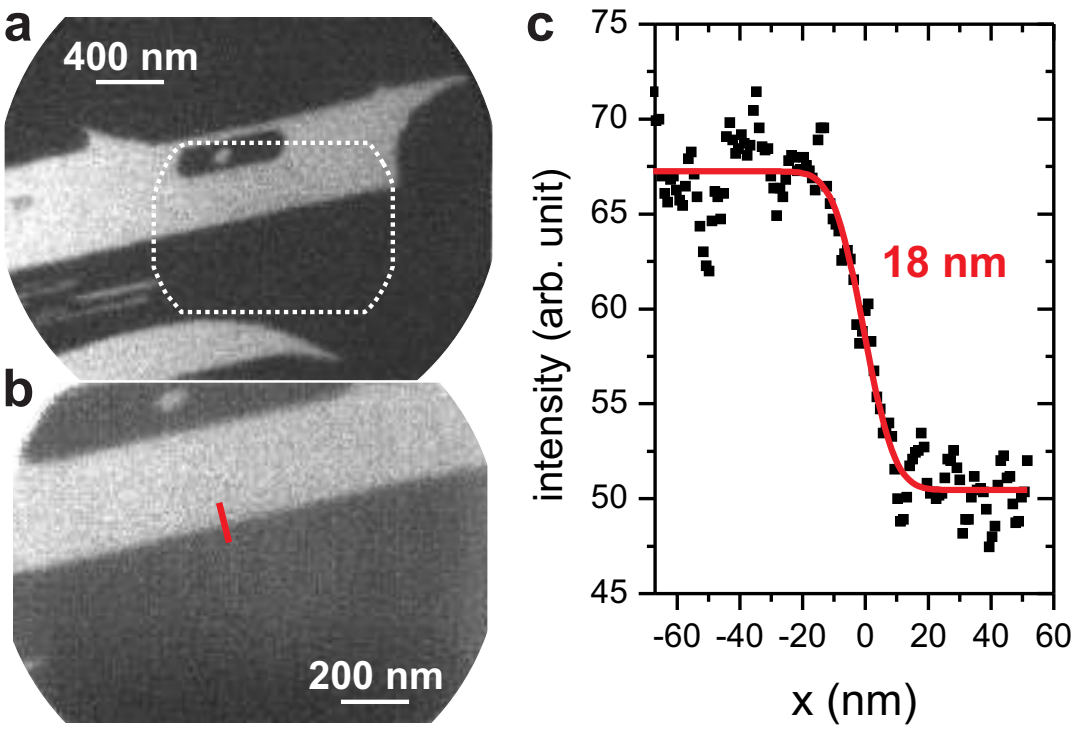

Figure 1.22: Lateral resolution in XPEEM using W 4f at kinetic electron energy of E_0 = 165.2 eV and photon energy of hν= 200eV, j_{ph} = 8x10^{11} ph/s (a) and 2x10^{11} ph/s (b), c.a. = 30 μm, acquisition time 200 s and 3000 s. The Au covered areas appears dark in the XPEEM images, whereas the W substrate is bright. (b) is a zoom-in of the overview image (a) (see marked area). The graph in (c) shows a cross section at the border between substrate and Au domain (red line in b). The fit with an Error function yields in a lateral resolution of 18 nm.

cross-section through the border between Au domain and W substrate along the red line is displayed in **c**. The fit by an error function gives a lateral resolution of 18 nm. This value is the best reported so far for an XPEEM with chemical contrast. Locatelli *et al.* reports a resolution of 50 nm at the same system, but with lower magnification and using the Au 4f intensity. In the same paper the resolution of 35 nm was shown using secondary electrons and Pb 5d photoelectron. As a test system, about 30 nm high three dimensional Pb islands were used. A similar system with three dimensional Ag islands was used to demonstrate a lateral resolution of 22 nm with secondary electrons[19]. However, at high three-dimensional islands the local electric field is distorted, leading to image distortion and local change of magnification. Therefore, a confusing effect on the sharpness cannot be excluded, especially when the height of the objects (20 to 30 nm) is in the range of the lateral resolution, measured at the rim of the objects[20].

The knowledge collected so far is very useful also to optimize the design for SMART-II, the improved aberration-corrected spectro-microscope which gains from the experience acquired in the SMART project and is currently under development in this workgroup. Here some options are summarized which can be taken into account to improve the lateral resolution in XPEEM.

1. Time structure of the synchrotron light source: the pulsed time structure is the main origin for the negative effect of the space charge. An elongation of the pulse structure or more filled bunches per circle would relax the difficulties.

2. Improved focusing of the illuminating photon beam onto the sample surface: one should avoid that useless electrons originated outside the field of view would pass through the microscope and contribute to the beam intensity. This can be achieved in two way:

   (a) optimizing the refocusing optics to an enhanced demagnification of the light source, this means to concentrate the intensity in a smaller spot size and/or

   (b) using apertures in the intermediate planes in the beamline, e.g. the energy exit slit plane, to reduce the spot size and therefore the total intensity by cutting away intensity from the side.

3. Electron beam: here in three different plane, the intensity of the electron beam

must be reduced as soon and as much as possible to avoid the space charge effect on the path to the electron mirror:

(a) Selection of acceptance angle: an aperture in the backfocal plane of the objective lens reduces the beam intensity by cutting away the large starting angle;

(b) Real space selection: an aperture in the first intermediate image plane cuts away all the electrons outside the field of view, so that they do not contribute anymore to the beam intensity.

(c) Energy selection: a high pass energy slit in the first dispersion plane of the magnetic beam splitter filters away the high intense secondary electrons tail. Only the wider energy range around the interested XPS peak is passed through.

4. Detection: a detector with a higher sensitivity and larger number of pixels can lead to use lower photon beam intensity.

Those arrangements to reduce the space charge effect, together with a higher stability that allows a longer acquisition time in case of a reduced flux, will result in a higher resolution. Although the electron mirror which we use as an aberration corrector is very sensitive to space charge effect, the advantages of the aberration correction overweigh this disadvantage. Due to increase in transmission a larger portion of the photo-emitted electrons can be used for the imaging. Therefore the photon flux can be reduced, which on the other hand limits the space charge effect.

Chapter 2

Fe_3O_4/Pt(111) thin film: growth, defects and inhomogeneities

Magnetite (Fe_3O_4) is an iron oxide that has inverted cubic spinel structure, with tetrahedral sites occupied by Fe^{3+} ions, whereas octahedral sites are randomly occupied by Fe^{2+} and Fe^{3+} ions with equal concentration. It is the most ancient magnetic material known; usually a ferrimagnet with a Curie temperature of 850 K[21], it becomes multiferroic at low temperatures[22]. For an oxide, the conductivity is relatively high (250 Ω^{-1} cm^{-1}). It has a half-metallic character[23], i.e. the electronic band structure changes with the spin orientation of the charge carriers, due to the highly spin-polarized density of states in the conduction band. At temperatures below 120 K, magnetite undergoes the so-called Vervey transition[24], a charge ordering of Fe^{2+} and Fe^{3+} states in the octahedral sites that leads to a metal-insulator transition[25]. Fe_3O_4-based films show, also, a large magnetoresistance[26]. With all these peculiar properties, Fe_3O_4 has a wide range of technical applications, for example in spintronics, where magnetite is used for the construction of magnetoresistance devices[27]. However, in the heterogeneous catalysis magnetite has been more extensively used, both for industrial production and scientific investigation. Iron-based catalysts have been used for the ammonia production, first by W. Ostwald (1900) and F. Haber (1904) for their fundamental studies[28], and then by F. Haber and C. Bosch (1909) for the industrial-level production via the *Haber-Bosch* process. The ammonia synthesis is a milestone for the heterogeneous catalysis not only for the huge impact in the modern society, but also for the elucidation of the production mechanism, with a major contribution by G. Ertl[29,30], that has paved the way for the

development of modern surface science.

Magnetite model catalysts, like single crystals or thin films grown on single crystal support, have been investigated in details in the last decades[31] for study the physical origin of its functional properties. Nevertheless, Fe_3O_4 is still a hot topic in the surface science community. Some important aspects are nowadays under controversial debate, mainly regarding the strong dependence of the surface properties on the preparation conditions e.g. (i) using a single crystal instead of a thin film grown on a crystalline support, (ii) different oxidation temperatures and/or (iii) oxygen partial pressures. As a short overview of the various structural models proposed up to now, we cite first of all the LEED analysis of Barbieri *et al.*[32] and Ritter and Weiss[33], who suggested the 1/4 monolayer (ML) of Fe over a close-packed O layer as the most favored atomic termination of a $Fe_3O_4(111)$ thin film grown on a Pt(111) surface. However, TPD, IRAS and HREELS studies of adsorbed CO as a probe molecule suggested a surface terminated by 1/2 ML of iron[34]. Condon *et al.*[35] observed with STM and LEED the formation of the so-called "biphase" surface at low oxidation temperatures on Fe_3O_4 single crystal. This was later found also in magnetite thin films on Pt(111) by Shaikhutdinov *et al.*[36]. Shvets *et al.*[37] suggested the formation of a O-terminated surface with superperiodic features when a $Fe_3O_4(111)$ single crystal is cooled down after oxidation while maintaining the oxygen exposure. Such variability in the surface structure may only be understood via a more systematic and comprehensive study of the various parameters that influence the preparation process. The knowledge of the effects of the different preparation parameters is crucial for a correct comparison of the existing results, for merging them into a clear and unambiguous global picture and for tailoring the film properties depending on the goal of future experiments. Moreover, modifications in the preparation recipe could lead to an improved surface structure, morphology and domain structure of the magnetite thin film, as well as the related physical properties, such as magnetic properties, chemical reactivity and nucleation and encapsulation of nanoparticles[38].

The $Fe_3O_4(111)$ surface has been investigated therefore by several experimental techniques available nowadays. These methods nonetheless have a blind spot: they are applied to an already formed sample, i.e. they are able to examine surfaces *after* the preparation, and not *while* the film is produced. To overcome this limitation is especially important for cases like the magnetite, in which the preparation conditions have

such a big influence. Having this in mind, the capability of a spectro-microscope to observe the surface *in-situ* and *in real-time* during the preparation with nanometer resolution can be extremely helpful to sort out the effect of every known parameter and to discover new factors that can play an unexpected crucial role. With SMART one has full control over the surface: in addition to study in real-time the effect of a parameter variation, one can switch between several comprehensive probing techniques (microscopy, spectroscopy or diffraction with reflected or emitted electrons) within seconds, all applied on the same surface area. The *in-situ* characterization of the surface gains a new kind of completeness.

2.1 Preparation recipe and calibration

We chose Pt(111) single crystal as a support for the magnetite thin film because of the easy the preparation and the know parameters to control the growth. Pt(111) is one of the best suited substrate for the magnetite, with a lattice mismatch of 7%. The thin film preparation, widely accepted in literature[36], consists of two parts. First, the substrate surface is covered by a complete monolayer of FeO(111) obtained by dosing a corresponding amount of Fe at room temperature and subsequently oxidizing with 1x10^{-6} mbar of O_2 at 1000 K for two minutes. In the second step the real Fe_3O_4 film is formed by at least three cycles of not less than 5 ML Fe deposition at room temperature and subsequent exposure to 1x10^{-6} mbar of O_2 at 900 K for 5 minutes. This procedure results in a fully closed Fe_3O_4(111) film with an average thickness greater than 5 nm.

Before the deposition, the Pt sample had to be cleaned with several cycles of sputtering and annealing. For the sputtering were used Ar^+ ions with a kinetic energy of 1200 eV. With an Ar partial pressure of 1x10^{-4} mbar the filament current of the sputter gun was increased until the sputtering current measured at the sample is about 7 μA. After 30 min of sputtering the sample was annealed to 1200 K for 5 min. Four cycles were required to remove a (previously deposited) magnetite film with a thickness of 10 nm. In the last cycle, between the sputtering and the annealing, the sample was heated in oxygen to burn the residual carbon species: after keeping the surface in 1x10^{-6} of O_2 for 15 min with a temperature of 700 K, it was annealed to 1200 K in UHV. This

yielded a sharp LEED pattern without structured background. LEEM imaging of the clean Pt(111) surface showed smooth areas of terraces partially more than 1 μm wide, separated by a bunch of some tens of atomic steps.

For the Fe deposition a Focus EFM3 evaporator was used. The iron rod of 99.995% purity (Alfa Aesar) was heated with electron bombardment provided by a W99%Th1% filament. In order to reduce the pressure, the evaporant rod (2 mm thick and 45 mm long) was contained in a liquid-cooled copper cage with a hole in which the evaporant material passes towards the sample. The base pressure in operating conditions was below $1x10^{-9}$ mbar. The water-cooled evaporator was mounted on a side port of the main chamber, pointing towards the sample surface, and could be approached to the sample with a linear drive to a minimum distance of 20 cm. This - compared to other experimental setups - rather large distance was due to the objective lens just 2 mm in front of the sample, which limited the access to the specimen. For this reason the evaporator had to point to the sample under a grazing incidence angle, in our case an angle of 20°. With a heating power of about 15 W, the iron flux has been measured *in-situ* as $4.1x10^{14}$ atoms/(cm^2 min).

2.1.1 Preparation of FeO(111) and calibration of the Fe evaporator

The real-time observation of Fe deposition and subsequent oxidation in LEEM gives access to many details of the formation of the thin oxide film. Above room temperature Fe grow on the Pt(111) surface in a Volmer-Weber mode (i.e. isolated 3D islands), with the size and the density of 3D islands strongly depending on the substrate temperature[39]. At 300 K deposition of 1 ML of Fe resulted in uniformly distributed islands with a width below 20 nm almost fully (approx. 80 % - see **Fig 2.1** series **a**) covering the Pt substrate. In contrast, at slightly elevated temperatures of 350 K the number of islands was considerably lower, the lateral size clearly enlarged to several hundreds of nm (**Fig 2.1** series **b**). This change in morphology was driven by diffusion as the effect is enhanced at higher temperature. This means that thermodynamically Fe does not wet the Pt(111) surface. This tendency to de-wet the surface can only be overcome by decreasing the temperature in order to reduce diffusion, as it is already known for other systems (for example Pb/Si(111)[40] or Pb/Cu(111)[41]). In this respect, the Pt(111) substrate shows a

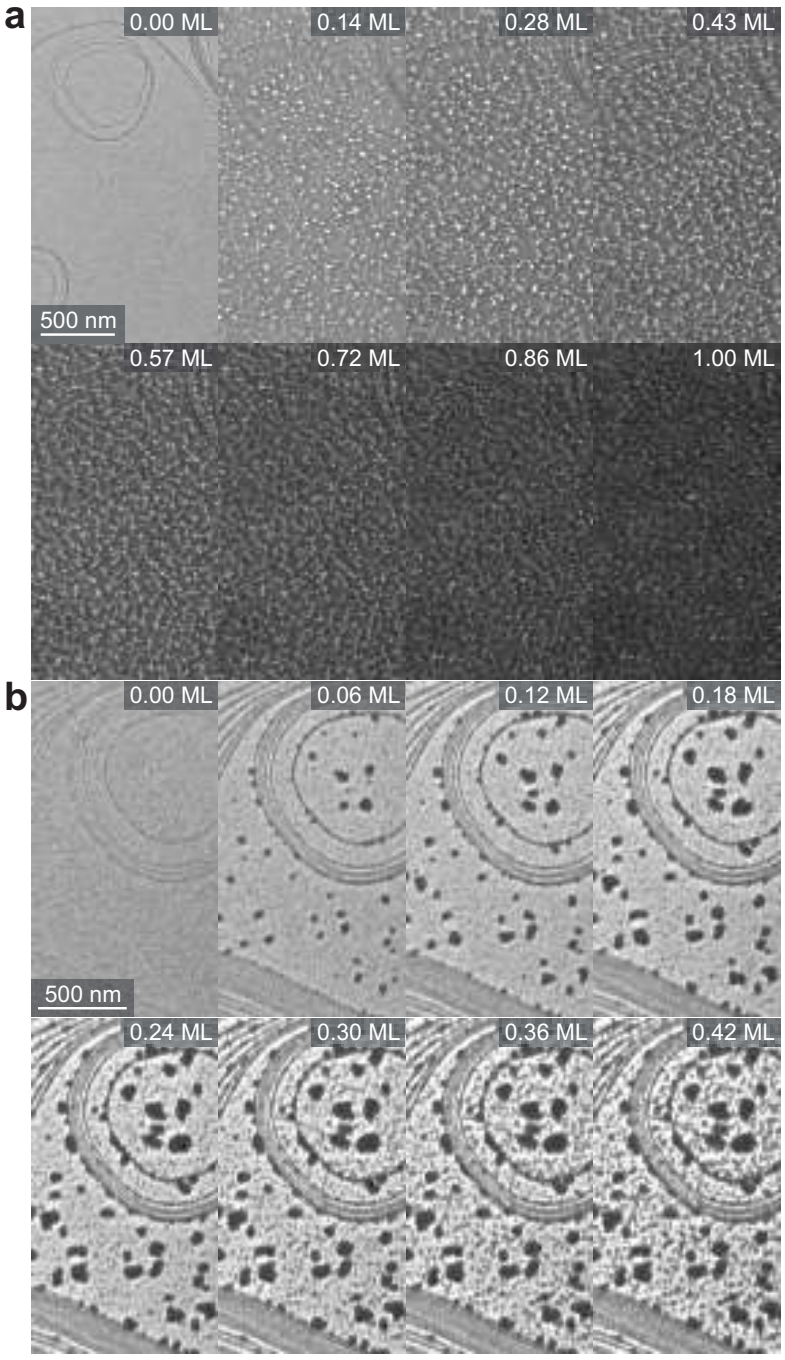

Figure 2.1: Deposition of Fe on a clean Pt(111) surface at 300 K (a) and 360 K (b). The first series has been taken at slight over-focus conditions, E_0 = 17 eV; the second in slight under-focus, E_0 = 6 eV; therefore the Fe islands appear white in (a) and black in (b).

behavior opposite to Ru(0001), investigated by Santos *et al.* with LEEM[42]. Here, the first Fe layer is completely wetting the substrate at 520 K, documented by the merging of large 2D islands into a closed film

In the case of the Pt(111) substrate, the morphology of the first Fe layer strongly influences the subsequent formation of a FeO(111) layer. The Fe film was oxidized at $1x10^{-6}$ mbar of O_2, starting at room temperature, followed by annealing with a rate below 10 K/s up to finally 1000 K, which was kept for 2 min. Upon cooling, oxygen was pumped off not before reaching 500 K. During the annealing in oxygen the contrast in the LEEM image changed at 820 K. At this temperature, the corrugation of the Fe deposited gave way to the formation of large flat area by coalescence of small FeO domains (**Fig. 2.2**). The oxidation was not driven by mesoscopic reaction fronts, but occurred everywhere at the same time, independently from the substrate morphology. This produced an FeO(111) film completely covering the whole Pt substrate, but only if iron was deposited at 300 K. Starting, however, with the more isolated 3D Fe islands grown at 350 K, the same oxygen treatment lead to an incomplete FeO(111) film with well isolated iron oxide islands. This, probably, is related to the different initial morphology of the deposited Fe on the substrate, as well as some Fe depletion due to the segregation of a fractional amount of Fe into the Pt(111) substrate, enabled by the higher deposition temperature[43].

The Fe deposition rate was calibrated using LEEM *in-situ* and in real-time: here 1 ML of Fe is defined as the amount deposited at 300 K which leads to a perfectly closed FeO(111) layer after the oxidation (**Fig. 2.3a**). For Fe amounts slightly larger than 1 ML, the material in excess formed well ordered FeO_x islands of triangular or hexagonal shape[44], which could be easily distinguished from the first FeO(111) layer by the different reflectivity of the electron beam at specific kinetic energies (e.g. 3 eV). The structural quality of the FeO(111) single layer was evaluated by LEED, yielding results comparable to those in Ref. 33. The LEED pattern of FeO/Pt(111) consists of the principal diffraction spots surrounded by satellites, as a consequence of the Moiré pattern created by the FeO film mismatching the substrate (**Fig. 2.3b**). STM analysis in literature[45] shows that the Fe atoms are separated by 3.10 Å and form rows that are rotated by $\pm 1.3°$ against the Pt atom rows. This arrangement leads to a Fe coincidence site on the Pt surface every eight Pt lattice units along the [01$\underline{1}$] direction and two Pt lattice units

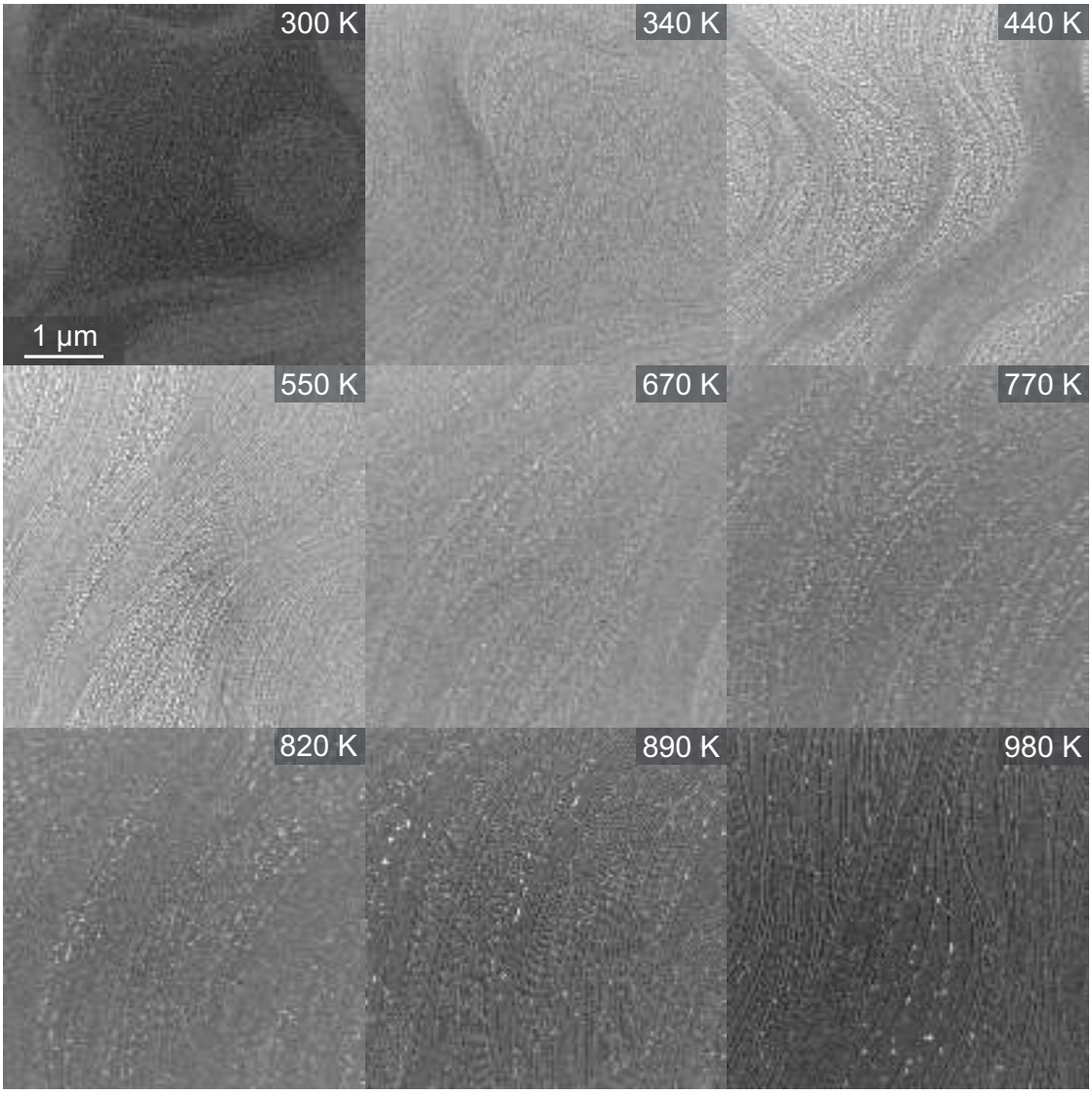

Figure 2.2: Initial oxidation of 1 ML Fe, deposited at RT. The first image displays the starting point at room temperature and in UHV regime. From the second image onward, the sample is exposed to 1x10^{-6} mbar of O_2: the oxidized areas appear brighter. E_0 = 20 eV, under-focus.

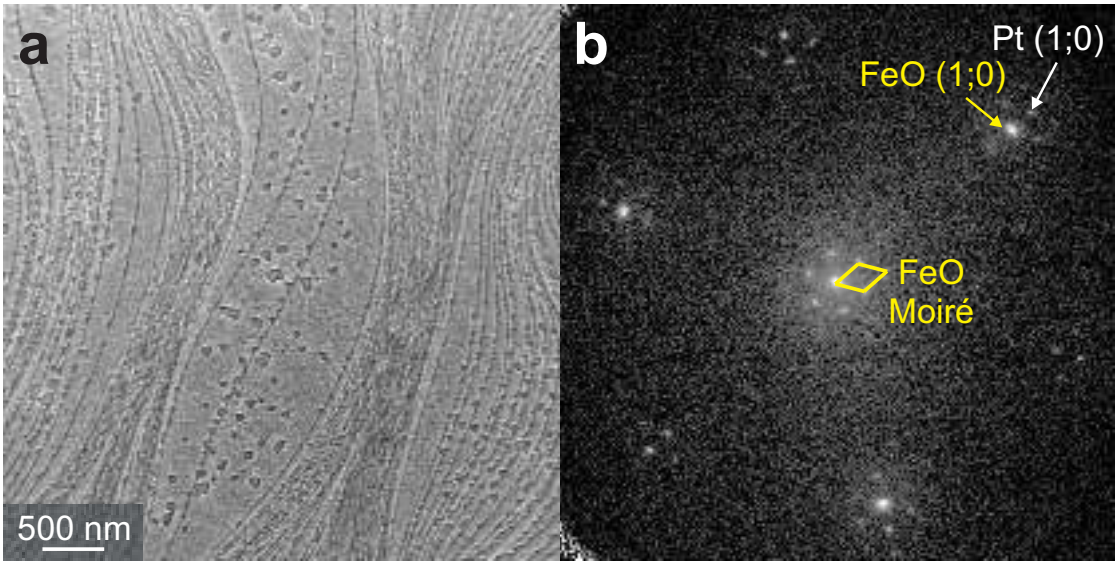

Figure 2.3: (a) Perfectly closed FeO(111) film over the Pt(111) surface. The islands visible on the terraces and along the atomic steps are constituted by a second layer of FeO. E_0 = 20 eV, in focus. (b) LEED pattern of the FeO/Pt(111) surface. The Pt (1;0) spot (in white) and the FeO (1;0) spot and Moiré pattern (in yellow) are highlighted. E_0 = 88 eV

along the [$\bar{1}$10] direction. In this way, a superstructure cell with a lattice constant of 25.4 Å is formed, which is rotated by $\pm 10.9°$ against the (1x1) unit cell of the Pt(111) surface. This superstructure forms the Moiré pattern visible in STM, the diffraction of which produces the satellite spots detected in LEED. It has to be noticed that (i) the first order FeO(111) spots are located closer to the specular beam than the first order Pt spots, because of its larger surface unit cell, and (ii) the satellite spots are actually double spots due to the presence of two possible rotations of the FeO film against the substrate[44].

To get a closed Fe_3O_4(111) film, the FeO monolayer formation is a necessary step because it prevents the segregation of a large amount of iron into the Pt bulk when the temperature arises for the oxidation. However, a small amount of iron could still migrate into the bulk when the temperature is raised up above 500 K. This amount of material is accumulated at each experiment and could influence the substrate during the Fe oxidation. In order to study this phenomenon, the clean Pt(111) surface has been

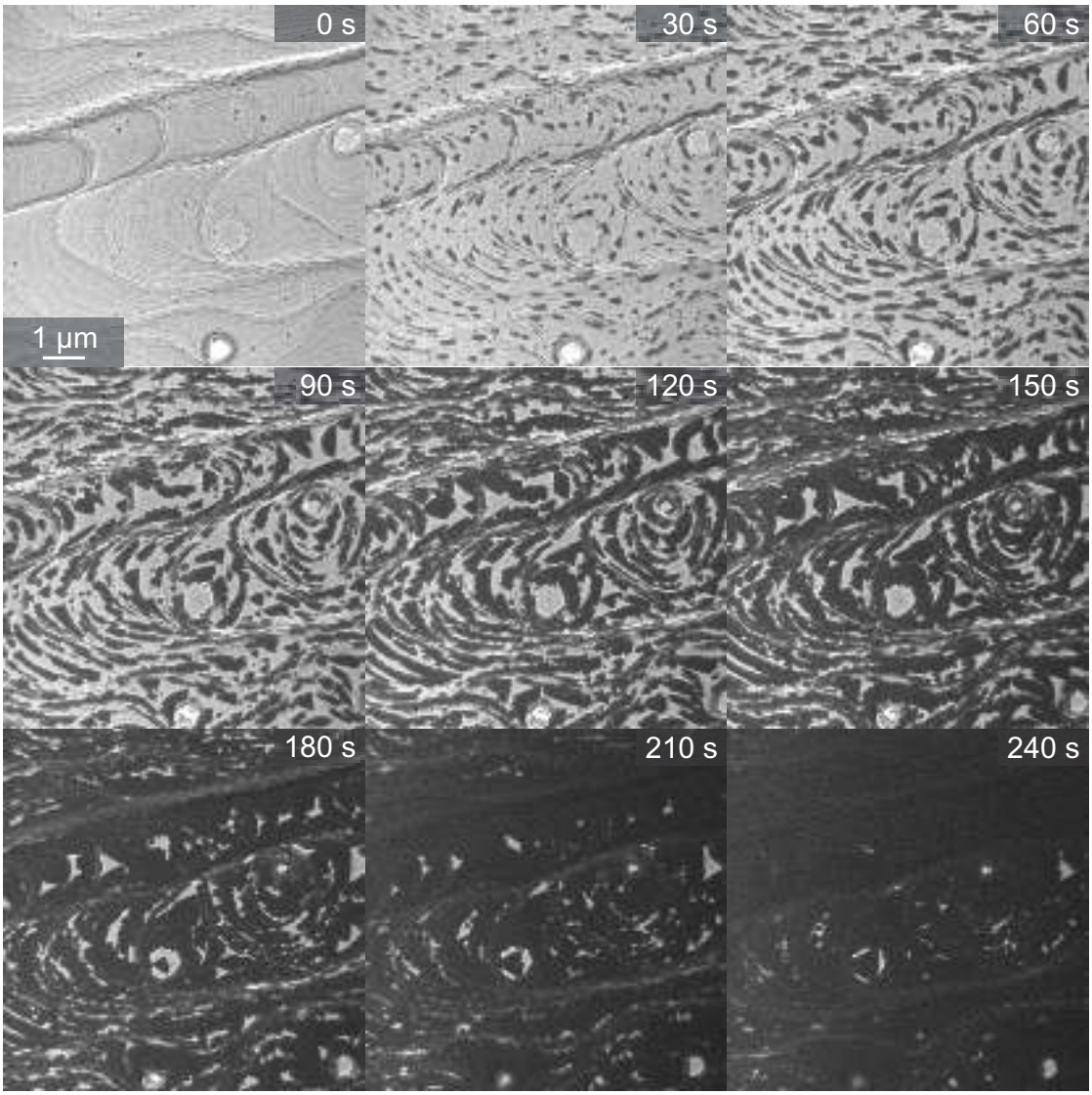

Figure 2.4: Formation of FeO layer by Fe segregation from the substrate bulk. The Pt(111) sample was exposed to $1x10^{-6}$ mbar of O_2 and kept at 1000 K.

exposed to 1x10^{-6} mbar of O_2 at 1000 K. In a couple of minutes (the growth rate increases proportionally with the oxygen partial pressure) the surface was covered by a FeO layer, formed by the material that emerged from the substrate bulk. This is confirmed by the dynamic of the film growth: the FeO film starts to grow at the Pt(111) atomic steps and continues perpendicularly to the steps, refueled by the Fe atoms that emerges from the bulk through the step (**Fig. 2.4**). However, the LEED pattern of this FeO layer differs in details from the FeO layer grown by oxidation of deposited Fe: the sharp double satellite spots are substituted by lines that are perpendicular to the vectors defining the reciprocal unit cell. Dark field LEEM images taken with the smallest contrast aperture (10 μm) centered on the satellite lines show that the film is composed by several domains in which the Moiré pattern differs from the expected one (**Fig. 2.5**). The FeO film created by oxidation of iron segregated into the bulk results distorted, crystallized in a more disordered way compared with the one created with deposited Fe. The quantification of this process is important because the flow of detected material can mislead the calibration of Fe deposition: in fact, the resulted FeO coverage can be enlarged by the additional iron coming from the substrate bulk, with the result that the amount of deposited Fe is overestimated. However, the flux of Fe from the bulk is very low, because several minutes are required to generate 1 ML of FeO at 1000 K. On the contrary, LEEM measurements during the oxidation demonstrate that the process needs just a few seconds when the temperature reaches the oxidation threshold (820 K). For this reason, once the Fe is deposited by the evaporator, the portion of the final FeO coverage that comes from the iron diluted in the bulk can be quantified in the order of only about one percent. Therefore, the calibration of the Fe evaporator is not misled by this effect. Nevertheless, the sample has been periodically depurated by this contamination with several cycles of FeO creation (clean Pt(111) exposed at 1x10^{-6} mbar of O_2 for five minutes at 1000 K) and sputtering.

In order to grow the Fe_3O_4(111) film, a larger amount of Fe was deposited on the complete FeO(111) film at a substrate temperature below 350 K. During the Fe deposition the intensity of the LEEM image gradually decreased and the step contrast slightly change, but dominating features of the substrate morphology like atomic steps and step bunches remained unchanged (**Fig. 2.6a**). This can be explained by the formation of rough agglomerates of Fe, which are smaller than the lateral resolution in the experi-

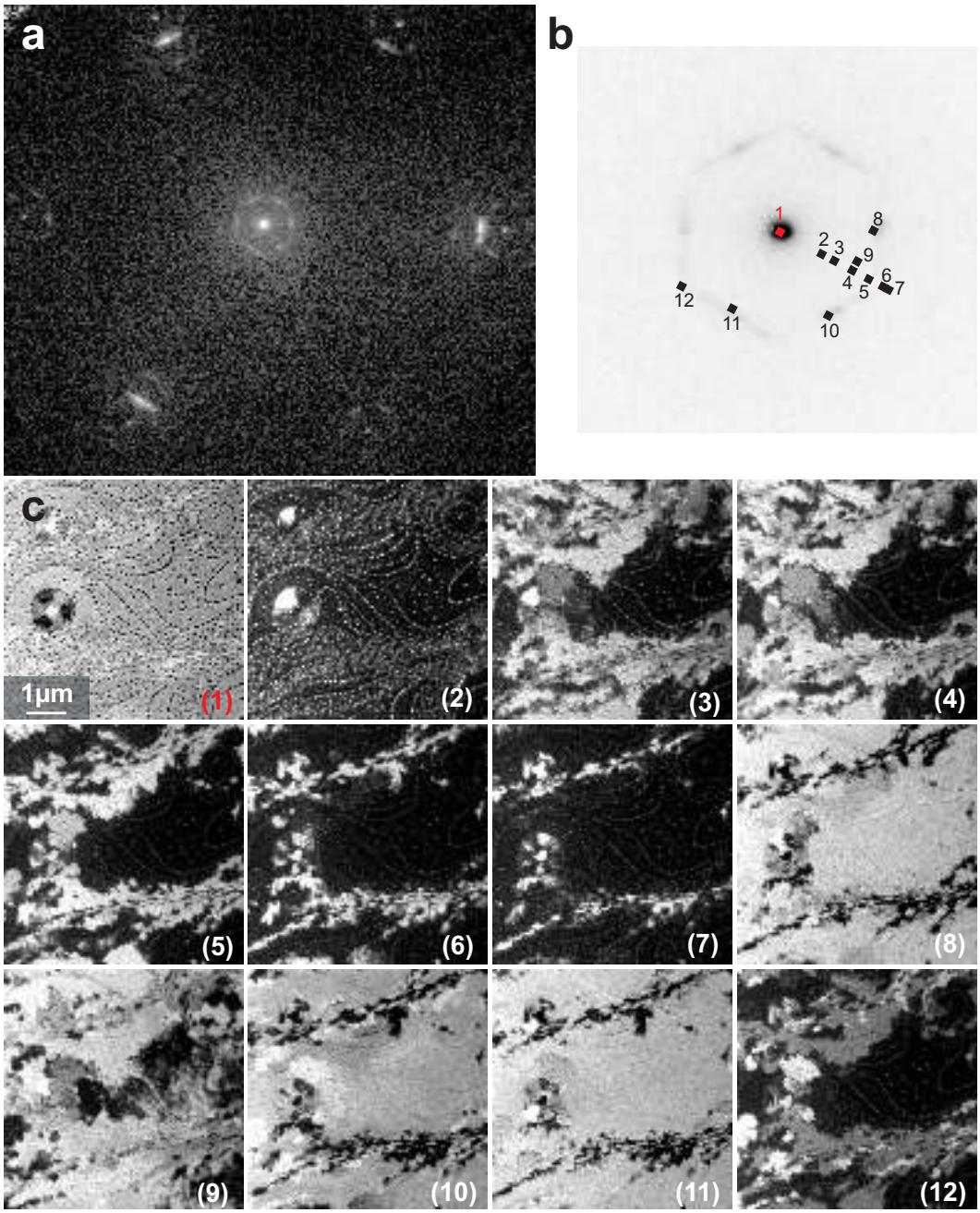

Figure 2.5: Weakly ordered FeO(111) monolayer created with Fe segregation from the Pt bulk. (a) LEED pattern of the FeO layer. The six satellite spots are smeared out along lines, forming an hexagon around the (0;0) spot. E_0 = 88 eV (b) particular of the (0;0) spot and its satellites. The numbered squares indicate the areas from where electrons were collected to form the dark field LEEM images shown in (c). The first image is in bright field mode. E_0 = 15 eV.

ment ($<$ 20 nm). The amount of the deposited material per cycle was varied between 5 and 10 ML, with no appreciable difference in the quality of the resulting oxide films. The oxidation procedure was the same as described above for FeO, but the oxidation temperature was lowered to 900 K and kept for 5 min. LEEM images taken during this process show a change in reflectivity and a contrast recovery when the temperature approaches 840 K. By following this procedure it was possible to produce Fe_3O_4 films, completely closed over the entire sample (**Fig. 2.6b**).

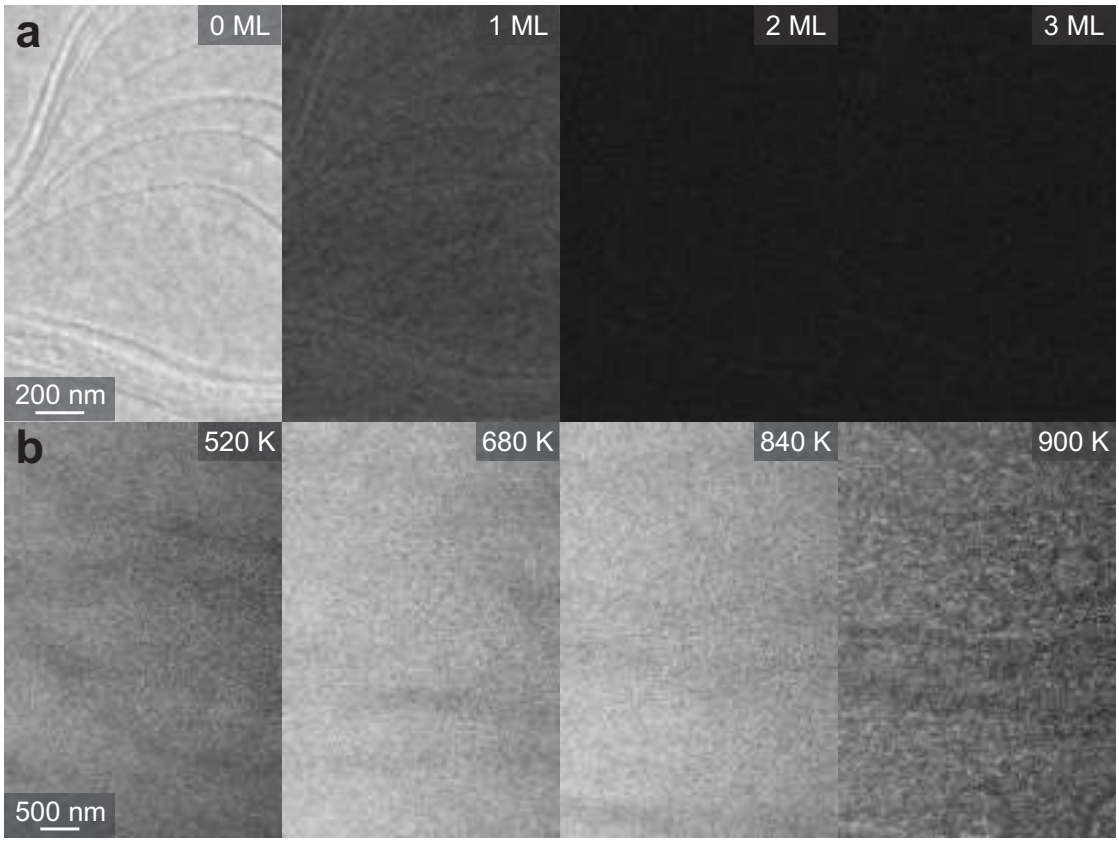

Figure 2.6: Formation of Fe_3O_4(111) thin film. (a) Fe deposition on FeO/Pt(111) at 300 K. E_0 = 20 eV. (b) Oxidation (p = 1x10^{-6} mbar) of 8 ML of Fe deposited on FeO/Pt(111). The surface reflectivity increases with the temperature and the contrast is recovered for temperature above 840 K. E_0 = 20 eV.

2.1.2 Two kinds of surface termination

The $Fe_3O_4(111)$ surface is known[31] to have at least two kind of atomic termination, that are formed at different oxidation temperature. For a better understanding, let us start from the basic description of the unit cell, following the syntax presented in Ref. 32. The magnetite crystal has a cubic inverse spinel structure that exhibits homonuclear layers along the (111) planes. The structure can be represented by the stacking sequence $Ba_3Ca_1b_1c_1Ac_3Bc_1a_1b_1C$, where each letter corresponds to a plane, each subscript number describes how many atoms are in the plane and the upper-case represents the oxygen layers. The unit cell, defined by the [111] axis (z) together with those axes (x,y) defining the (2x2) structure, contains 8 oxygen atoms and 6 iron atoms, organized in 4 layers. Two close-packed oxygen layers (four atoms each) stacked in fcc sequence ABCABC are separated by two different iron layers, which alternate in the stacking order. In the first one, called Kagomé , three $Fe^{2+,3+}$ atoms populate three quarter of the available octahedrally coordinated sites, situated within a single (111) plane. The second one, called MixTrigonal, presents two Fe^{3+} atoms tetrahedrally coordinated and one $Fe^{2+,3+}$ octahedrally coordinated per unit cell; each one has a different z coordinate. With this configuration one of the four oxygen atoms of the unit cell differs from the other, it presents three bonds toward the Kagomé iron plane and one to the MixTrigonal, while the others present two bonds to each plane. This induces a slight difference in the position along the z coordinate. For $Fe_3O_4(111)$ a ML is represented by the surface density of a close-packed layer of oxygen. The O-O distance on the (111) plane is 2.97 Å, while the distance between oxygen planes in the z direction is 2.35 Å when a Kagomé layer is included, and 2.50 Å when a MixTrigonal layer is included. The unit cell height along the [111] direction is therefore 4.85 Å, which corresponds also to the typical step height for this orientation[33]. The complete unit cell model is shown in **Fig. 2.7a** as a side view, while top view of the two iron layers is presented in **Fig. 2.7b**.

The surface termination obtained by the described preparation procedure (final oxidation at 1000 K) can be represented by rigid truncation of the bulk crystal unit cell along the MixTrigonal plane, in a way that only the bottommost iron atom remains. The $Fe_3O_4(111)$ surface exposes therefore ML of Fe with tetrahedric coordination on a close-packed oxygen layer. Under this, a Kagomé iron layer is arranged. This model

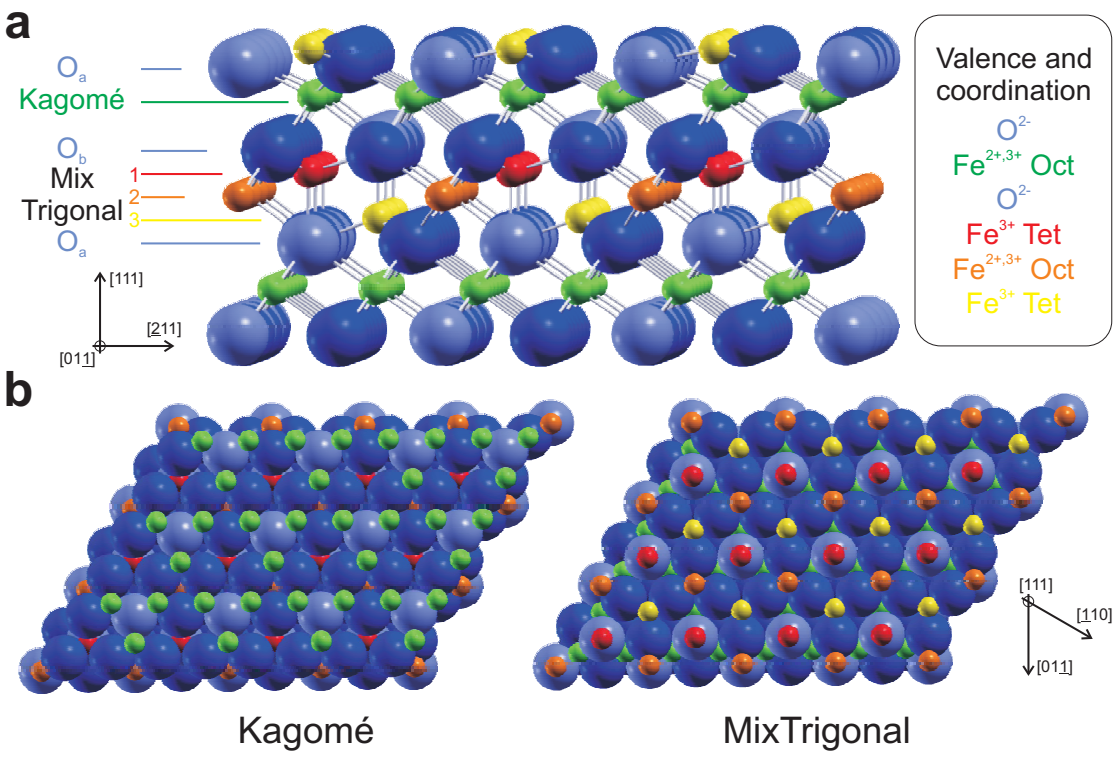

Figure 2.7: (a) side view and (b) top view of the Fe_3O_4 lattice structure. The oxygen atoms are presented with two shades of blue to highlight their bond orientation. Dark blue oxygen atoms are bonded with two iron atoms per iron plane; light blue oxygen atoms are bonded with three iron atoms in the Kagomé layer and one iron atom in the MixTrigonal. This different configuration influences their position inside the lattice: the light blue atom is 0.04 Å closer to the Kagomé layer respect to the dark blue ones.

is generally accepted in literature as the most common one for these preparation conditions, and is confirmed by several dynamic LEED and STM analysis[32,33] (**Fig. 2.8a**). The LEED pattern is formed by sharp spots arranged in a hexagonal pattern (**Fig. 2.8b**). The reciprocal lattice vectors (1;0) and (0;1) are usually defined from the real space vectors that identify the position of the oxygen, instead of those that define the inverse spinel unit cell (which has twice the length). In this way the spots labeled as (1;0) and (0;1) are close to the first order ones of the Pt(111) substrate. With this definition the Fe_3O_4(111) LEED pattern appears as a (2x2) superstructure, with half-order diffraction spots produced by the twice as large unit cell.

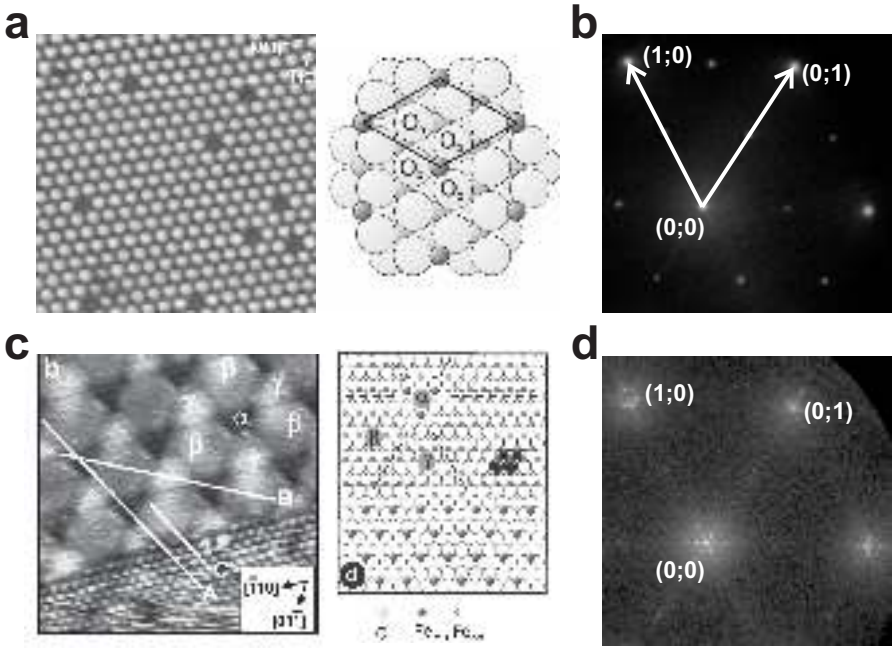

Figure 2.8: Atomic view and LEED pattern of the different termination of $Fe_3O_4(111)$ surface. (a) STM image and scheme of the termination produced with an oxidation temperature of 1000 K. The protrusions in the STM image correspond to the iron atoms that rest upon a closed oxygen layer. From Ref. 33. (b) Corresponding LEED pattern, E_0 = 38 eV. (c) STM image and scheme of the termination produced with an oxidation temperature of 870 K, the so-called biphase. From Ref. 36. (d) Corresponding LEED patter, E_0 = 58 eV.

At a slightly lower oxidation temperature, around 870 K, the magnetite (111) surface presents a more complex atomic termination, called biphase ordering, for the first time by Thornton's group[46] on α-Fe2O3(0001) in 1995 and on $Fe_3O_4(111)$ single crystal in 1997[35]. In 1999[36] Shaikhutdinov *et al.* confirmed that this termination exists also for $Fe_3O_4(111)$ thin films on Pt(111). This STM investigations showed the coexistence of the termination described in the paragraph above and areas with a superstructure with a periodicity between 40 and 60 Å, aligned to the regular $Fe_3O_4(111)$ lattice (**Fig 2.8c**). In this superstructure three regions can be distinguished in STM; two with triangular shape and specular orientation (β and γ), and a third, smaller and located at the vertexes of the other two (α). The model proposed for these areas presents three different atomic termination: while for α the termination appears like the normal one in $Fe_3O_4(111)$, β and γ expose respectively 3/4 ML and a close-packed layer of octahedrally coordi-

nated Fe atoms located over an oxygen layer. The superstructure region is located 2.5 Å lower than the regular $Fe_3O_4(111)$ surface, with a further depression detected only in the α region. From this one might conclude that the β region corresponds to a rigid truncation of the unit cell along the Kagomé iron layer, while the γ is a Kagomé modified with add 1/4 ML of Fe, i.e. the surface atoms are arranged with a FeO(111)-like compressed structure (the mismatch between FeO(111) and $Fe_3O_4(111)$ oxygen planes is 3%). The only two LEED pattern available in literature for the biphase[35,47] are taken at $Fe_3O_4(111)$ single crystals and present satellites corresponding to the superstructure only around the first order diffraction spots; the quality of the image, however, is very poor. In order to establish more precisely the LEED pattern of the biphase surface termination, a $Fe_3O_4(111)$ thin film was produced with lower oxidation temperature, 850 K. The result is depicted in **Fig. 2.8d**. Satellites with hexagonal symmetry surround every diffraction spots. The half-order spots of biphase termination were weaker in intensity than the corresponding ones for the 1/4 ML Fe termination, and presented satellites as well. A SPA-LEED analysis of the satellite position showed that they were produced by a 2D superstructure with a spatial periodicity of 53 Å, in good agreement with the previous findings.

2.2 Changes in the preparation conditions and inhomogeneities

The $Fe_3O_4(111)$ film prepared with the procedure described above consists of terraces up to 100 nm wide. By looking at the surface in LEEM, the step density increased after every cycle, especially above 20 nm of thickness. The film could be smoothed if the temperature of the last oxidation treatment was increased to about 1000 K, whereas it was necessary that the film was already closed and thicker than 7 nm. For thinner films the annealing up to 1000 K led to an irreversible de-wetting (see Section 2.2.2). The LEED pattern of the film matched perfectly the one referred to the first atomic termination, i.e. 1/4 ML of iron atoms over a close-packed oxygen layer. A subsequent thermal flash in UHV did not produce further morphological changes.

After having experience with the canonical recipe, several films have been produced

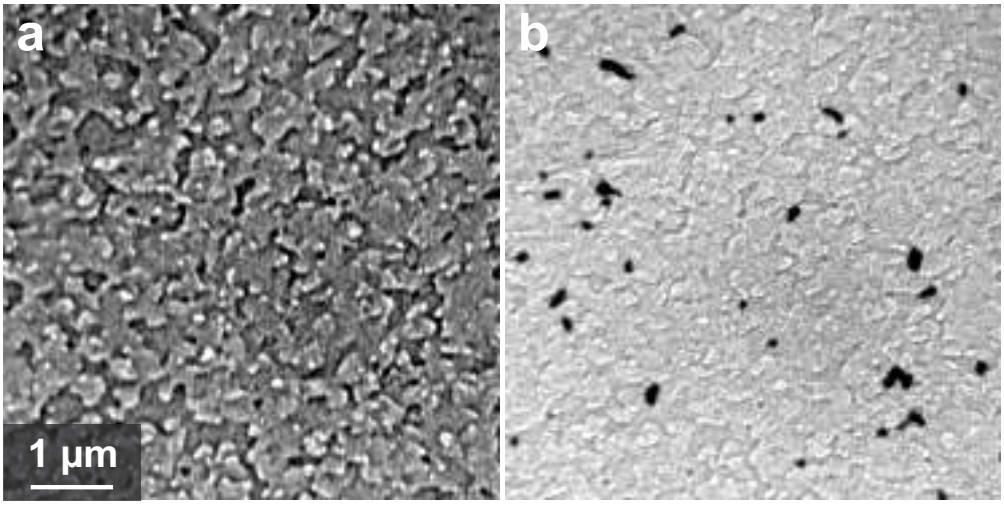

Figure 2.9: (a) Wide-range bright field and (b) dark field LEEM images of the identical surface area using the (0;0) and (1/2;0) spots, respectively. The contrast is due to the film morphology. Additionally, the domains rotated by 180° become visible as dark areas in the dark field image. Image (a) is in slight overfocus. E_0 = 24 eV.

with slightly different preparation conditions, from which a large case record has been collected, mainly focused on the inhomogeneities in the thin film. These can be of different nature: crystallographic, morphological and regarding the surface termination.

2.2.1 Crystallographic inhomogeneities

Magnetite crystallizes in an inverse spinel structure with space group $Fd3m$, while the Pt substrate exhibits a fcc structure with space group $Fm3m$. Therefore, during the thin film formation on clean Pt(111), the Fe_3O_4 islands created by initial nucleation can only coalesce with improper stacking and form a complete film with two twin domains rotated by 180°. Dark field LEEM studies using the (1/2;0) and (0;1/2) spots showed an unexpected distribution of the rotational domains. For every film completely covering the metal surface we prepared, a predominance of one rotational domain was observed. Depending on the preparation conditions, the coverage ratio for the rotational domains ranged between 75%/25% and 98%/2%. **Fig. 2.9a** and **b** show bright field and dark field LEEM image of a closed Fe_3O_4(111) film, respectively. In the dark field the two rotational domains are visualized as dominating bright area and small black areas. This

preponderance is maintained even after subsequent cycles of Fe deposition and oxidation. On average, the rotational domain size is larger than the terrace width; some of them were even several microns wide. A comparison between dark field and bright field LEEM images shows that the rotational domains are preferentially placed in correspondence of the step bunches of the substrate. This can be checked by using electrons with very low kinetic energy: in this case the mean-free-path length is so large that LEEM can image through the oxide film. **Fig. 2.10** shows that at substrate step bunches (identified in bright field with the horizontal stripes which looks like in relief) the Fe_3O_4 film consists mainly of the rotational domain that corresponds to the minority species on the substrate terraces. The possible origin of this inhomogeneity will be discussed in more details in Section 3.2, where further elements will be introduced.

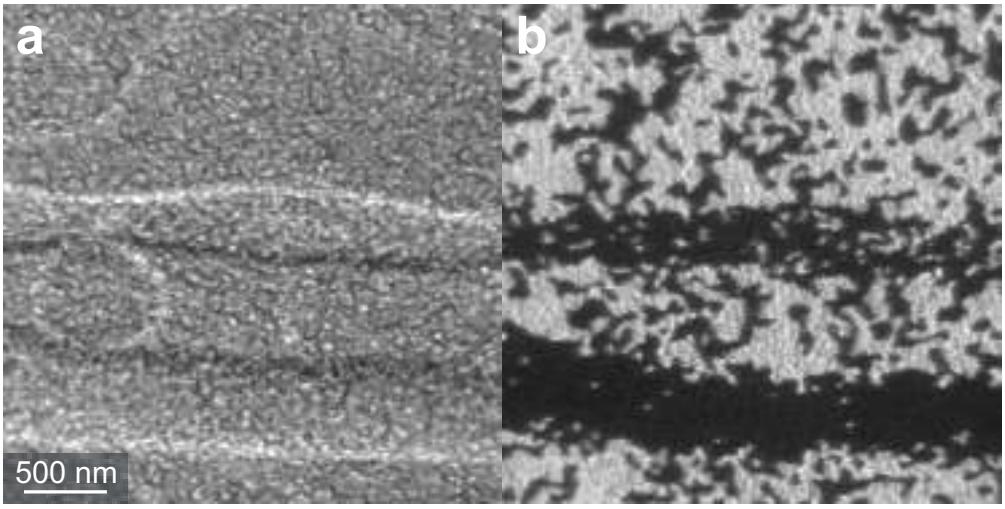

Figure 2.10: Rotational domains at the substrate step bunches. (a) Bright and (b) dark field LEEM images of a closed Fe_3O_4 layer. The thin film crystallized on the substrate step bunches (visible in bright field as the two horizontal stripes that look like in relief) present a different ratio in the relative abundance of the rotational domains. E_0 = 24 eV.

2.2.2 Morphological inhomogeneities

A crucial parameter for the morphological uniformity of the thin film is the oxidation temperature. On the one hand it should be high enough to enable the oxidation process,

but on the other hand not too high, especially during the first deposition cycles, to avoid a de-wetting of the Fe_3O_4 film. The latter was observed at oxidation temperatures above 900 K, as FeO areas became clearly visible in the "holes" of the $Fe_3O_4(111)$ film. The width of these FeO domains increased dramatically at further increase of temperature, from approximately 100 nm to about one micron for an oxidation temperature of 1000 K. The FeO areas could be identified by various experiments: bright field and dark field LEEM, LEED and XPEEM. In the de-wetted case bright field LEEM images (**Fig. 2.11a**) Fe_3O_4 (dark) and FeO (white) areas are visible with different contrast, while the corresponding LEED pattern shows the superposition of the $Fe_3O_4(111)$ patter and the Moiré pattern of FeO(111)/Pt(111). By dark field imaging using the Fe_3O_4 (1/2;0) and (0;1/2) spots (**Fig. 2.11b** and **c**), isolated with the smallest contrast aperture (10 μm), the FeO areas appear dark, while the Fe_3O_4 areas shows the contrast between rotational domains. On the contrary, the FeO domains can be unambiguously identified as brighter areas if one of the satellite spots around (0;0) is selected (**Fig. 2.11d**). XPEEM images obtained with Pt $4f_{7/2}$ core level emission line (**Fig. 2.11e**) additionally reveal that the FeO domains formed by de-wetting are indeed deep holes in the Fe_3O_4 film. The FeO areas are so thin that the electrons photo-emitted by the Pt substrate can still pass through, while the magnetite film is thick enough to damp completely the Pt signal. Considering the electron mean free path at the used kinetic energy (104.2 eV) one can estimate the thickness of the FeO areas as a few angstrom. Once the Fe_3O_4 film had de-wetted and FeO holes were formed, it was nearly impossible to recover a closed Fe_3O_4 film by several additional cycles of Fe deposition and oxidation. Obviously, the Fe atoms adsorbed on the FeO areas at room temperature migrated onto the Fe_3O_4 areas during the oxidation process at 900 K. Consequently, only the Fe_3O_4 grew, while the FeO zones remained present. Furthermore, wide-range LEEM images of an almost closed Fe_3O_4 film show that FeO domains are formed preferentially at the step bunches of the Pt(111) substrate (**Fig. 2.11f**), where the Fe_3O_4 is in stable, most likely due to the strain induced by the steps and the step bunches.

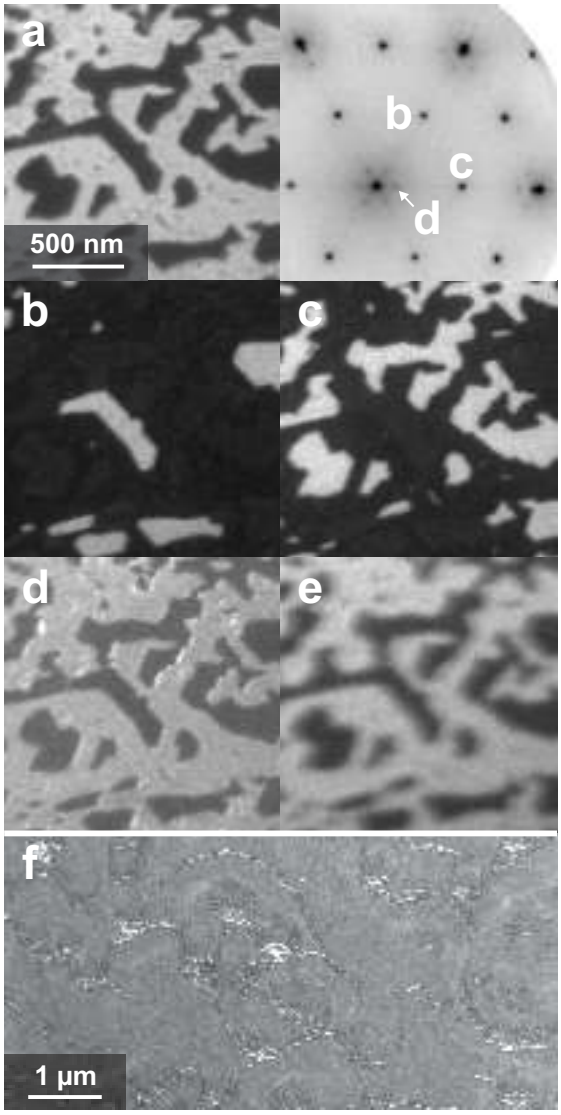

Figure 2.11: Strongly de-wetted Fe_3O_4 film analyzed by microscopy, diffraction and local spectroscopy. (a) Bright field LEEM image (E_0 = 24 eV) and relative LEED pattern (E_0 = 88 eV) showing Fe_3O_4 and FeO structures. The labels in LEED mark the selected diffraction spots used for the dark field LEEM images (b), (c) and (d). In (d) facets appear as white lines due to the particular diffraction conditions. (e) XPEEM image of the Pt $4f_{7/2}$ photoemission line, hν = 180 eV, E_B = 71.6 eV. (f) Wide-range bright field LEEM image of a different and almost complete Fe_3O_4 thin film (in gray) with small FeO domains (in white) formed upon the Pt(111) step bunches (the wavy structures still visible in dark gray). E_0 = 21 eV.

2.2.3 Surface inhomogeneities

Beside the two inhomogeneities in the rotational domains and in the morphology discussed so far, it has been detected a third type related to the surface termination. This phenomenon was investigated using four comprehensive methods: (a) SPA-LEED studying the profile of the LEED spots in real-time yielding the domain sizes for different preparations, (b) XPS of the surface before and after the final annealing, determining the chemical composition of the surface, (c) STM of the "as prepared" surface, visualizing objects smaller than the LEEM resolution and (d) dynamical LEED analysis of the spot intensities for differently prepared surfaces, studying the surface unit cell structure and therefore the termination.

SPA-LEED

The "as prepared", fully closed film oxidized at 1000 K exhibits a shoulder-like broadening around the (0;0) peak (**Fig. 2.12a**), which gradually disappeared upon a thermal flash to 900 K in UHV. The profile of the specular diffraction spot has been fitted with a superposition of a central peak with a Gaussian-like instrumental broadening, and a shoulder which can be described as a sum of three Lorentz$_{3/2}$-like functions of different half-widths. Given the scattering vettor $\mathbf{k}$ as the difference between the final (after reflection) and initial electron wave vector, $\mathbf{k} = \mathbf{k}_f - \mathbf{k}_i$, and depicted its parallel and perpendicular components respect to the surface, $\mathbf{k}_\parallel$ and $k_\perp$, one has that

$$I_{(00)}(\mathbf{k}_\parallel, k_\perp) = I_{central}(\mathbf{k}_\parallel, k_\perp) + I_{shoulder}(\mathbf{k}_\parallel, k_\perp) \tag{2.1}$$

with

$$I_{central}(\mathbf{k}_\parallel, k_\perp) = I_{Gauss}(k_\perp)\, f_{Gauss}(\mathbf{k}_\parallel) \tag{2.2}$$

$$I_{shoulder}(\mathbf{k}_\parallel, k_\perp) = I^{(1)}_{Lor3/2}(\mathbf{k}_\parallel, k_\perp) + I^{(2)}_{Lor3/2}(\mathbf{k}_\parallel, k_\perp) + I^{(3)}_{Lor3/2}(\mathbf{k}_\parallel, k_\perp) \tag{2.3}$$

The prominent broadening as shown in **Fig. 2.12b** is described by the first part $I^{(1)}_{Lor3/2}$. The weakly modulated background, described by the broadened Lorentzian$_{3/2}$ $I^{(2)}_{Lor3/2}$

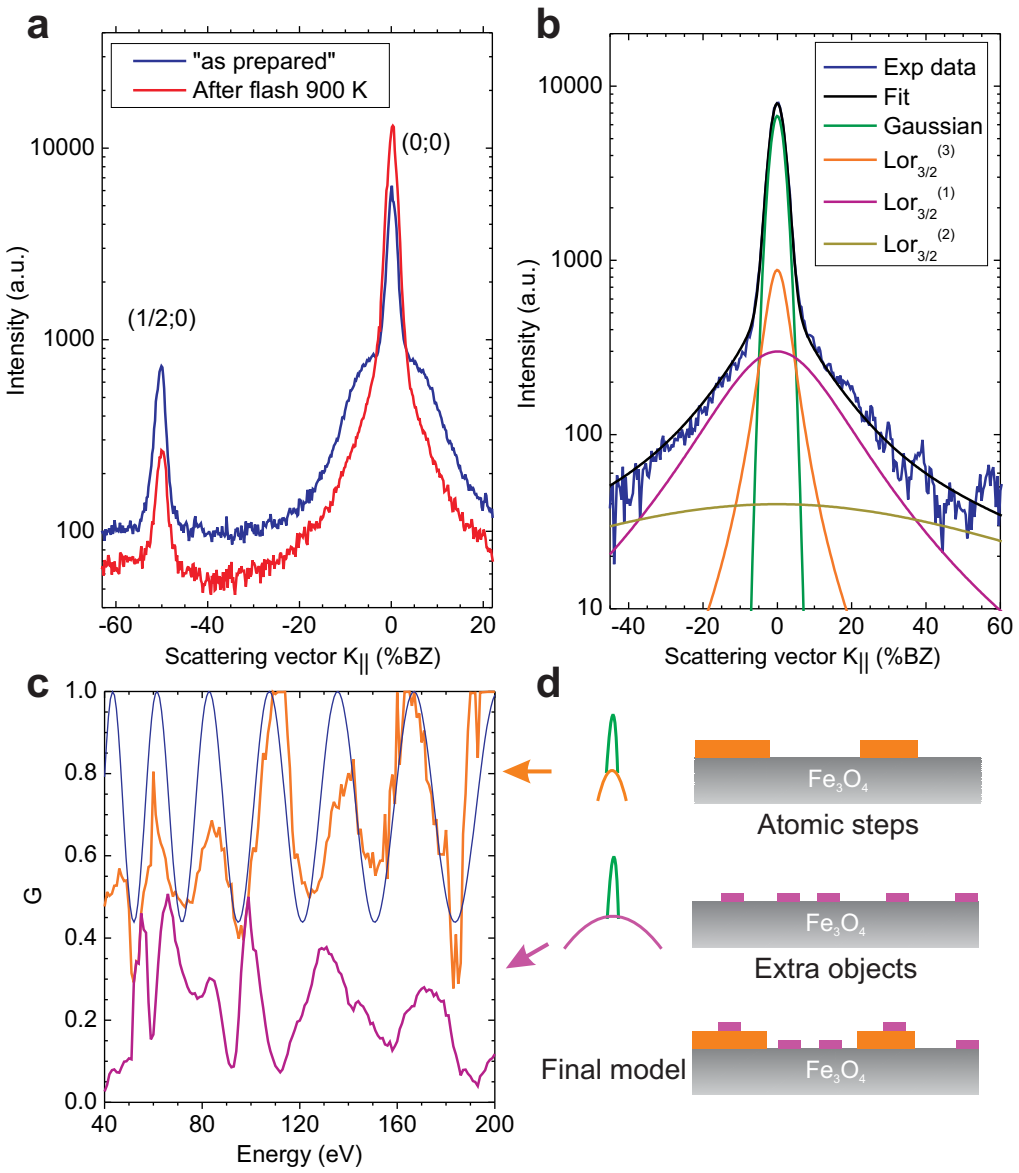

Figure 2.12: (a) Spot profile analysis of the LEED pattern for the "as prepared" surface (in blue) and after a final annealing at 900 K (in red). (b) Fit of the LEED profile with a narrow Gaussian for the central peak in green, two Lorentz$_{3/2}$ peaks in orange and purple for the shoulder-like broadening and a very broaden Lorentz$_{3/2}$ peak in dark yellow for the background. (c) Graph of the relative intensities G for the orange and purple peaks in function of the energy. The fit for the orange curve with $G(S)$ is shown in light blue. (d) Scheme for the surface model proposed.

with a full width at half maximum (FWHM) as large as the Brillouin Zone, can be related to adsorbates or small clusters on the surface[36]. The third Lorentzian$_{3/2}$ $I^{(3)}_{Lor3/2}$ has a FWHM slightly larger than the Gaussian one and can be related to the presence of atomic steps. The (0;0) spot profiles have been analyzed in the energy range between 40 and 200 eV. The FWHM for both, the central peak and the prominent broadening, increases linearly with $k_\perp$; from this behavior a mosaic spread of $\pm$ 0.2° in the Fe_3O_4 film can be calculated, which is much larger than in the Pt substrate (0.007°) determined in the same way. The formation of a mosaic texture is well known for oxide films on metal systems: it has been reported not only for Fe_3O_4(111)/Pt(111)[48], but also e.g. for NiO(100)/Ni(100)[49] and NiO and MgO on Ag(100)[50]. The mosaic spread was produced during the film preparation and can be caused by small angle grain boundaries, which might be a compensation mechanism for the lattice misfit between the oxide film and the Pt substrate underneath.

The ratio G between the integral intensities of the I_{Gauss} and $I^{(3)}_{Lor3/2}$ LEED spot components

$$G = \frac{I_{Gauss}}{(I_{Gauss} + I^{(3)}_{Lor3/2}} \tag{2.4}$$

reveals a periodic exchange between two relative intensities (**Fig. 2.12c**). G can be modeled by a two-layer system described as

$$G(S,\theta) = 1 - 2\theta(1-\theta)(1-\cos(2\pi S)) \tag{2.5}$$

where θ is the coverage and $S = k_\perp/2\pi d$ the scattering phase, with d being the step height[51]. The fit gives the coverage equal to θ = 0.17 ML and a step height value d = 4.79 $\pm$ 0.09 Å , fully comparable with the height of the magnetite unit cell (4.85 Å). On the other hand, $G(S,\theta)$ calculated between the Gaussian and the broad $I^{(1)}_{Lor3/2}$ shows no periodicity in $k_\perp$, which is an indication of the presence of objects with a different form factor. From the FWHM, it has been calculated that the objects that generate the predominant broadening have an average lateral size of about 2 nm. **Fig. 2.12d** shows a schematic view of the proposed surface model, which assumes that the distribution

of the "atomic steps" causing the third Lorentzian$_{3/2}$ $I^{(3)}_{Lor3/2}$ is not correlated to the distribution of the "extra objects" related to the first Lorentzian$_{3/2}$ $I^{(1)}_{Lor3/2}$.

LEED profile analysis of the (0;0) spot has been performed also during the final oxidation and during the subsequent flash at 900 K, to detect the formation, the changes and the disappearance of the shoulder components. It was found that $I^{(1)}_{Lor3/2}$ was not present during the oxidation process when the temperature was still at 1000 K, but it formed during the cooling down at temperature below 750 K. This transient point changed with the cooling rate. **Fig. 2.13a** displays the integral intensities of the sharp central Gaussian and the $I^{(1)}_{Lor3/2}$ components for two different cooling rates, the faster passing from 1000 to 500 K in 120 s (i.e. approx. 4 K/s dark lines in the graph) and the slower in 460 s (i.e. approx 1 K/s light lines). For slow cooling rates the transient occurs even below 670 K. The final shape of the (0;0) spot appeared slightly different for the two cooling rates: the width of the $I^{(1)}_{Lor3/2}$ component decreased from 21% of the BZ for the fast cooling to 10% for the slow cooling, meaning twice as large objects when the sample spent more time at lower temperature with O_2 exposure. Furthermore, the spot profile has been measured when the oxygen exposure has been cut off during the cooling process above 750 K. In this case no broad component $I^{(1)}_{Lor3/2}$ was detected. Therefore, the formation of extra objects on the surface must be directly related to the O_2 exposure at lower temperature.

Fig. 2.13b shows the intensity behavior during annealing up to 900 K with an average heating rate of 3 K/s. The two oxide films studied have been produced with the fast and slow cooling of **Fig. 2.13a**. The temperature dependence of SPA-LEED during the annealing shows that the objects start to disappear for temperatures above 700 K for the first cooling and the objects created with slower cooling rate during the oxidation disappear not below 870 K. **Fig. 2.13c** and **d** display typical LEEM images for the "as prepared" surface created with slow cooling rate, before and after the annealing respectively. The "as prepared" surface appears very irregular, but well ordered after the flash with terraces of the Fe_3O_4 film a few 100 nm wide. The roughness of the "as prepared" film is due to the oxidation process, which most likely produces dense extra objects smaller than the lateral resolution in the experiment (20 nm) and makes therefore the morphology (atomic steps) of the Fe_3O_4 layer invisible.

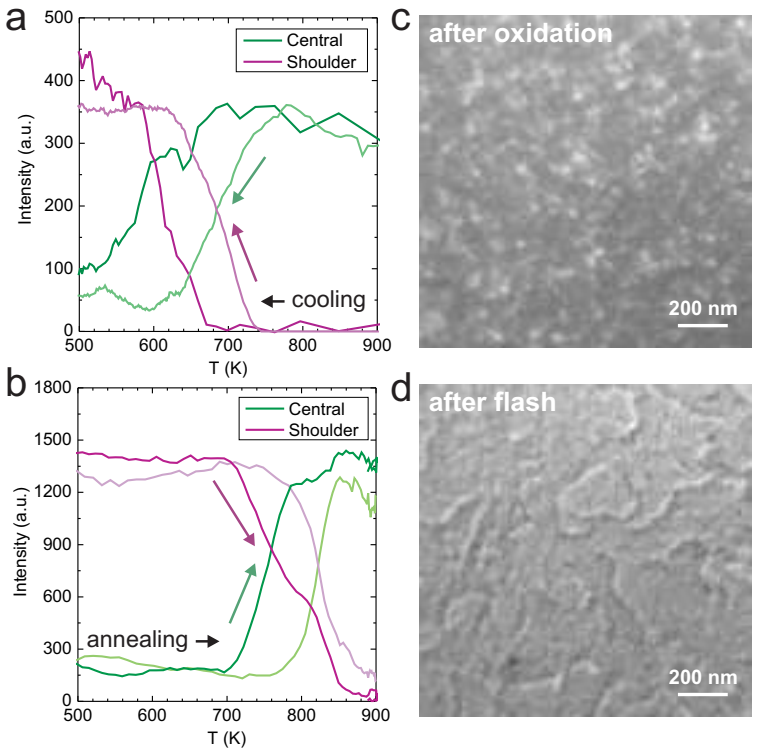

Figure 2.13: Formation of inhomogeneities during oxidation and annihilation by annealing. (a) Integral intensity of the central Gaussian and the shoulder Lorentz$_{3/2}$ components of the (0;0) LEED spot for fast (in dark) and slow (in light) cooling rate in oxidation atmosphere; E_0 = 39 eV. (b) Intensity of the same components during a flash in UHV at 900 K; E_0 = 39 eV. (c) and (d) LEEM images of the "as prepared" magnetite thin film after the oxidation with slow cooling rate and of the surface after the flash, E_0 = 24 eV, slight overfocus.

XPEEM/XPS

Based on the results from SPA-LEED measurements, XPEEM images were taken to check whether the surface inhomogeneity was related to possible contamination originating from the background pressure (carbon- and nitrogen-related gaseous species) or from possible migration of Mo from the cap that held the sample. From a stack of XPEEM images taken for a defined kinetic energy range, and with fixed photon energy, one can extrapolate the XPS spectra from a controlled and localized area of the sample. These spectra were measured both for the "as prepared" surface and after the flash at

900 K, with an energy resolution of 0.5 eV. In the spectra no C 1s, N 1s and Mo 3d core level photo-emission lines were detected. Both, the O 1s and the Fe 3p core level spectra (**Fig. 2.14**) change during the final flash, whereas the two spectra have been taken within a few minutes without any change of the beam-line parameters or of the microscope in between. A fit of the O 1s line with a single Voigt function reveals a small peak shift of 0.10 eV between the two spectra. Due to the limited energy resolution, it is not possible to verify whether the shift is caused by superposition of several components. However, it is a strong indication that the annealing changes the electronic properties of the surface. In XPEEM no image contrast and therefore no further details of the surface were detected. This means that there is no domain of chemical species larger than the lateral resolution in the XPEEM experiments (50 nm).

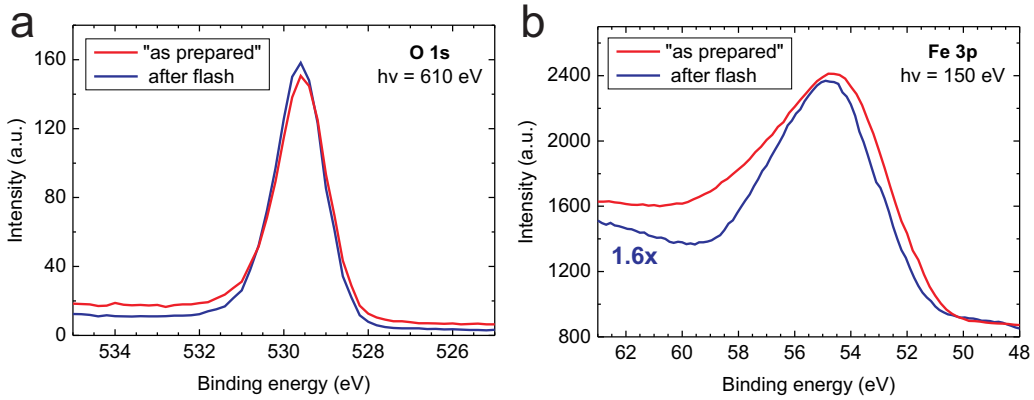

Figure 2.14: Influence of the final annealing on the extra oxygen driven species: O 1s (a) and Fe 3p (b) XPS spectra of the ”as prepared” Fe_3O_4(111) film and after a flash at 900 K.

STM

A confirmation of the changes in the surface structure detected with SPA-LEED and XPS was given by STM data collected by the Surface and Reactivity group at the Fritz-Haber-Institut, led by Shamil Shaikhutdinov, which had collected some STM images of the ”as prepared” Fe_3O_4(111) film on Pt(111) prepared with the same preparation

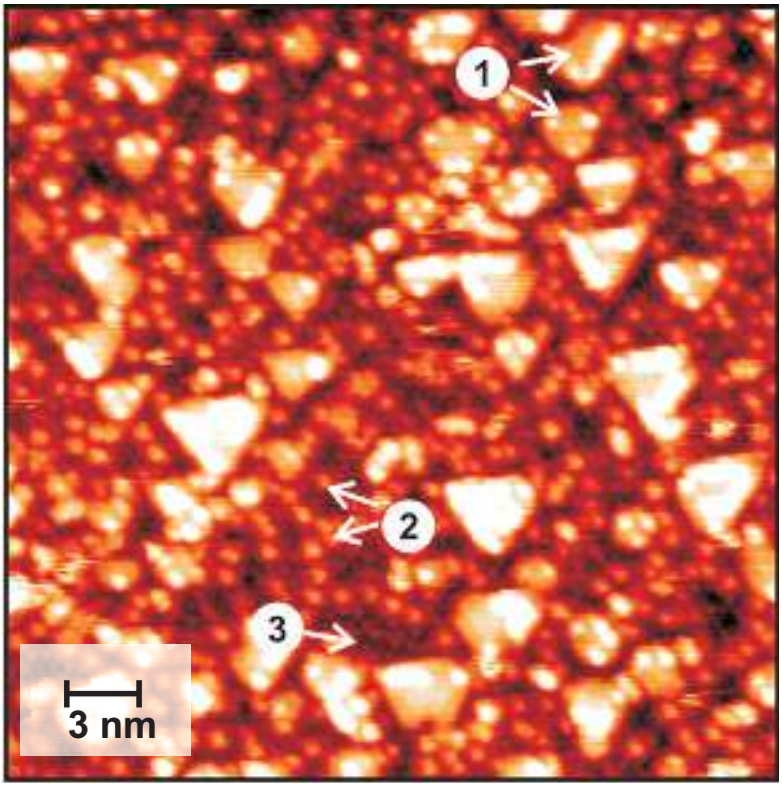

Figure 2.15: Typical STM image of an "as prepared" $Fe_3O_4(111)$ film. This film was oxidized in $2x10^{-6}$ mbar O_2 at 1000 K; at the subsequent cooling down the oxygen was reduced at 500 K. Several species are observed as indicated (see text). Tunneling bias 1.4 eV, current 1 nA. Courtesy from Zhi-Hui Qin and Shamil Shaikhutdinov.

recipe described above. An example of them can be seen in **Fig. 2.15**. In this figure several species can be clearly identified on the film surface: triangularly shaped islands (1), randomly distributed broad protrusions (2) located in registry to the ordered lattice of small protrusion with 6 Å periodicity (3). This periodic structure has been already reported in several STM studies of the $Fe_3O_4(111)$ surfaces (in form of both, single crystals and films) and assigned to the Fe atoms on the 1/4 ML Fe-terminated surface[35,36,39]. Species (2), which are about 1.5 Å in height, have previously been assigned to adsorbates (presumably, water related) as a result of the interaction of the Fe-terminated surface with the residual gases in UHV[52]. This species can explain the weakly modulated background $I^{(2)}_{Lor3/2}$ detected in SPA-LEED. The flat triangular islands (1) are about 2 nm in average size and about 2.5 Å in height, with edges running

along the main crystallographic directions of the $Fe_3O_4(111)$ surface, which implies a high degree of crystallinity of the islands. These can be attributed to the broad shoulders $I^{(1)}_{Lor3/2}$ detected in SPA-LEED. In fact, the average size of the triangular-shaped islands (2 nm) is fully compatible with the FWHM of the $I^{(1)}_{Lor3/2}$ component. The islands could not be atomically resolved in STM experiments indicating very low corrugation amplitude, which is anticipated for oxygen-terminated oxide surfaces where the topmost oxygen layer effectively screens electrostatic states of underlying metal cations, mainly contributing to the tunneling current[36]. This is not in contradiction with the SPA-LEED findings, which excludes also that these objects are simply small terraces that present the same atomic termination like the rest of the surface: if this would be the case, $G(S)$ should show a periodicity respect to S, which is in contrast to the experimental results of SPA-LEED.

I/V-LEED

The intensity modulation of different diffraction spots were extracted from LEED spectra of the Fe_3O_4 film, taken with SMART as a function of the beam kinetic energy. This measurement has been done at room temperature for both, the "as prepared" surface and after the flash at 900 K. In particular, the intensity of six different diffraction spots, (0;0), (1/2;0), (0;1/2), (1;0), (0;1) and (1/2;1/2), has been analyzed within an energy range between 40 and 300 eV, corresponding to an overall dataset of 1560 eV. The spectra of each spot have been extracted from recorded LEED pattern via numerical integration over an area large enough to incorporate the signal from the broadening found in SPA-LEED. The advantages of LEEM systems such as SMART in collecting these spectra compared to a standard LEED optics are various. During the energy scan the operation condition of the electron gun and the image columns are not altered, but solely the sample potential is changed. Consequently the beam current on the sample is constant during the scan, for all experiments. Additionally, due to the optics the investigated diffraction spots do not move in position on the detector during the energy scan and the (0;0) spot is visible even at full perpendicular illumination. It is also possible to directly inspect the probed surface region from where the diffracted electrons are collected. Combining this with a dark field image, which gives the portions of the possible rotational domains, one can easily decouple the contributions of the two rota-

tional domains and extract the real spectra of (1/2;0), (0;1/2), (1;0) and (0;1) spots of a single rotational domain. This is not possible with a standard back-view LEED setup, because of the superposition of two threefold pattern with unknown relative abundance. Therefore, one is forced to average the spectra of spots of the same diffraction order, with consequent loss of information.

In our case, the ratio of the surface areas arranged with the two rotational domains was 94%/6%; giving a correction factor p = 0.06 and assuming that the experimental LEED pattern is a weighted incoherent superposition of two rotated LEED patterns:

$$I_{total}(\mathbf{k}_{\parallel}, k_{\perp}) = (1-p)\, I_{+}(\mathbf{k}_{\parallel}, k_{\perp}) + p\, I_{-}(\mathbf{k}_{\parallel}, k_{\perp}) \tag{2.6}$$

with the intensity of the two rotational domains $I_{+}(\mathbf{k}_{\parallel}, k_{\perp})$ and $I_{-}(\mathbf{k}_{\parallel}, k_{\perp})$, and with the probability of (1-p) and p, respectively. Because of the 180° rotation symmetry between the domains:

$$I_{+}(\mathbf{k}_{\parallel}, k_{\perp}) = I_{-}(-\mathbf{k}_{\parallel}, k_{\perp}) \tag{2.7}$$

As a consequence one may separate the two contributions as:

$$I_{+}(\mathbf{k}_{\parallel}, k_{\perp}) = \frac{1-p}{1-2p} I_{total}(\mathbf{k}_{\parallel}, k_{\perp}) - \frac{p}{1-2p} I_{total}(-\mathbf{k}_{\parallel}, k_{\perp}) \tag{2.8}$$

The resulting disentangled I/V-LEED spectra for the ”as prepared” and ”after flash” surface are shown in **Fig. 2.16** and differ strongly in some energy ranges; the most evident changes are marked by arrows in the figure. This can be interpreted as a change in the surface termination. Additionally, we found that the spectra of the ”as prepared” surface do not change significantly for different cooling rates.

The fitting strategy of the I/V spectra was structured in two steps. The first one determined the surface structure of the flashed film under the assumption of its structural homogeneity. Once being obtained, this structure was used as a support on top of which small islands, observed by SPA-LEED and STM, were modeled in order to fit the I/V data obtained for ”as prepared” samples. The code used is the Barbieri/Van-

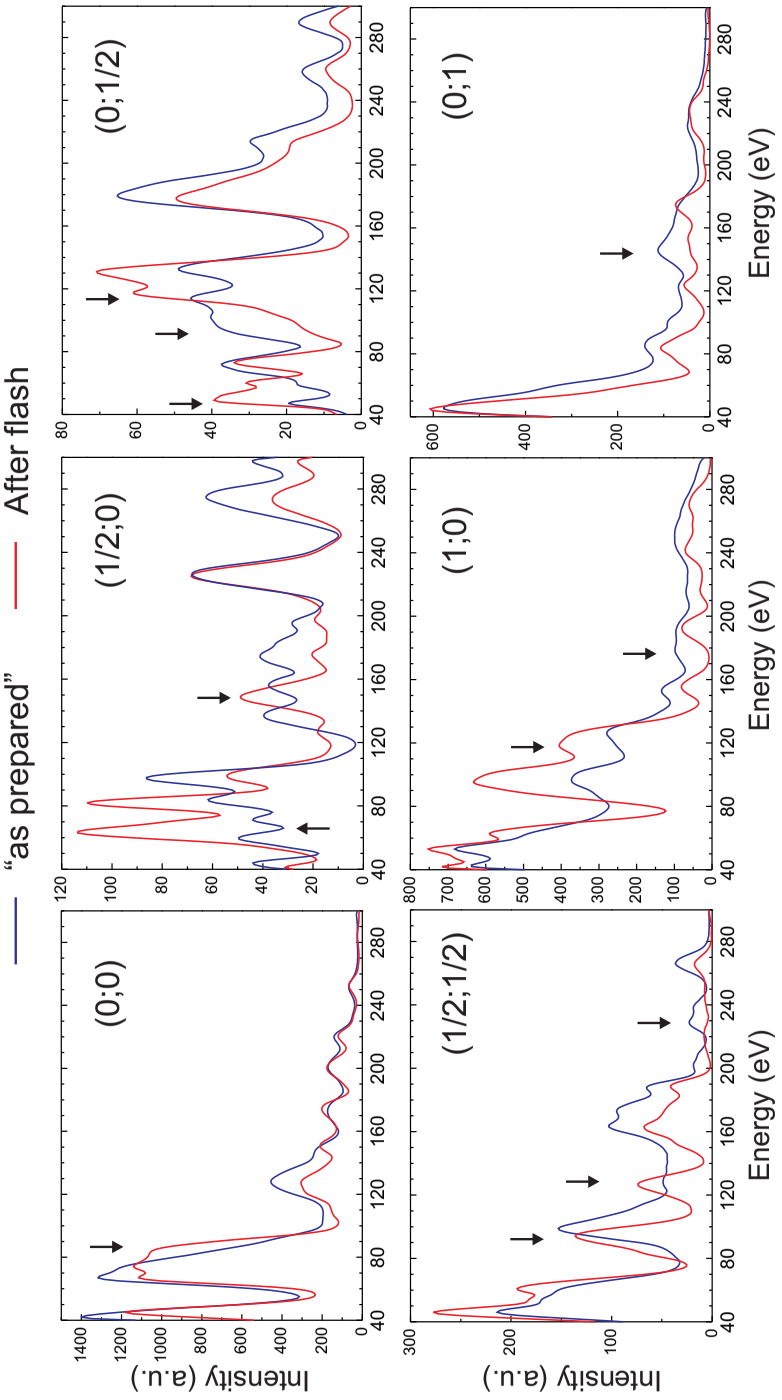

Figure 2.16: I/V-LEED curves of the first six diffraction spots, for the "as prepared" surface and after the annealing at 900 K. The curves were smoothed via convolution with a Lorentzian function of width equal to 2 eV[53]. The arrows mark the major changes produced by the flash.

Hove SATLEED for the generation and the fitting of I/V spectra and for the phase shifts calculation. A detailed computational description of these packages can be found in Van Hove's homepage[54]. The initial configuration of the system has been extracted by the final parameters and position of atoms in the unit cell of Ritter and Weiss[33]. The scattering phase shifts were calculated for oxygen and iron atoms in Fe_3O_4 structure up to a maximal azimuthal quantum number of $l = 7$, assuming a muffin-tin radius of 0.96 Å for O and 0.92 Å for Fe[55]; For the calculation a Debye temperature of 280 K for Fe and 550 K for O were set, and an imaginary part of the inner potential of 5 eV was chosen.

The assumed models for the surface atomic structure was obtained firstly by truncation of the bulk crystal unit cell along the (111) plane, which yields six different terminations. Additionally, it has been taken into account the possibility that in proximity of the surface one iron atom can go underneath the first close-packed oxygen layer, which is suggested as the more energetically favored atomic termination by DFT calculations from Zhu *et al.*[56]. Other more complex structure models were taken into account, i.e. with incomplete site occupation and/or changed coordination sites and shifted planes. The experimental I/V curves were smoothed via convolution with a Lorentzian of width equal to 2 eV[53]. Each configuration was optimized until the change in every atomic coordinate in a single iteration loop was below 0.1 Å. **Table 2.1a** shows the resulting Pendry Reliability (R) factors of the relaxed best models. The most reliable model is ML Fe atom belonging to the MixTrigonal layer on a close-packed oxygen layer resting upon a Kagomé iron layer. This configuration is displayed in **Fig. 2.7a**. Summarizing, this analysis confirms the expected atomic surface termination for the optimial preparation condition, i.e. oxidation of Fe and a subsequent final flash in UHV.

The fit of the I/V curves measured for the "as prepared" films gives the results shown in **Table 2.1b**: in general, all R-Factors are much larger with respect to the values obtained with the flashed surface. The most reliable model was still the one described above, but with an R-Factor of 0.33, much worse than before. Assuming that, as shown in the STM images, part of the "as prepared" surface exposes the termination dominant after the annealing, one can try to subtract the contribution. The restriction that the resulting I/V spectra must be greater than zero limits the value of the effective coverage of this termination to θ_{eff} = 0.25 ML. Therefore, one may describe the "before flash"

Models	R-Factors		
	a	**b**	**c**
$a_1Ba_3Ca_1b_1c_1A...$	0.14	0.33	0.50
$Ba_3Ca_1b_1c_1A...$	0.23	0.45	0.47
$Ca_1b_1c_1A...$	0.53	0.42	0.56
$c_1a_1Ba_3Ca_1b_1c_1A...$	0.35	0.48	0.56
$b_1c_1a_1Ba_3Ca_1b_1c_1A...$	0.49	0.50	0.54
$a_3Ca_1b_1c_1A...$	0.55	0.52	0.65
$c_1Ba_3Ca_1b_1c_1A...$	0.37	0.46	0.51
$a_4Ba_3Ca_1b_1c_1A...$	0.41	0.44	0.53
$Aa_4Ba_3Ca_1b_1c_1A...$	0.73	0.70	1.00
$Ba_4Ca_1b_1c_1A...$	0.32	0.44	0.59
$a_1B_3a_3Ca_1b_1c_1A...$	0.35	0.40	0.54
$C_3a_1b_1c_1A...$	0.58	0.57	0.56

Table 2.1: R-factors of the I/V-LEED analysis for different models of surface termination in case of (a) $Fe_3O_4(111)$ surface after a flash at 900 K, (b) $Fe_3O_4(111)$ surface "as prepared" and (c) $Fe_3O_4(111)$ surface "as prepared" with a partial subtraction of the spectra obtained after the flash. The models syntax corresponds to Ref. 32.

I/V spectra as a superposition of the intensity after the flash and intensity I_{inh} of the unknown species, i.e.

$$I_{before\ flash}(V) = \theta_{eff} I_{inh}(V) + (1 - \theta_{eff}) I_{after\ flash}(V) \tag{2.9}$$

With this, a new set of spectra of the inhomogeneity $I_{inh}(V)$ has been created

$$I_{inh}(V) = \frac{1}{\theta_{eff}} I_{before\ flash}(V) - \frac{1 - \theta_{eff}}{\theta_{eff}} I_{after\ flash}(V) \tag{2.10}$$

This new set, that represents the I/V spectra of the surface subtracted by the contribution of the non-covered surface fraction, was now used for the I/V-LEED simulations. The results are shown for θ_{eff} = 0.25 ML in **Table 2.1c**. The R-factor of the "flashed surface" configuration (top line) rises up to 0.50, while the other models showed no improvement. Also for other θ_{eff} values we never found an improvement compared to the column in **Table 2.1b**. Therefore, we have to clearly state that all suggested terminations in **Table 2.1** for the as prepared surface are not reliable.

2.2.4 Discussion

The comprehensive combination of different microscopic (LEEM, XPEEM, STM), diffraction (SPA-LEED, I/V-LEED) and spectroscopic (XPS) techniques shed light on the complex variability induced by changes in the preparation conditions of $Fe_3O_4(111)$ thin films. Following the known recipe, the sample preparation does not result in a completely flat and homogeneous surface, but leads to inhomogeneities of different nature. The morphology of the magnetite thin film is strongly influenced by the temperature at which the oxidation is performed. For films with thickness below 10 nm, an oxidation temperature of 1000 K leads to a de-wetting of the film, and the formation of holes some hundreds of nm wide, which expose a thin FeO layer that covers the Pt substrate. This de-wetting can occur even if the magnetite film presents, prior to the oxidation at high temperature, a clear $Fe_3O_4(111)$ LEED pattern with no FeO extra spots. Once formed, the FeO holes remain present even after further cycles of Fe deposition and oxidation. The Pt substrate morphology has an influence in the formation of the holes: it has been observed that they occur preferentially over the substrate step bunches. Therefore, it is expected that, for substrates with high step density (i.e. in case of higher Miller indexes), the formation of holes can be enhanced and a completely closed magnetite film can be obtained only with a careful monitoring of the oxidation temperature.

The surface of the "as prepared" sample is populated by objects a few nm wide. The formation of these objects at the end of the oxidation process - only during the final cooling in O_2 atmosphere - and the evidence in the XPS spectra that no other contaminants are present in significant quantities, lead to the conclusion that they are agglomerates of FeO_x that rest upon the standard terminated Fe_3O_4 surface (1/4 ML Fe over a close-packed oxygen layer) formed before. Though the STM data show that these objects have a regular almost crystalline shape, the I/V-LEED simulations did not lead to a clear model for the termination of the "as prepared" surface. This might be explained by the intrinsic limitation of this method. In fact, from the SPA-LEED and the STM results we know that the investigated objects are on average only 2 nm wide, corresponding to about "7 O atoms", therefore they do not fulfill the periodic boundary conditions assumed in the I/V-LEED analysis. On the contrary, these small objects have a large fraction of atoms at the island border with a correspondingly strong scattering

contribution. These border atoms are under-coordinated and geometrically shifted with respect to their positions under periodic boundary conditions, which cannot be considered by I/V-LEED simulations. This is also consistent with the change in shape of the O 1s and Fe 3p XPS spectra, which can be explained by the presence of surface O and Fe atoms with different charge states and coordination. In addition, the assumption of only two terminations coexisting could be too simple: the surface structure might be the result of the superposition of several co-existing metastable terminations, among the one that survives after the flash. However, the presence of FeO_x objects on the surface could in principle considerably increase the number and the kind of active sites (in example, under-coordinated Fe atoms of unknown charge state on steps and kinks) for the adsorption of molecules from the residual gas.

In general, such objects can also have strong consequences for understanding the catalytic behavior of the $Fe_3O_4(111)$: the local variation in stoichiometry might change the reactivity of the whole surface. Furthermore, it can affect the nucleation of metal nanoparticles (with the creation, modification or inhibition of the nucleation sites) and/or the encapsulation that occurs for example in the case of Pt nanoparticles on $Fe_3O_4(111)$[38]. The dynamic LEED analysis confirms that a flat surface with the regular and homogeneous termination according to literature can be obtained only with a flash at 900 K. This may be interpreted as a necessary "cleaning" process inducing migration and desorption of atoms in excess and subsequent rearrangement of the surface towards a homogeneous atomic termination, as well as desorption of oxygen atoms, segregation of iron atoms into the film and exposure of the canonical termination present beneath. In conclusion, the formation of FeO_x agglomerates under certain preparation conditions of the film and their stability at relatively high temperatures can help to sort out the discrepancies in the literature about the magnetite surface termination. Even a slight difference in the preparation conditions (for example the cooling rate of the system or the final flash performed at temperature below 900 K) can lead to substantial changes in its electronic properties, with important consequences for its behavior in catalysis.

Chapter 3

Fe_3O_4/Pt(111) thin film: the layer-by-layer growth

The described magnetite preparation recipe creates completely closed thin films with up to 100 nm wide terraces separated by steps of one unit cell height. The surface roughness increases with the thickness: for 20 nm thick films, the average terrace size decreases, i.e. the step density increases. The thin film roughness is very important for the LEEM/PEEM analysis, because a high step density distorts and blurs the image and therefore confuses the interpretation. Besides this, the steps are natural nucleation centers for deposited material. If the aim is to visualize and to study the creation of nanoparticles on a surface, a low step density helps to avoid messy situations. For these reasons, some effort was spent to develop new preparation recipes that can result in a more ordered and flat thin film surface.

As already observed[39], the temperature has the greatest effect in smoothing the magnetite surface. Performing the last oxidation at higher temperature, 1000 K instead of 900 K, increases the terrace average size. However, a further increase of the oxidation temperature brings the risk to destroy the thin film itself by desorption of O and Fe atoms, as observed above 1100 K. On the other hand, keeping the oxidation process at high temperature (i.e. 1000 K) for longer time does not help either: direct LEEM observation of the oxidation of the deposited Fe shows that the new film layer is formed within only some tens of seconds. Once formed, its morphology remains substantially stable. Therefore, the production of smoother magnetite thin films passes necessarily through the revision of the philosophy beyond the preparation method.

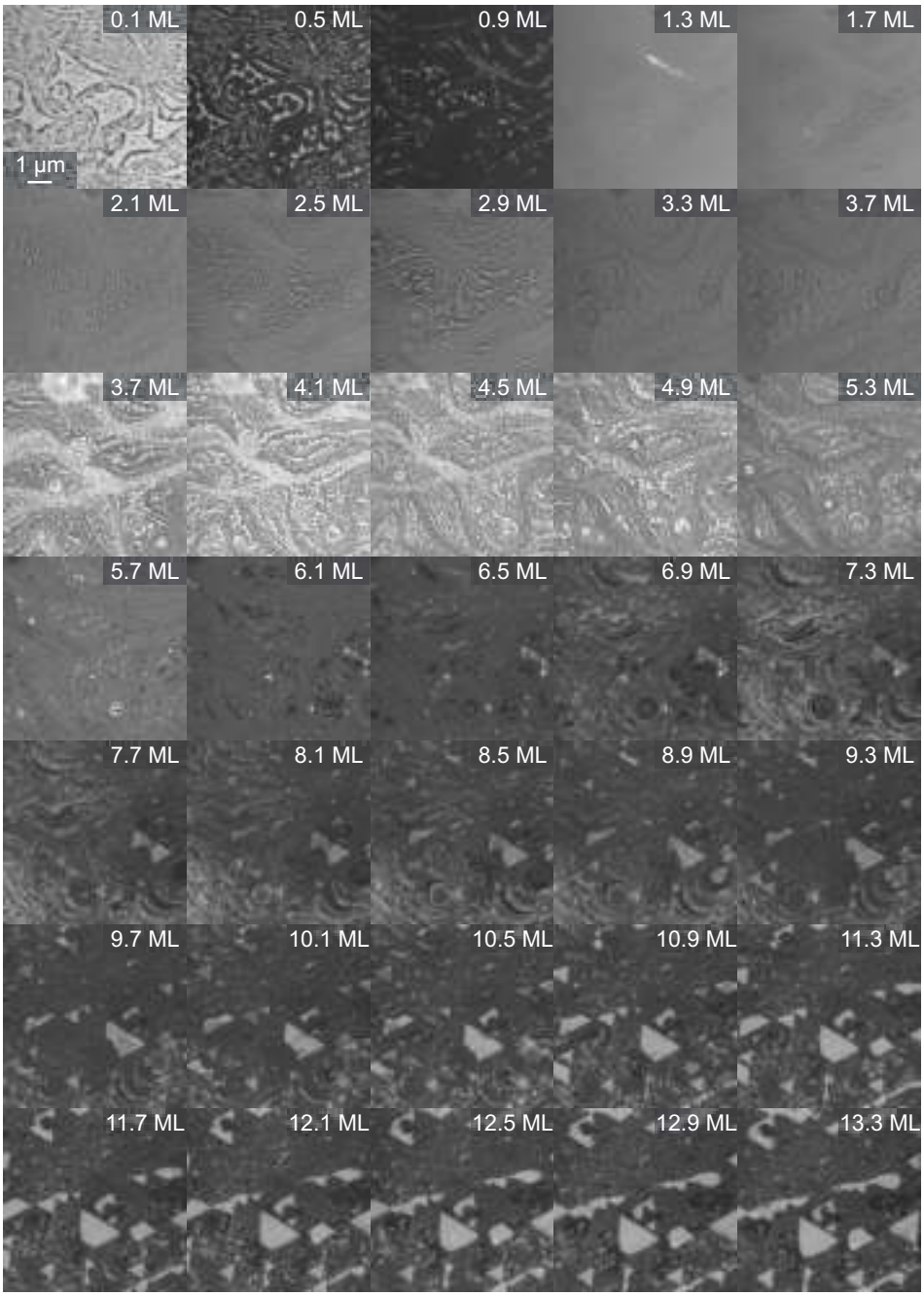

Figure 3.1: Direct observation of Fe deposition in oxidation conditions, T = 960 K, p = 1x10^{-6} mbar O_2, Fe flux = 0.27 ML/min. At 3.7 ML the growth was interrupted and the electron kinetic energy changed, from 15 to 18 eV, in order to enhance the contrast. After an initial layer-by-layer growth, Fe_3O_4 islands were formed above 6 ML. Image intensity is rescaled after 1.0 and 3.7 ML

The adopted recipe imposed a rigid division between (a) the Fe deposition at room temperature in UHV and (b) the oxidation process at high temperature. A different approach unites these two steps in one, i.e. Fe deposition on the Pt substrate under oxidation conditions at higher temperature. However, this procedure has the great drawback that it does not create a fully closed film, but isolated $Fe_3O_4(111)$ islands on a closed FeO thin layer. This kind of preparation has been already used by Santos *et al.*[42] to study the magnetism of ultrathin (1 nm) magnetite islands on a Ru(0001) single crystal. As a first approach to this different recipe, LEEM images of Fe deposition on Pt(111) were recorded in real-time, at 960 K and with an oxygen partial pressure of $1x10^{-6}$ mbar. **Fig. 3.1** displays selected frames of the iron oxide film growth. At the beginning of the Fe deposition, the FeO grew layer-by-layer like over the Pt(111) surface. The growth of the layers was well visible, because every layer has a different reflectivity. In this phase, it should be pointed out that, for FeO films thicker than 1 ML, the sticking coefficient of the Fe atoms can be lower than in the case of deposition on the bare Pt surface. This is due to the higher free energy required for the coverage of such polar systems, which probably had a slightly different stoichiometry compared to the pure FeO film. Therefore the real amount of iron oxide produced, expressed in **Fig. 3.1** in equivalent ML of FeO, might be overestimated. After the completion of a few polar FeO-like layers, the surface energy (which increases with the film thickness[31]) was so high that the additional deposited material crystallized in small three-dimensional Fe_3O_4 islands (bright objects above 6.1 ML). The crystal structure of the islands could be easily detected by spatially-resolved LEED (**Fig. 3.2a**): when the islands were included in the small illuminated area, the special diffraction spots typical for Fe_3O_4 appeared in the pattern. The FeO layers stopped growing in thickness and the deposited material, due to the high mobility at 960 K, contributed to enlarge mainly the magnetite islands. These had a distinct triangular shape, whereas the two possible orientations were not equally populated. A statistical analysis showed that the quantity of islands with the dominant orientation was about three times larger than the other type. Therefore, it is evident that the orientation was not randomly distributed, but triggered by the stacking sequence of the substrate. This aspect will be discussed in more detail in Section 3.2.1. During the deposition the magnetite islands did not only grow laterally in size, but mainly in height: it is clearly visible that atomic steps ran over the surface on top of the 3D islands. Some islands showed areas with different reflectivity; what can be explained as

the so-called quantum size effect of the island thickness, which modulates periodically (in energy) the reflected intensity in LEEM, due to the interference between the partial electron waves backscattered from the surface and from the film/substrate interface[57]. Even after about 15 ML of Fe deposited, the magnetite islands did not merge together to form a fully closed film. **Fig. 3.2b** shows the final state of the layer-by-layer growth, at room temperature in UHV conditions. Clearly, for this kind of growth, the substrate step bunches were favored nucleation sites for the magnetite islands. In fact, the elongated structure which traces out the step bunches was the result of the coalescence of a high number of small islands, while on the terraces the Fe_3O_4 islands were mainly isolated.

This experiment showed that the Fe deposition in oxidation condition offers a better control over the thin film growth: the possibility to see in real-time in LEEM the layer-by-layer growth of the Fe_3O_4 opens the door to parameters to control the preparation: the temperature, the oxygen partial pressure and the Fe deposition rate can be regulated with higher precision and stability; a single parameter can be changed in real-time to isolate its effect on the thin film preparation. In order to achieve the aim for a fully closed magnetite thin film on the surface - not possible for continuous growth starting from FeO/Pt(111) - a new strategy had to be set up by combining the two preparation recipes described, starting with the first one (Fe deposition and oxidation in separate stages) to build up a fully closed and sufficiently stable $Fe_3O_4(111)$ thin film, followed by Fe deposition on this template layer at high temperature with oxygen exposure. In this way the layer-by-layer growth can be enabled even for complete films and not only for small islands.

The first attempt has been performed with a thin (3 nm) and not perfectly closed $Fe_3O_4(111)$ film. The starting template (**Fig. 3.3**, first frame) showed a film created with the original recipe and with a very rough resulting surface. The morphology of the thin film still matched the step distribution of the Pt substrate. The step density at the surface was high; the typical dimension of the terraces was about 50 nm. Once the deposition started (**Fig. 3.3**, from the second frame onward), the atomic steps modified their shape and tent to align with the atomic rows direction. It is important to notice that, during the layer-by-layer growth, the predominant shape of the terraces was *triangular*. Since the magnetite unit cell has threefold symmetry, this means that one particular step alignment was energetically favored respect to the possible others. In this case,

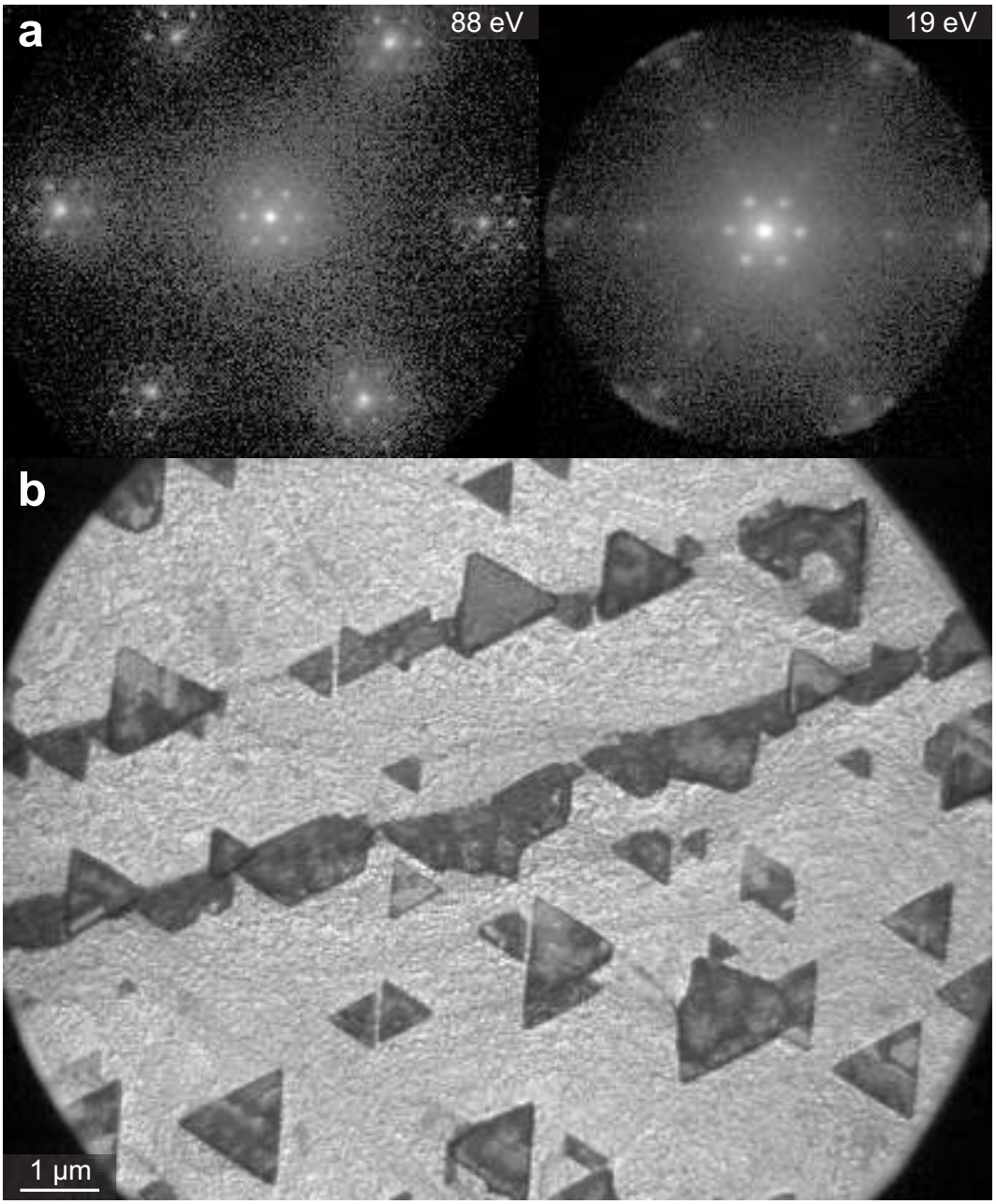

Figure 3.2: (a) LEED pattern of the iron oxide film grown in layer-by-layer mode for 3.7 ML (left) and 15 ML (right). The Fe_3O_4 spots are visible only in the right pattern, after the formation of triangular islands. (b) Sample surface after the deposition of 15 ML Fe in oxidation conditions. The dark triangular islands are Fe_3O_4, grown over a multilayer of FeO (bright). Along the step bunches of the substrate the magnetite islands coalesce to form stripe-like features. E_0 = 34 eV.

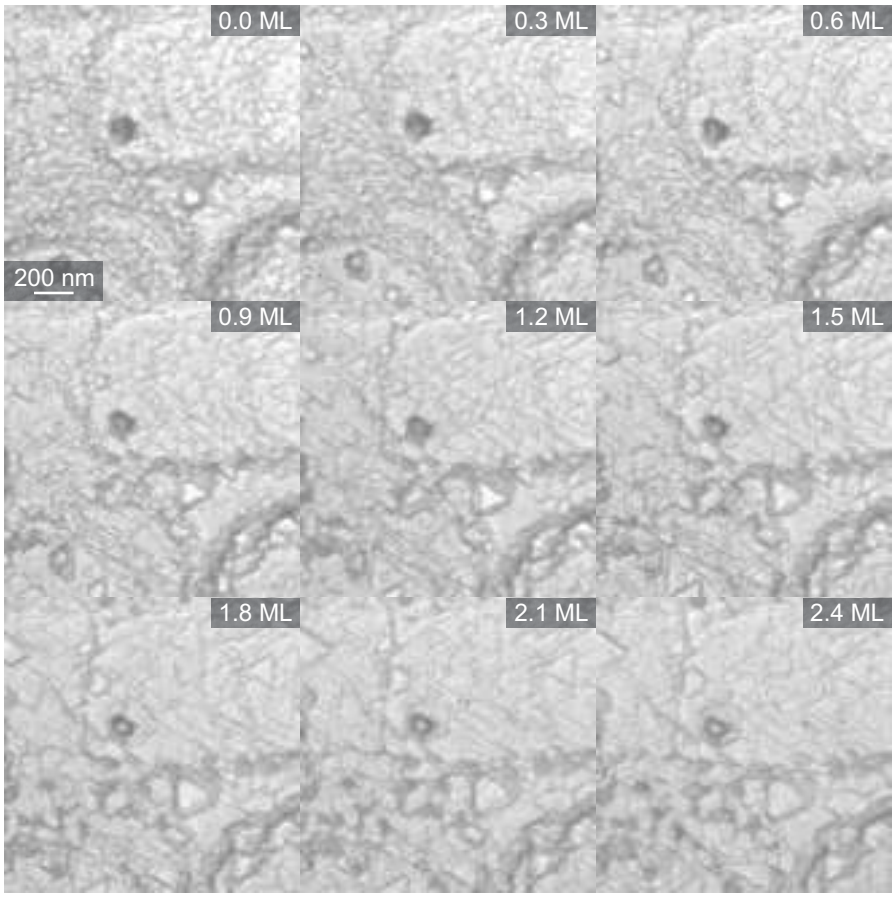

Figure 3.3: Step flow growth of mixed-phase FeO-Fe_3O_4/Pt(111) thin film. T = 900 K, p = 1x10^{-6} mbar O_2. The FeO areas become clearly visible after the deposition of about 1 ML, as the holes decorating the step bunches of the Pt substrate. E_0 = 20 eV.

the steps followed the [$\underline{1}$12] direction and the directions symmetrically equivalent. Together with the atomic steps alignment, the terraces started to grow and merged to create much larger structures: the step density decreased markedly. The growth occurred only by expansion of the atomic steps and not by creation of a new layer on a large terrace. This can be related with the fact that the magnetite unit cell has an inverse spinel structure, consisting of two hexagonally close-packed planes of oxygen with two alternating different planes of iron in between. The formation of a new layer on a terrace should require not only a simple deposition of material, but also a precise arrangement of the atoms in a double iron-oxygen layer, with the result that due to the high complexity of the magnetite unit cell the formation of a growing nucleus on a flat area could be less

probable. The Fe deposition in oxidation conditions had also an effect on the morphology of the thin film. If the preparation is not perfect, the film presents some small holes with FeO at the bottom. During the layer-by-layer growth the holes enlarged in size by a factor of 10, passing from 20-50 nm up to 400 nm (**Fig. 3.4**). This enlargement was not linear in time; the holes became stable after a few minutes.

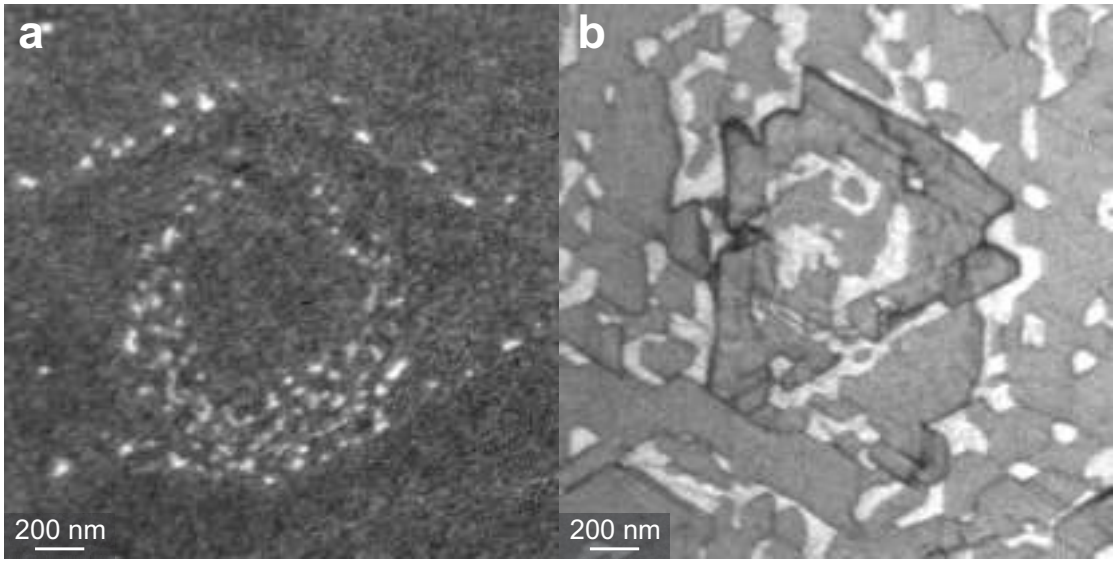

Figure 3.4: Different surface areas of an incomplete Fe_3O_4 thin film (in dark) with FeO holes (in white), before (a) and after the layer-by-layer deposition (b). E_0 = 13 eV (a) and 19 eV (b). The dark lines in (b) are facets of the Fe_3O_4; their formation is induced by the circular step bunch of the substrate.

Subsequently, a new film was grown layer-by-layer like on a completely closed and thicker Fe_3O_4 film (**Fig. 3.5**). In this film steps and fractures are visible, grouped in wavy structures, which are produced for compensating the strain induced by the substrate step bunches. The deposition of a few ML Fe in oxidation condition enhances again the terrace width by an order of magnitude and aligns the steps along a particular direction. During the deposition, no FeO domains were produced: the film remained compact and homogeneous.

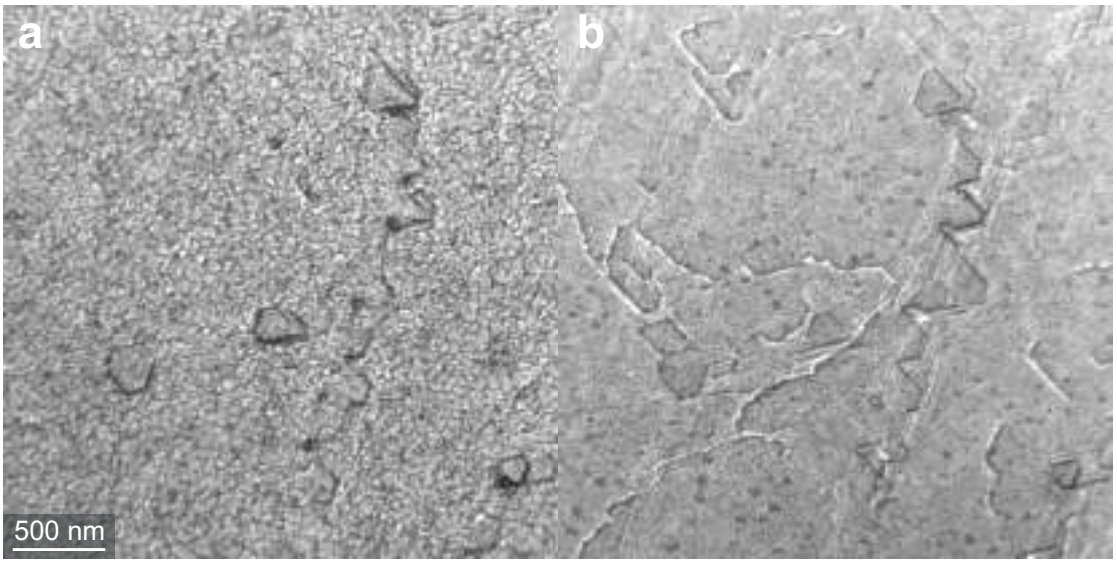

Figure 3.5: Closed Fe_3O_4 film before (a) and after (b) the deposition of 6 ML of Fe in oxidation conditions, T = 1000 K, p = 1x10^{-6} mbar O_2. E_0 = 29 eV. The identical surface area is shown.

3.1 Morphology

3.1.1 Isolated line defects

The surface smoothed by the Fe deposition in oxidation conditions presents peculiar features on the surface, which were not observed on a film formed with the standard growth procedure. During deposition, in addition to the well-known step flow, another kind of surface feature becomes visible: a linear defect that appears like a segment, with a beginning and an ending point (**Fig. 3.6a**). Its dynamic behavior during the growth is similar to that of a step: it flows on the surface only during the deposition and stops if the Fe flux is interrupted. Therefore, its atomic structure is related to a discontinuity in the lattice periodicity, in which the deposited material can be accommodated. The linear defects follows the alignment of the atomic steps, along the [$\underline{1}$12] direction and equivalents. However, its appearance does not match the one for a standard atomic step. In LEEM the intensity line profile of the step contrast is a consequence of the interference of the Fresnel diffracted electron waves from two adjacent terraces[58]. Normal inci-

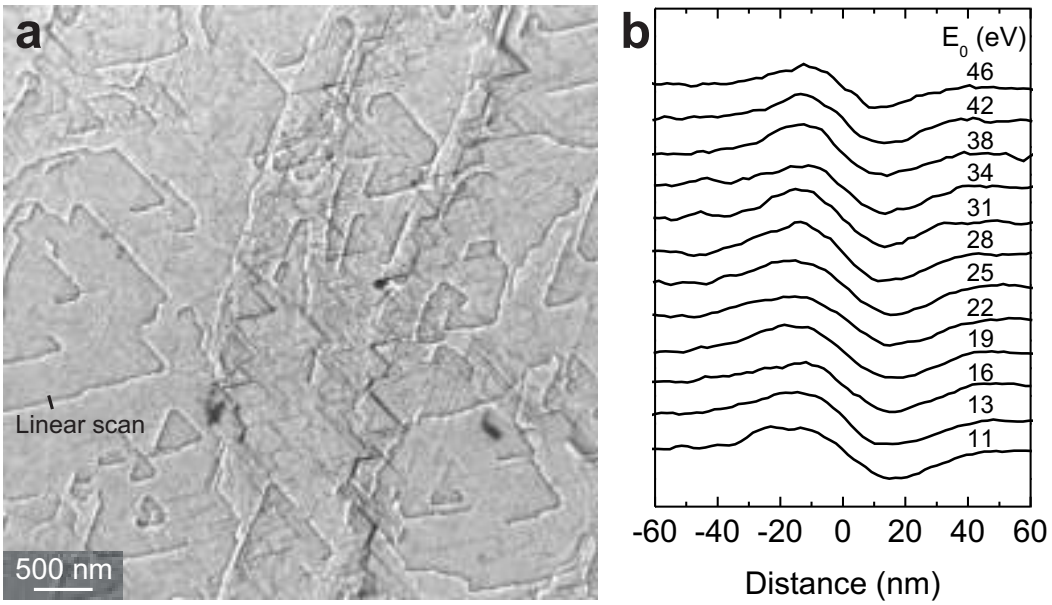

Figure 3.6: (a) Closed Fe_3O_4 film after layer-by-layer deposition. The substrate step bunches are visible as vertical stripes with higher step density. The line defects are clearly visible as segments with strong contrast, while the atomic steps are simple black stripes. The image is in slight over-focus, E_0 = 29 eV. (b) Linear scan profiles of the line defects in under-focus conditions for different electron kinetic energies.

dent electrons backscattered from neighbored terraces of different height have a relative phase shift of $2k_\perp a_0$ where $k_\perp$ is the electron wave vector component perpendicular to the surface and a_0 is the step height. The interference between phase-shifted waves diffracted by adjacent regions creates the step contrast. In out-of-focus conditions, the step contrast shows an asymmetry (the region close to one side of the line has higher intensity than the other) that changes periodically with the electron phase shift, i.e. with the square root of the starting kinetic energy E_0. This periodicity was not observed in the new surface features, but the asymmetry in the line profile was constant (**Fig. 3.6b** - the brighter side does not change with the starting kinetic energy). Furthermore, the asymmetry changed its sign with the focus: bright and dark sides were inverted when one passed from over-focus to under-focus conditions. In over-focus conditions, the

flow of a linear defect during the deposition occurred always in the direction of the bright side. A detailed discussion about these aspects will be given in Section 3.1.3.

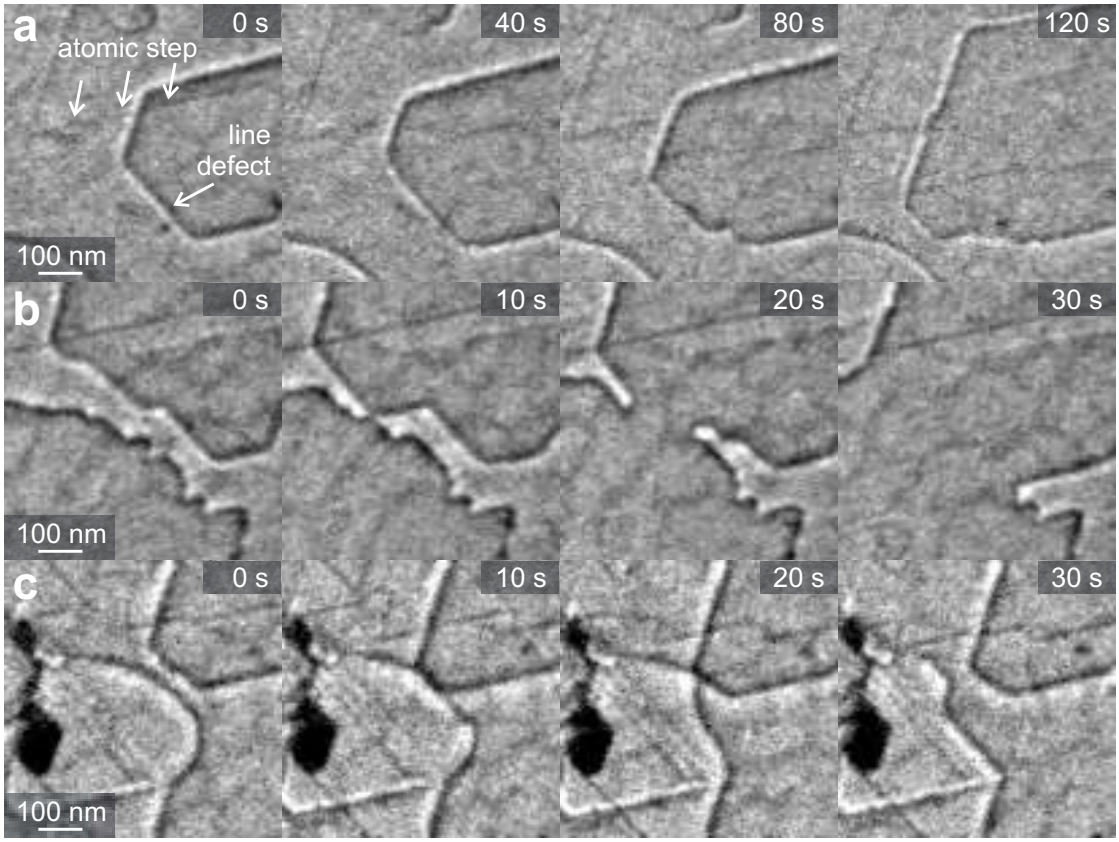

Figure 3.7: Dynamic of atomic steps and line defects during the layer-by-layer growth. The (a) series shows the independent flow between the features, (b) displays how linear defects with opposite contrast merge together, while in (c) two linear defects with concordant contrast remain separated. Deposition rate 0.22 ML/min, E_0 = 29 eV, slight over-focus.

During the layer-by-layer growth, the line defect flow and the step flow ran independently, i.e. even when crossing they do not modify each other (**Fig. 3.7a**). The new feature is therefore a type of defect that does not alter the structure of a step. In the growth it is also clearly visible that two line defects could annihilate each other, but only if their contrast asymmetries were inverted (**Fig. 3.7b**). If they presented the same

contrast asymmetry, the cancellation did not occur (**Fig. 3.7c**). From this behavior one can conclude that the contrast asymmetry is a consequence of an *orientation* of the defect, like in the case of two standard atomic steps flowing against each other: two steps with opposite orientation (the lower terrace of the one is the lower terrace of the other) can cancel each other and form a unique flat terrace; two steps with the same orientation (the lower terrace of the one is the higher terrace of the other) do not merge together, but might create a double step. All these observations bring us to the conclusion that the line defects behave exactly like an atomic step, but with a different nature with respect to the standard atomic step visible in LEEM.

Although they do not appear like steps in LEEM, their topology reminds in first analysis the topology of steps generated by screw dislocations. In a compact and defect-free crystal a surface step is always a closed line, in case of holes or islands, or an infinite line (crossing the whole surface) that reflects the miscut of the crystal surface. A real crystal can present several crystallographic defects; among them are the dislocations. They are formed when an incomplete extra plane of atoms are inserted in the periodic planes of the crystal. The magnitude of the lattice distortion is represented by the so-called Burgers vector, which quantifies the position shift of a portion of the crystal respect to the non-distorted case, i.e. the *strength* of a dislocation. The dislocation line is the *locus* in which the lattice periodicity is not satisfied. The Burgers vector $\mathbf{b}$ can be written as

$$\oint_{\Gamma} \mathrm{d}\mathbf{u} = \mathbf{b} \tag{3.1}$$

for any closed circuit around the dislocation line[59] (see **Fig. 3.8a**). When the dislocation line crosses the surface, it generates the so-called screw dislocation: the atomic planes follow a helix path around the dislocation line, so that on the surface a step is formed. Typically these steps look like long segments which can connect two screw dislocations: as an example, in **Fig. 3.8b** is presented one with the related atomic steps measured in LEEM on the Pt(111) surface. From these considerations, the main supposition is that the line defects are related to line dislocations. The fact that in a LEEM image line dislocations in Fe_3O_4(111) thin films do not look like normal atomic steps could be ascribed in first analysis to the much more complex unit cell geometry. In fact,

the Fe_3O_4(111) unit cell consists of four alternate layers of Fe and O atoms. A line dislocation in a crystal with such complex unit cell could in principle have a strength which is only a *fraction* of the unit cell length. Such consideration will be discussed in Section 3.1.6.

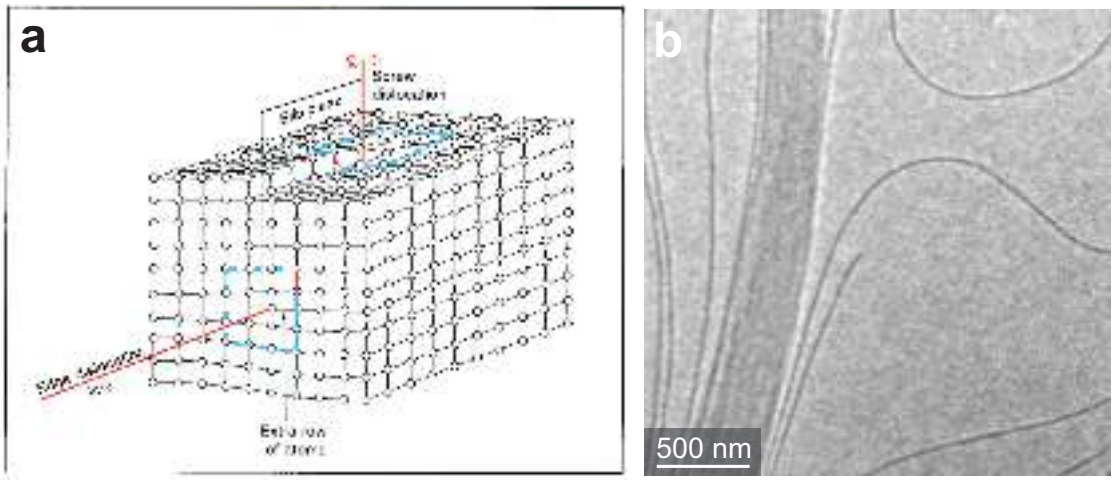

Figure 3.8: (a) Scheme of a dislocation in a simple cubic crystal. The blue arrows indicate the Burgers circuit, the red arrows the Burgers vectors. (b) Screw dislocation on Pt(111) surface, visible as a demi-infinite line. E_0 = 19 eV,

The suggestion that line defects are related to dislocations is supported by the fact that they appear only after deposition of several ML of Fe with the layer-by-layer growth. Typically, dislocations are induced by strain in the crystal. In Section 2.2.3, it has been reported that the Fe_3O_4(111) thin film presented a much larger mosaic spread than the Pt(111) substrate, i.e. the magnetite thin film was not perfectly flat, but composed by areas slightly tilted against each other. This can be a consequence of the mismatch between the step height of the Pt(111) surface (2.27 Å) and the separation of the iron layers in the Fe_3O_4 unit cell (1.83 or 2.35 Å), which can produce a local tilt of the (111) planes of the film. The freshly prepared magnetite film presented a high step density (see **Fig. 3.5**, first frame), which makes it difficult to identify local crystallization defects. During the layer-by-layer growth, the step density decreased dramatically (the average terrace size enlarged by a factor of 10) with increased thickness. As a consequence, the accumulation of strain could favorite the formation of extended dislocation. In this sense it is important to notice that in **Fig. 3.6a** the three line defects direction were equally

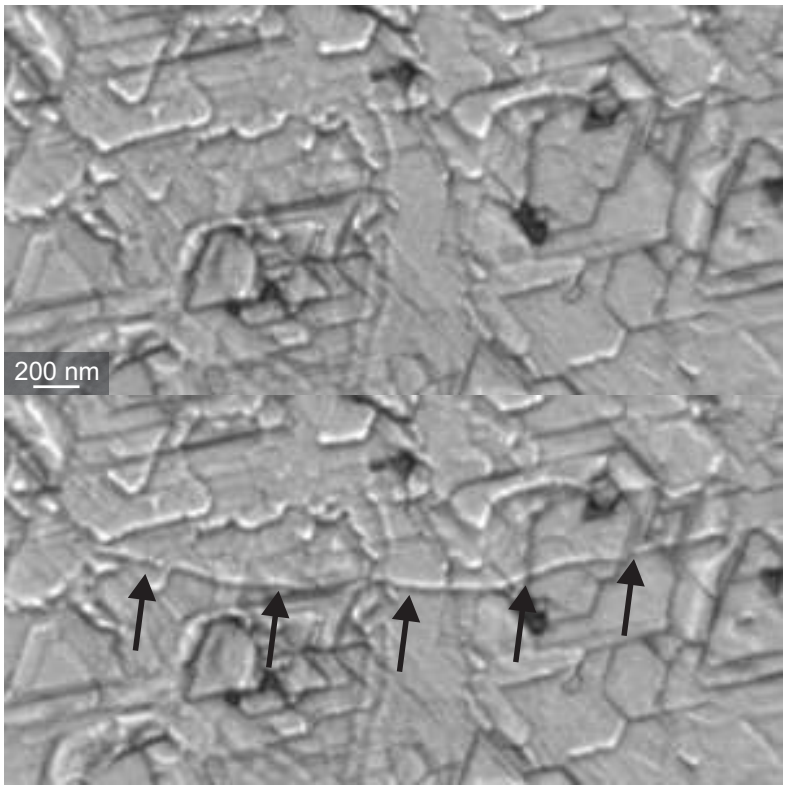

Figure 3.9: Fast creation of line defects during the layer-by-layer growth. Bright field LEEM images of the same area, in slight over-focus. The second frame was taken 2.2 s after the first one. In this time interval, a new line defect, about 2.7 μm long and highlighted with black arrows, was formed. E_0 = 29 eV, slight over-focus.

present on the terraces, while they had a preferential direction when formed over the substrate step bunches. This is coherent with the expectation of the strain direction, which should be randomly distributed on terraces, while on step bunches should be polarized on the step direction. Moreover, it has been observed during the layer-by-layer growth that, while some line defects grew gradually in size with a continuous flow, some others were created in about one second and could be even several microns wide (**Fig. 3.9**). This particular behavior confirms that the line defects can be formed from major fractures of the thin film, which can be produced in such short time in order to accommodate the strain induced by the deposition. This argument will be expanded with theoretical considerations in Section 3.1.4.

The analysis of the line defect extremes, where a screw dislocation is expected, gave

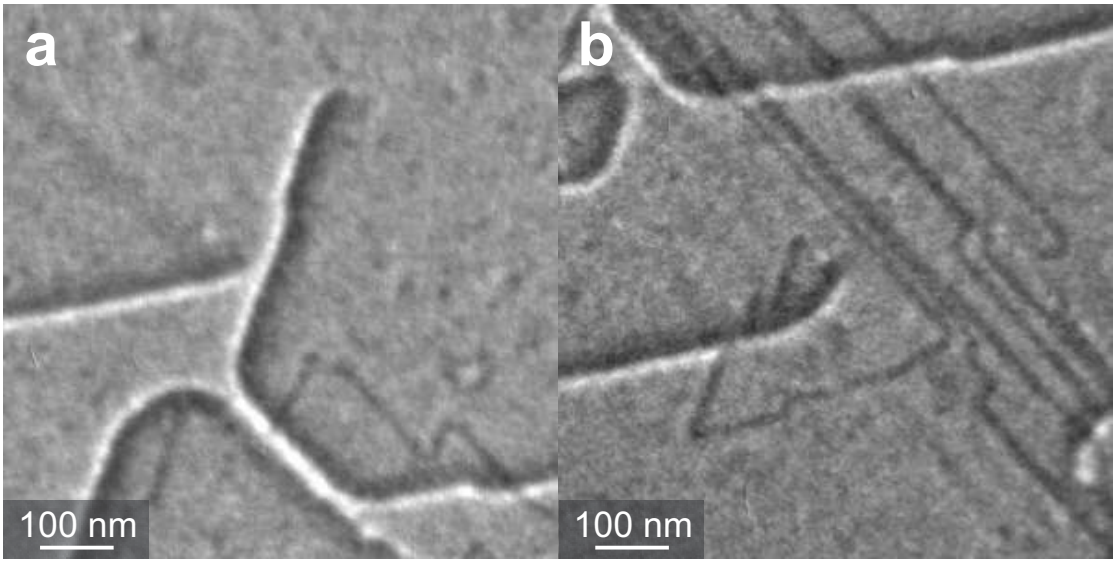

Figure 3.10: Extremes of the isolated line defects. Fractional steps can be generated from a flat surface (a) or from a step (b).

new insights on the nature of the line defects. Two kinds of extremes were found. In addition to the usual case, in which the line defect was generated out of a flat surface (**Fig. 3.10a**), there was a case in which a normal step was converted to a line defect (**Fig. 3.10b**). These two possibilities can be explained with a model describing the line defect as a dislocation with strength along the [111] direction smaller than the unit cell length. In the usual case the shift generated by the dislocation is compensated by the lattice strain around the screw dislocation, i.e. they are opposite in sign. The new case can be modeled by assuming that the step and the strain have concordant sign, i.e. the lattice distortion act in the same direction of the Burgers vector, and combine together to form a regular step. Both cases were detected on the surface with almost the same probability. During the layer-by-layer growth, the step and the line defect of the second case flew independently as reported before, but always keeping the contact point at the extreme.

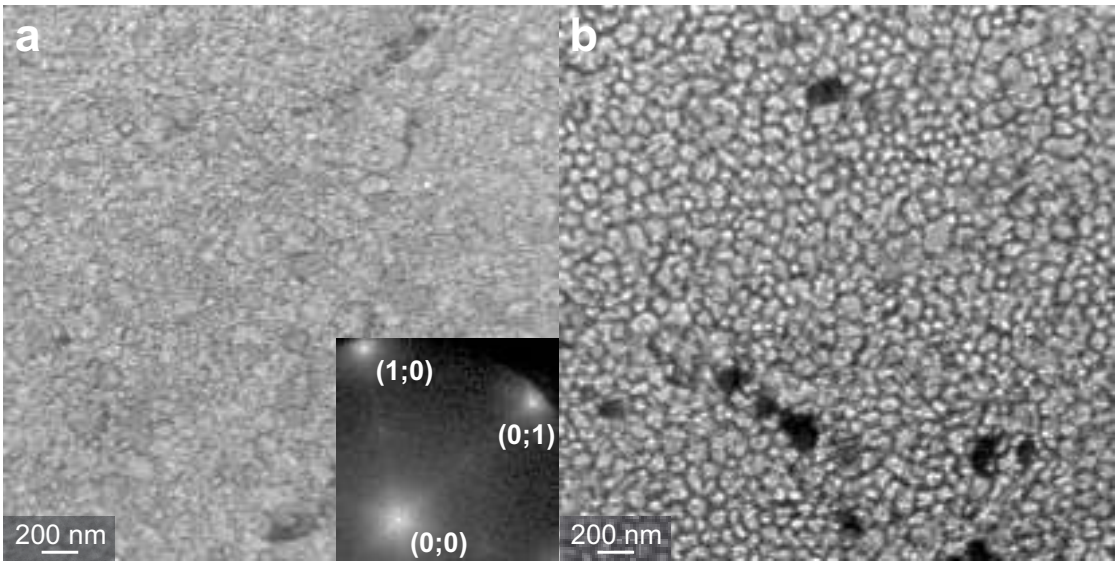

Figure 3.11: Appearance of a defect network. (a) LEEM (E_0 = 10 eV) and LEED (E_0 = 24 eV) images of the initial template thin film. The satellite spots in LEED attests a biphase ordering of the surface. (b) over-focused LEEM image of the film after the deposition of 8 ML of Fe in oxidation conditions. The network of line defects covered the entire surface. The black patches were isolated film holes covered by FeO(111). E_0 = 29 eV.

3.1.2 Line defect network

In addition to the atomic steps and the line defects, a third surface feature was detected, a network of thick lines with hexagonal order over the entire thin film surface. This feature was produced with Fe deposition in oxidation conditions on a particularly rough initial template film, built with 9 ML of Fe oxidized at 890 K. **Fig 3.11a** shows LEEM and LEED images of a rough film, mainly terminated with biphase ordering. After the Fe deposition, LEEM images of the thin film in perfect focus showed a film with large terraces and some line defects discussed in the previous section. However, in out-of-focus conditions, the magnetite thin film revealed the presence of domains separated by thick lines arranged in a hexagonal pattern (**Fig 3.11b**). The analysis of the auto-correlation function of images with large field of view showed that the domains were

aligned along the O atomic rows and that their average size was 95 nm. By comparison of the two images, before and after the deposition, it emerges that the domain network resembled the morphology of the template thin film.

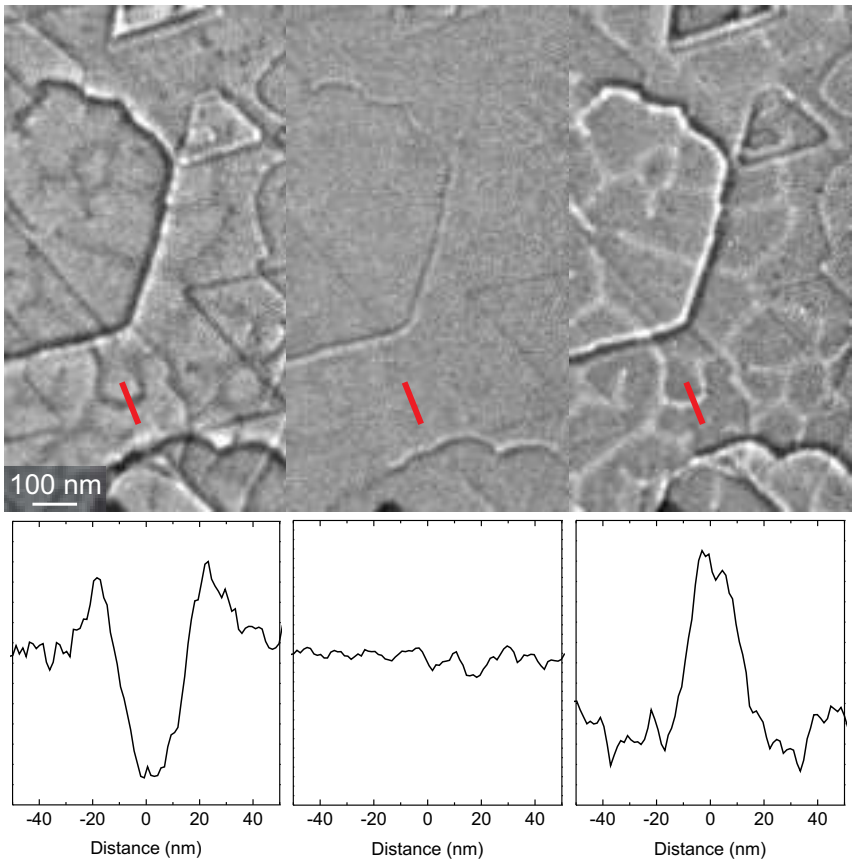

Figure 3.12: Network of line defects in LEEM. The same area was detected in LEEM in over-focus (left), in-focus (center) and under-focus conditions (right). Intensity profiles of the lines, taken along the red segments, are depicted below every image. Isolated line defects and atomic steps are also visible. E_0 = 29 eV.

A more detailed insight on the network lines shows that their appearance in LEEM is related with the focus value. **Fig. 3.12** shows the same sample area in three different focus conditions: over-focus, in-focus and under-focus. As highlighted in the line profiles below the images, in the first case the lines appear dark with bright contours, while in the last they appear bright with dark contours. In focus conditions, they cannot be detected. Furthermore, it should be noticed that the network is not perfectly closed,

but some lines have an end like the isolated line defects discussed before. This aspect leads to think that they are also crystallization defects, a different kind of dislocation compared to the isolated line defects of Section 3.1.1.

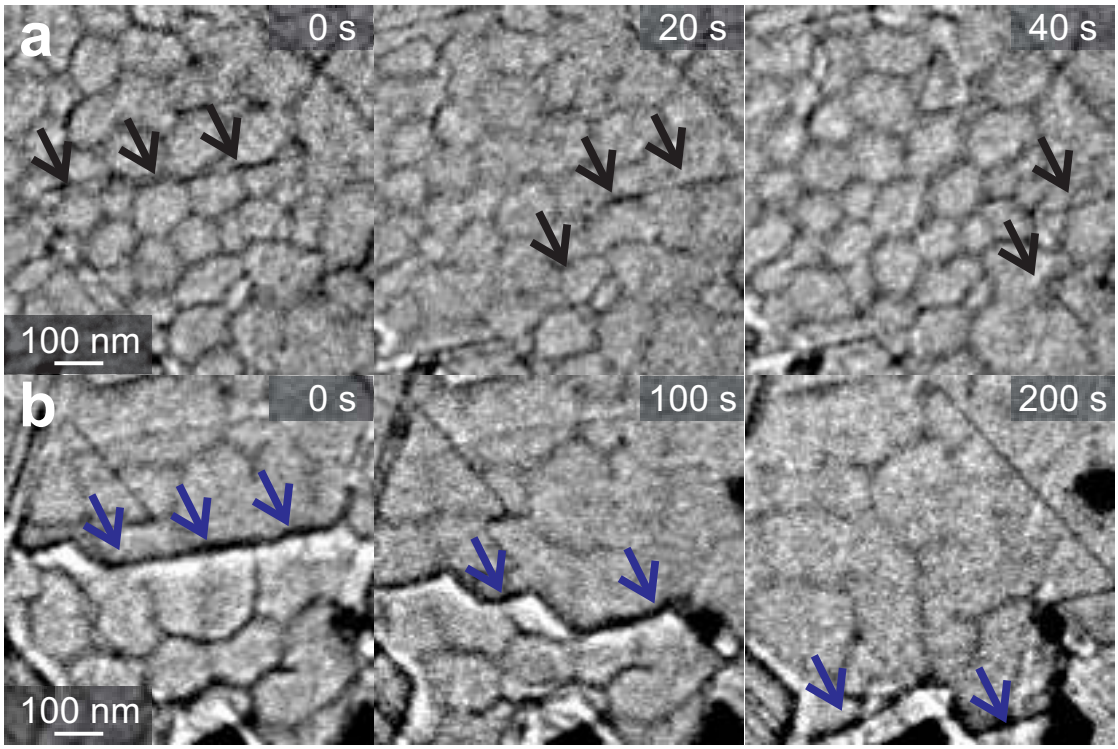

Figure 3.13: Interaction between line network and other surface features. (a) Flow of an atomic step (highlighted with black arrows) over the network did not lead to a significant change. (b) Motion of an isolated line defect (highlighted with blue arrows) over the network caused a rearrangement. Deposition rate, 0.22 ML/min, E_0 = 29 eV.

Unlike the isolated line defects, the line network stayed static during the Fe deposition in oxidation conditions. No motion was detected under any Fe flux, temperature or oxygen pressure condition. Furthermore, the network was not modified if an atomic step flowed on/through it (**Fig. 3.13a**). This means that the line network, although appeared as a surface feature, is an effect of a crystallization defect that ranges deeper into the film. On the contrary, the line network was strongly modified by the transit of an isolated line defect. **Fig. 3.13b** shows that the network appeared deeply rearranged: the passage of an isolated line defect erased part of the network and created a new one.

This can be explained with the idea that both isolated lines and line network are surface exhibitions of sub-surface dislocations, which can interact with each other. The motion of one dislocation forces a rearrangement of the atoms that modifies the structure of the other dislocation. Their different appearance in LEEM testifies a different nature of such dislocation; in order to fully investigate this aspect, a LEEM image contrast simulation code was written.

3.1.3 LEEM simulation with Contrast Transfer Function formalism

In LEEM, the image is formed by electrons elastically backscattered from the sample surface. The contrast arises from the interference of the Fresnel diffracted electron waves. Over the last 15 years, several approaches were introduced to calculate the image formation in LEEM, partially adapting the methods already developed for Transmission Electron Microscopy (TEM)[60,61]. The first example was from Chung and Altman[58,62], which developed a wave-optical model to describe the step contrast in ideal and real conditions, i.e. taking into account the instrumental resolution and the beam coherence. This model was later improved by a Fourier Optics (FO) formalism[63], which allows the image contrast calculation for amplitude and phase objects, including the objective lens aberration effects, diffraction cut-off by a contrast aperture, lens defocus, energy spread and size of the electron source, as well as instabilities in lens current and voltage. In parallel, Jesson and coworkers[64,65] proposed a wave optical treatment of ideal surfaces with Contrast Transfer Function (CTF) formalism, in which the effects already included in FO are directly incorporated into a transfer function. This method was then integrated with fifth-order aberrations by Schramm *et al.*[12]. The CTF is an attractive approach because it has a low computational cost and allows image calculation for arbitrary phase, amplitude and mixed amplitude-phase objects. In the following, a brief explanation of the CTF principles with aberrations up to the third order is depicted.

Suppose to have an object illuminated by a uniform plane wave

$$\psi_{in} = \psi_0 \, e^{\mathbf{k}_{in} \cdot \mathbf{R}} \tag{3.2}$$

where $\mathbf{R}$ is the 3D position, ψ_0 is the amplitude and $\mathbf{k}_{in}$ is the wave vector. The plane wave is then reflected by the object, which cause spatial variation of the amplitude and the phase. Generally, the resulting wave is given by

$$\psi_{out} = \psi_{in} * \psi_{obj} \tag{3.3}$$

with

$$\psi_{obj}(\mathbf{R}) = \sigma(\mathbf{R})\, e^{(\mathbf{k}_{out}-\mathbf{k}_{in})\cdot\mathbf{R}} \tag{3.4}$$

Here σ is the amplitude modification factor, while the phase difference between out-going and incoming wave vectors induces a phase modification factor. In condition of normal incidence, only the vertical component survives, i.e. $\mathbf{k} = |\mathbf{k}|\hat{z}$. Now, given that $|\mathbf{k}| = 2\pi/\lambda_0$ and supposing that the specimen has a 2D local surface height $h(\mathbf{R})$ expressed in unit of the step height a_0, the phase shift is given by

$$(\mathbf{k}_{out} - \mathbf{k}_{in}) \cdot \mathbf{R} = 2\frac{2\pi}{\lambda_0}\, a_0\, h(\mathbf{R}) \tag{3.5}$$

The reflected plane wave is then modified by the cathode immersion lens, in which the electrons are accelerated from start energy E_0 (equal to $< ug >$ in the SMART control program) to the base energy E (equal to 15 keV), and the objective lens of the LEEM imaging system: the final image wave $\psi(\mathbf{R})$ results the convolution of the out-coming wave $\psi_{out}(\mathbf{R})$ with the contrast transfer function $T(\mathbf{R})$, which is the complex point spread function that incorporates the effects of the lens system.

$$\psi(\mathbf{R}) = (T \otimes \psi_{out})(\mathbf{R}) \tag{3.6}$$

Using the simple mathematical fact that a convolution in real space corresponds to a multiplication in the Fourier space (Convolution theorem), the description is much easier in the spatial frequency space. Then, given $\mathbf{q}$ the 2D coordinate in reciprocal space and $\mathscr{F}$ the Fourier operator,

$$\psi(\mathbf{R}) = \mathscr{F}^{-1}\left[\mathscr{F}[T(\mathbf{R})] * \mathscr{F}[\psi_{out}(\mathbf{R})]\right] \tag{3.7}$$

The acceleration in the quasi homogeneous electric field of the cathode immersion lens imposes a parabolic trajectory to the electrons traveling from a specimen placed at a distance L (**Fig. 3.14**, black trajectory). This real situation can be converted to a virtual frame[64,66] in which electrons assume linear trajectories. In case of an ideal homogeneous field, the virtual image plane, i.e. the plane from where the electrons appear to originate, is placed at a dposition of L behind the surface (**Fig. 3.14**, blue trajectory). The field distortion induced by the aperture in the lens can be taken into account by assuming that the uniform field is terminated by an ideal diverging lens with focal length -4L. This lens forms a virtual image of the virtual specimen at point B, located at a distance 4L/3 from the anode (**Fig. 3.14**, red trajectory). The electron beam is then magnified by the field of the objective lens by a factor of M_M. The relative coordinate change, from specimen spatial and angular coordinates, (x_0,θ_0), to image coordinates (x,θ), can be described as follows. Given the overall lateral magnification of the objective lens M (equal to 18 for SMART), and the immersion factor defined as k = E/E_0 , one has the following relations:

$$\begin{aligned} &M = \frac{2}{3} M_M\,, \qquad M_A = \left(k^{1/2}\, M\right)^{-1}, \\ &\frac{x}{x_0} = M\,, \qquad \frac{\theta}{\theta_0} = M_A\,, \qquad \frac{q_0}{q} = M \end{aligned} \tag{3.8}$$

whereas q_0 = θ_0/λ_0 and q = θ/λ are the spatial frequency parallel to the surface in the specimen plane and in the virtual plane respectively. For the LEEM imaging system, the contrast transfer function is modeled as a product of all relevant contributions imposed by the optical system[63]. Given $T(\mathbf{q})$ as the Fourier transformation of $T(\mathbf{R})$,

$$T(\mathbf{q}) = M(\mathbf{q})\, W(\mathbf{q}, \Delta f)\, \mathcal{E}(\mathbf{q}) \tag{3.9}$$

Here, $M(\mathbf{q})$ incorporates the effect of a round contrast aperture in the diffraction plane

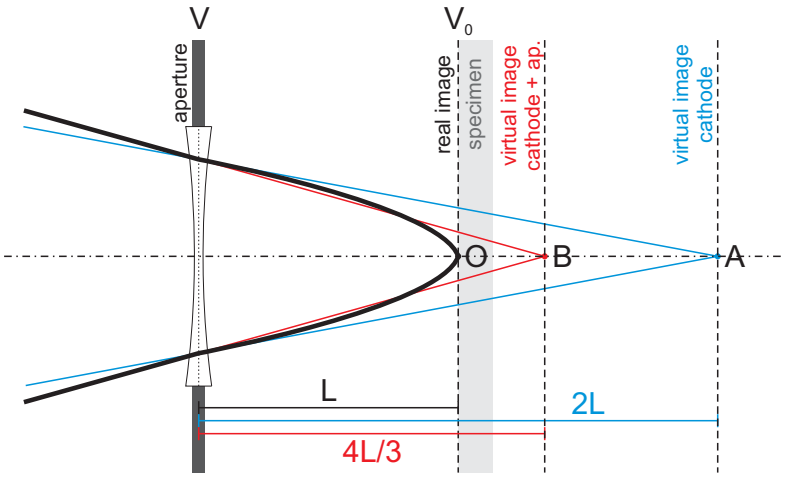

Figure 3.14: Scheme of the cathode immersion lens. Electrons reflected at point O (set at potential V_0) are accelerated toward the anode at potential V and are affected by the field distortion created by the anode aperture (black trajectory). The electrons travel a parabolic path in the uniform field between specimen and aperture, and appear to originate from a point A located in a virtual image plane at a distance $2L$ from the anode (blue trajectory). The anode aperture can be modeled as a diverging lens. This lens forms a virtual image of the virtual specimen at point B, located at a distance $4L/3$ from the anode (red trajectory).

and can be represented by a low-pass filter,

$$M(\mathbf{q}) = \begin{cases} 1 & \text{if } |\mathbf{q}| < q_{max}, \\ 0 & \text{if } |\mathbf{q}| \geq q_{max} \end{cases} \tag{3.10}$$

q_{max} can be calculated as α_{max}/λ, where α_{max} is the maximum angle permitted by the aperture and λ is the electron wavelength.

The wave aberration contribution $W(\mathbf{q}, \Delta f)$ refers to deviations of the wave path from ideal, which are function of the defocus Δf, and of spherical aberrations, expressed by the third-order coefficient C_s (see Section 1.3). It can be described[64] as

$$W(\mathbf{q}, \Delta f) = exp\left(\frac{\pi i}{2}(C_s \lambda^3 q^4 - 2\Delta f \lambda q^2)\right) \tag{3.11}$$

Finally, the chromatic-aberration damping envelope $\mathcal{E}(\mathbf{q})$ comes from an integration

over the weighted contributions of the different energies within the energy distribution, which is assumed to be a Gaussian function with FWHM ΔE[61]. Therefore, being C_c the chromatic aberration coefficient (see Section 1.3), one has that

$$\mathcal{E}(\mathbf{q}) = exp\left(-\frac{(\pi C_c \lambda q^2)^2}{16\, ln2}\left(\frac{\Delta E}{E}\right)^2\right) \tag{3.12}$$

The final result is the intensity image, which is calculated as the squared modulus of $\psi(\mathbf{R})$.

$$I(\mathbf{R}) = |\psi(\mathbf{R})|^2 \tag{3.13}$$

Following this procedure, a code was written in LabVIEW and IDL. Both program suites are able to create, manage and analyze images. The Fourier transformation was performed via Fast Fourier Transform algorithm. The code accepts as input the image dimension (in real space and pixels), the step height, the start and base electron energy, the aperture size, the linear magnification and values for C_C, C_S, Δf and ΔE. The program was then tested with a surface height function $h(\mathbf{R})$ that resembled an ideal step, i.e. a 2D Heaviside function. The results were in full agreement with the references given before.

3.1.4 Surface deformation from sub-surface dislocations

In order to simulate how sub-surface dislocations appear in LEEM, various surface height profiles have been modeled, which were consistent with the lattice displacement generated by the stress field of a dislocation. In the following, a brief overview about the dislocations is presented.

In general, when two crystals with different lateral displacement a (substrate s and film f) join each other, the atoms in the near vicinity of the boundary between them are displaced from their ideal position. Two lateral forces act on each atom: a) from the neighboring atoms of the same crystal, which tends to preserve the proper bond length, and b) from the neighboring atoms of the other crystal, which tends to force the atom

to occupy a position coherent with their lattice. In the case of a thin film built over a substrate crystal, if the interfacial bonding is much weaker than the lateral bonding, both crystals tend to preserve the natural lattice. If the interfacial bonding is comparable to the bond strength of the substrate, but much larger than the lateral bonding of the film, the film is forced to adopt the lattice of the substrate. In this case, the total elastic energy per unit area in the adlayer can be written[67–69] as

$$E_\varepsilon = h \int \sigma \, \mathrm{d}\varepsilon \tag{3.14}$$

where h is the layer thickness, σ is the stress in the layer and ε is the strain in the layer. The stress in the layer is related to the strain by $\sigma = Y\varepsilon$, being Y the Young elastic modulus. Without dislocation, ε corresponds to the misfit strain φ

$$\varepsilon = \varphi = \frac{a_s - a_f}{a_s} \tag{3.15}$$

Introducing dislocations at the interface with average distance S and made by a Burgers vector of strength b parallel to the interface, the strain in the layer becomes

$$\varepsilon = \varphi - \frac{b}{S} = \varphi - \delta \tag{3.16}$$

So, once solved the integral for $\sigma = Y\varepsilon$, the total strain energy per unit area in presence of dislocations is

$$E_\varepsilon = \frac{1}{2} Y h (\varphi - \delta)^2 \tag{3.17}$$

In the calculation of the total energy, the energy of the dislocation line per unit area has to be taken into account as well. This is approximately[69]

$$E_d = \frac{Y b^2}{4\pi S} \left(ln \frac{h}{b} + 1 \right) \tag{3.18}$$

The formation of dislocations occurs only when the total energy $E_T = E_\varepsilon + E_d$ has a

minimum regarding δ for $\delta > 0$, i.e. for a real and finite value of the spacing S at given Burgers vector strength b.

$$\frac{\partial E_T}{\partial \delta} = 0 \quad \Longrightarrow \quad \delta = \varphi - \frac{b}{4\pi h}\left(ln\frac{h}{b} + 1\right) \tag{3.19}$$

The condition $\delta > 0$ is only satisfied if the film thickness is above a specific critical value h_c,

$$h_c = \frac{b}{4\pi\varphi}\left(ln\frac{h_c}{b} + 1\right) \tag{3.20}$$

This equation cannot be solved analytically for h_c. For this result, h_c is under the assumption that the strain is assumed to be uniaxial, i.e. that one material compressed (or stretched) in one direction, no extension (or contraction) in a direction perpendicular is produced. Since the opposite (i.e. vertical contraction at horizontal extension) is usually the case, the last expression can be improved[68] by taking into account the Poisson ratio ν, defined as the ratio between the induced transverse strain and the axial strain, the angle α between the dislocation line and its Burgers vector and the angle β between the slip direction and that direction in the film plane perpendicular to the intersection of the slip plane and the interface:

$$h_c = \frac{b}{4\pi\varphi}\frac{(1 - \nu\, cos^2\alpha)}{(1+\nu)cos\beta}\left(ln\frac{h_c}{b} + 1\right) \tag{3.21}$$

This result indicates that dislocation with a particular orientation of the Burgers vector can appear only if the film thickness is above the critical value. The fact that isolated line defects and the line defect network in the Fe_3O_4(111) thin film were observed only at film thickness above $\sim$ 10 nm and not observed for thinner films created with the original recipe can be understood by this critical thickness. Moreover, the relation between total strain energy and film thickness can explain why new line defects were created continuously while the deposition occurred. This phenomenon can be seen as the necessity for the thin film to accommodate the further strain accumulated during the layer-by-layer growth. A simple calculation yields for thickness dependence of the

dislocation line density:

$$\delta(h) = \frac{b}{S} = \frac{b}{4\pi h_c}\,\frac{h - h_c}{h_c}\,ln\left(\frac{h_c}{b}\right) \qquad , \tag{3.22}$$

assuming that $h_c \gg b$. That means that the line density is proportional to the thickness difference Δh = h - h_c.

In the following I discuss how the long range distortions of the crystal lattice induced by dislocations causes an atomic displacement at the thin film surface. Such distortions are well described by classical dislocation theory[70]. Suppose that a misfit dislocation is located at a distance d below the film surface. Its Burgers vector can be separated in three perpendicular components, (i) a screw component b_{screw} parallel to the dislocation line direction, (ii) an edge component $b_{\parallel}$ perpendicular to the screw one that lies in the surface plane and (iii) a component $b_{\perp}$ perpendicular to the surface plane. Chosen a coordinate system such that y is the growth direction and xz is the surface plane, with z parallel to the dislocation line direction, the atomic displacement vector $\mathbf{u}$ at the surface above the dislocation is given[71] by

$$\begin{aligned} u_x &= \frac{b_{\perp}}{\pi}\left(\frac{d^2}{d^2+x^2}\right) + \frac{b_{\parallel}}{\pi}\left(\frac{-dx}{d^2+x^2} + tan^{-1}\frac{x}{d}\right) \\ u_y &= \frac{b_{\perp}}{\pi}\left(\frac{dx}{d^2+x^2} + tan^{-1}\frac{x}{d}\right) + \frac{b_{\parallel}}{\pi}\left(\frac{d^2}{d^2+x^2}\right) \\ u_z &= -\frac{b_{screw}}{\pi}\,tan^{-1}\frac{x}{d} \end{aligned} \tag{3.23}$$

A model of the surface height function $h(\mathbf{R})$ for a sub-surface dislocation should retrace the height component of the surface displacement, i.e. u_y. Therefore, an initial surface with such function as $h(\mathbf{R})$ was implemented into the simulation code. The new inputs required were the Burgers vector modulus $|\mathbf{b}|$, its angles with the plane parallel to the surface and with the dislocation line, and the dislocation depth d.

3.1.5 Simulation results and proposed model

An example of the image input and output of the simulation code is presented in **Fig. 3.15**. In this case were simulated an atomic step (**Fig. 3.15a**, left) and a surface profile (right) caused by a dislocation with Burgers vector perpendicular to the surface and located 5 nm below the surface. **Fig. 3.15a** is the input image, in which the color gradient is proportional to the height value $h(\mathbf{R})$, together with the plot of the projection of $h(\mathbf{R})$ along the horizontal axis x. **Fig. 3.15b** is the resulting LEEM image, together with the intensity profile along the horizontal axis. Both images have a simulated size of 200x100 nm^2. The contrast aperture value was set to 30 μm and a magnification M = 18 was choosen. ΔE was 0.5 eV. Such values were kept constant for all simulations.

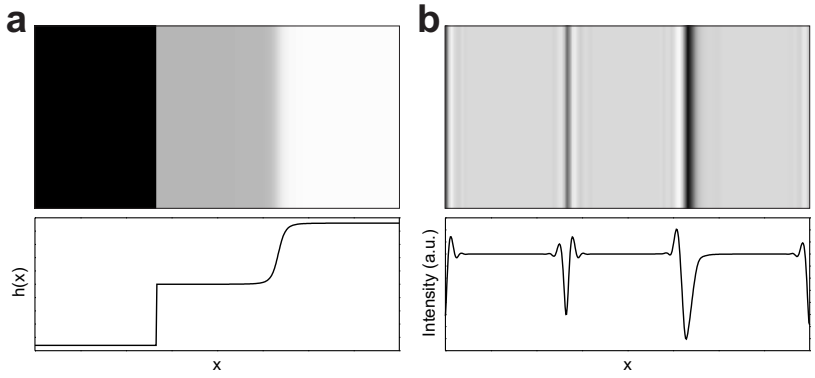

Figure 3.15: Example of simulation input (a) and output (b) images of an ideal atomic step and a sub-surface dislocation with Burgers vector perpendicular to the surface. The black and white values of the image intensity are -5%/105% of the value range, respectively. Linear scans of the images along the horizontal axis are presented below. Step height and Burgers vector module 2.3 Å, E_0 = 20 eV, d = 5 nm, Δf= 1 μm, C_s = 26 km, C_c = 32 m.

The LEEM image contrast of sub-surface dislocations was simulated and analyzed as function of the defocus, the start energy, the depth and the Burgers vector magnitude and angle with the surface plane. Two sets of simulations were taken for two different aberration regimes: one non-aberration-corrected (NAC), with C_s = 26 km and C_c = 32 m - the nominal values of the SMART lens system without the electrostatic mirror - and one almost perfectly aberration-corrected (AC) with C_s = 2.6 km and C_c = 3.2 m, i.e

10% of the NAC values, which should represent the experimental case. From **Fig. 3.15** it is already visible that a sub-surface dislocation with Burgers vector normal to the surface produces a kind of "smoothed" step. This configuration generates a highly asymmetric LEEM contrast, with one side bright and the other dark, very different respect to the contrast of an atomic step and similar to the contrast detected for the isolated line defects on a $Fe_3O_4(111)$ thin films. In the following we will discuss first this kind of dislocation as a candidate model for such defect.

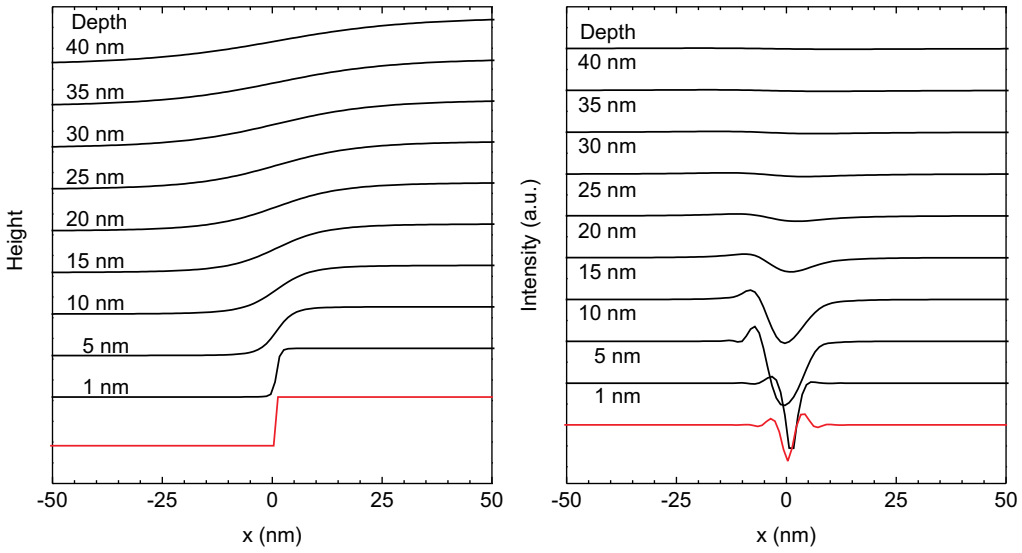

Figure 3.16: Real height and LEEM intensity of an atomic step (in red) and a sub-surface dislocation (in black) with different depth values. Step height and Burgers vector modulus 2.35 Å, E_0 = 20 eV, Δf = 1 μm, NAC.

The real profile of a normal dislocation depends on two parameters: the magnitude of the vertical component of the Burgers vector, which is the height difference between the two sides of the crystal, and the depth, which is proportional to how "smooth" is the profile. The latter effect is visible in **Fig. 3.16**, where line profiles of the real surface and NAC LEEM image are presented for different depth values (an ideal atomic step is presented for comparison in red). Dislocations with a depth above 20 nm and a Burgers vector modulus of 2.35 Å produce such a smooth height profile that is not visible in

LEEM. This value sets a upper threshold for the depth. It is important to notice that the asymmetry in the LEEM profile is produced for every depth value below this threshold.

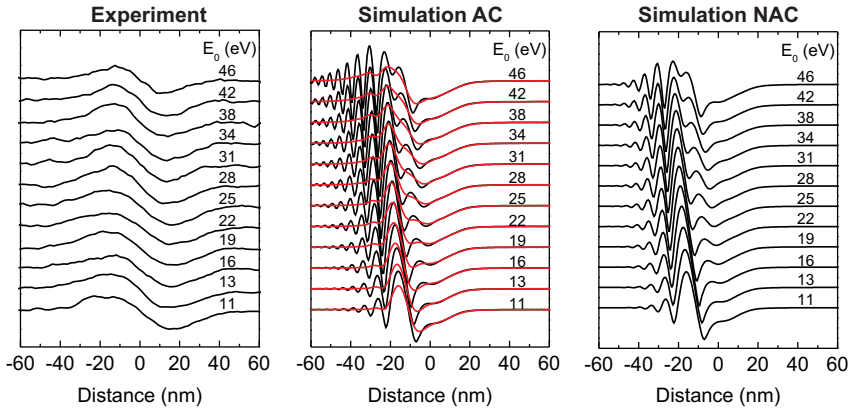

Figure 3.17: Experimental and simulated energy series for AC and NAC regimes. The red profiles in the AC series are produced with a Gaussian convolution of FWHM = 7 nm and simulate the detection with a resolution limit like in the experimental case. Burgers vector modulus 2.35 Å, Δf = 20 μm, depth 8 nm.

In Section 3.1.1 it has been shown that the isolated line defects behave differently in LEEM compared to a normal atomic step when the start energy is changed. Such effect is well reproduced by the simulations. The series of simulated line profiles for different E_0 in over-focus conditions are presented in **Fig. 3.17** in AC and NAC regimes, together with the experimental series already presented. In both cases the profile asymmetry is preserved by changing E_0. It is clear that the real superficial shape of the sub-surface dislocation influences deeply its appearance in LEEM. Here it should be underlined that the sense of the profile asymmetry indicates the real orientation of the dislocation: for any start energy, the brighter side in LEEM in over-focus conditions corresponds to the lower side in the real height profile. For the values of $|\mathbf{b}|$ and d chosen in this example (2.35 Å and 3 nm, respectively), the series presents visible diffraction fringes, which were not evident in the experiment. This can be due to a limit in the experimental resolution, influenced for example by small drift movement and physical resolution of the detector (due to the large field of view and the limited resolution, caused by the channelplate/screen unit): in fact, the spatial period of the fringes, 2-3 nm, is inferior than the maximum resolution for the field of view used in the experiment (3.11 μm),

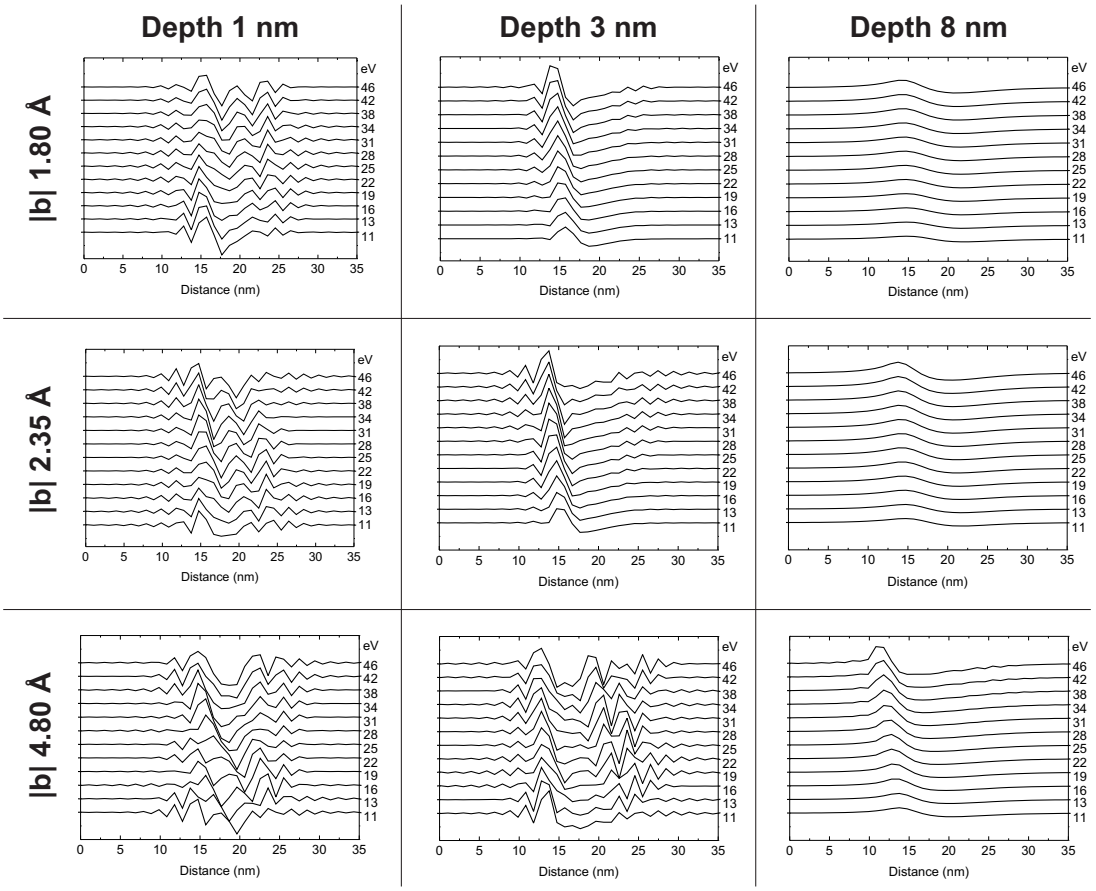

Figure 3.18: Energy series for different values of depth and Burgers vector magnitude in AC regime. $\Delta f = 1$ μm.

yielding a detector resolution of 7-8 nm. The low resolution has a broadening effect that can average out the diffraction fringes. This can be simulated as a convolution with a Gaussian function of FWHM equal to the resolution limit. The result can be seen in the AC simulation in **Fig. 3.17**: assuming a FWHM of 7 nm, the smoothed profiles (in red) present no fringes anymore. However, in the following the simulated profiles will be presented without smoothing.

Fig. 3.18 presents simulated energy series in AC conditions for three different values of $|\mathbf{b}|$ and d. From these data emerges that an asymmetric and smoothed LEEM profile is provided only if the depth is at least a few nanometers. Moreover, it seems that for a smooth LEEM profile is also crucial the ratio between $|\mathbf{b}|$ and d, i.e. the slope of the height profile. If $|\mathbf{b}|$ is below 2 Å, even a depth of 3 nm is enough to produce a LEEM profile without diffraction fringes. On the contrary, if $|\mathbf{b}|$ is 4.8 Å (equal to an atomic step on the Fe_3O_4(111) surface), a higher depth value is necessary to get rid of the fringes and have a smoothed profile. This gives a first indication that the dislocation should not be very close to the surface, and that the Burgers vector magnitude (or at least its normal component) should be smaller than the normal atomic step height.

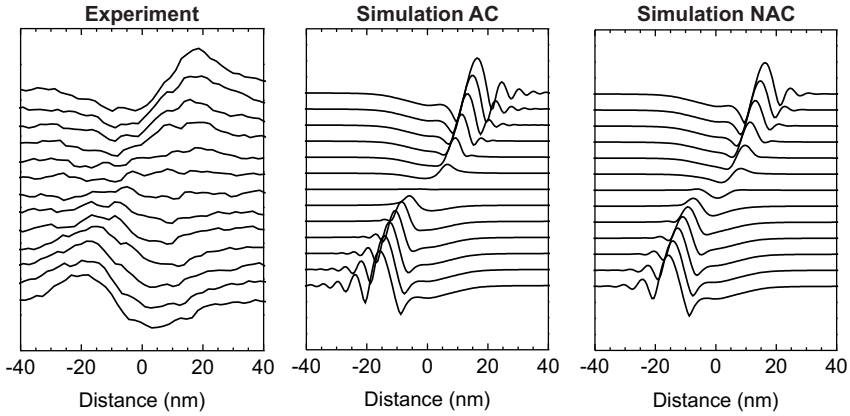

Figure 3.19: Experimental and simulated energy series for AC and NAC regimes. Focus range -15 μm / 15 μm, $|\mathbf{b}|$ = 2.35 Å, E_0 = 19 eV, d = 8 nm.

Another crucial parameter to compare is the focus. In **Fig. 3.19** are presented experimental and simulated focus series in AC and NAC conditions. As said previously, the profile asymmetry of the isolated line defects changes polarity with the focus, and in

perfect focus conditions no significant contrast is detected. In the simulations, only the AC results fulfill all requirements, while in the NAC case there is always a contrast, even in perfect focus conditions.

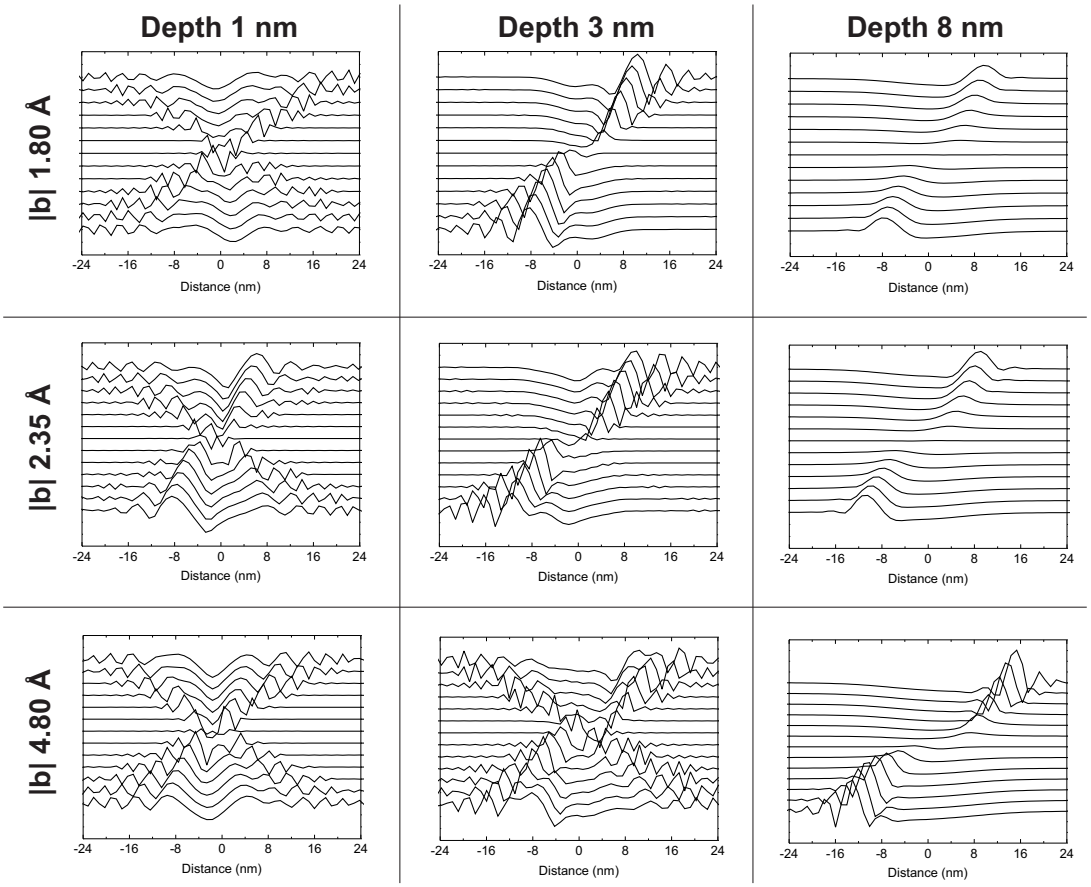

Figure 3.20: Focus series for different values of depth and Burgers vector magnitude in AC regime. Focus range -15 μm / 15 μm, E_0 = 20 eV.

Focus series were then simulated for three different values of $|\mathbf{b}|$ and d (**Fig. 3.20**). As in the energy series case, it is clear that a small depth value (a few nm) produces contrast profiles which are not compatible with experimental evidences, while a better agreement is reached with depth values above 3 nm. Even in this case the slope of the real profile seems to play a fundamental role. The ratio between $|\mathbf{b}|$ and d is more significative than the single values. In fact the results with $|\mathbf{b}|$ = 1.8 Å and small depth are almost equivalent to the ones with $|\mathbf{b}|$ = 4.8 Å and large depth.

A similar analysis can be done for misfit dislocations with a Burgers vectors parallel to the surface plane. An example of the simulation is shown in **Fig. 3.21**. In **Fig. 3.21a**, the input image and its horizontal line profile show the surface displacement that such type of dislocation can generate on the surface: a Lorentzian-shaped depression with amplitude $b_{\|}/\pi$ and FWHM proportional to the depth d. This displacement generates an over-focused AC LEEM image visible in **Fig. 3.21b**. The contrast profile of the defect shows a central dark band with two bright borders. This profile resembles significantly the one detected for the network lines. Therefore, this kind of defect is candidate as the origin of the line network.

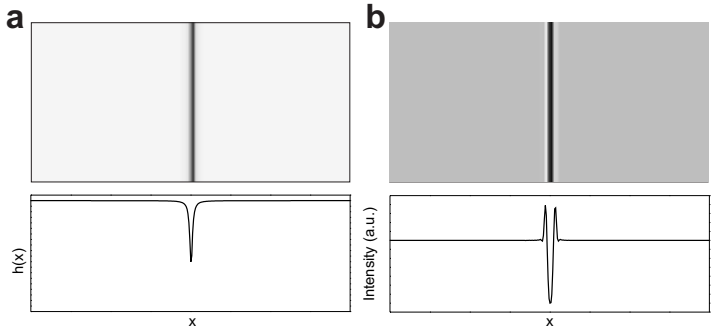

Figure 3.21: Example of simulation input (a) and output (b) images of a sub-surface dislocation with Burgers vector parallel to the surface. The black and white values of the image intensity are -5%/105% of the value range, respectively. Linear scans of the images along the horizontal axis are presented below. $|\mathrm{b}|$ = 1.8 Å, E_0 = 20 eV, d = 1 nm, Δf = 1 μm, AC.

The full comparison between experimental results (from **Fig. 3.12**) and AC simulations is presented in **Fig. 3.22**. The simulations show a clear agreement in the LEEM appearance for different focus values. The depth value was set to 10 nm, which is the film thickness in the experimental case: in this case the simulated misfit dislocation occurs at the interface between the Fe_3O_4(111) thin film and the Pt(111) substrate. Simulations are also useful to predict the behavior of such defects for different start energy and defocus values (**Fig. 3.23**). The series shows that the contrast does not change with the energy, and that only a change in the defocus value is able to invert the polarity of the profile. Moreover, no appreciable difference was detectable between AC and NAC regimes, and for different values of the Burgers vector modulus: like in the previous

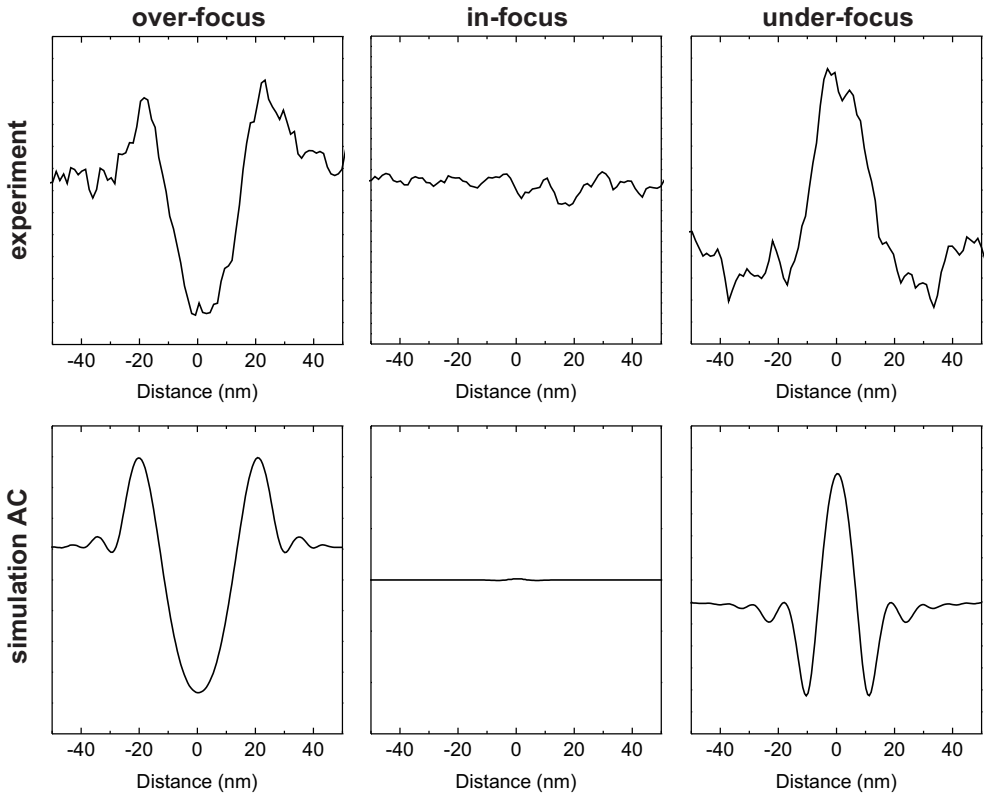

Figure 3.22: Comparison between experimental (top) and simulated (bottom) LEEM contrast profiles of line defects created by misfit dislocations with parallel orientation of the Burgers vector. The relative intensity scale is constant. Focus values 30 μm (left), 0 μm (center) and -30 μm (right). $|\mathbf{b}|$ = 1.5 Å, E_0 = 29 eV, d = 10 nm.

case, the contrast vanishes for depths above $\sim$ 20 nm.

3.1.6 Discussion

The simulation of LEEM images via CTF formalism proved itself a very valuable tool for unveiling the physical nature of the isolated line defects and the line network. The qualitative comparison between simulation and experimental data allows developing a model for such defects: the isolated line defects are most likely dislocations with a predominant vertical component of the Burgers vector, while the line network is a system of misfit dislocations with a Burgers vector parallel to the surface plane. Both crystal-

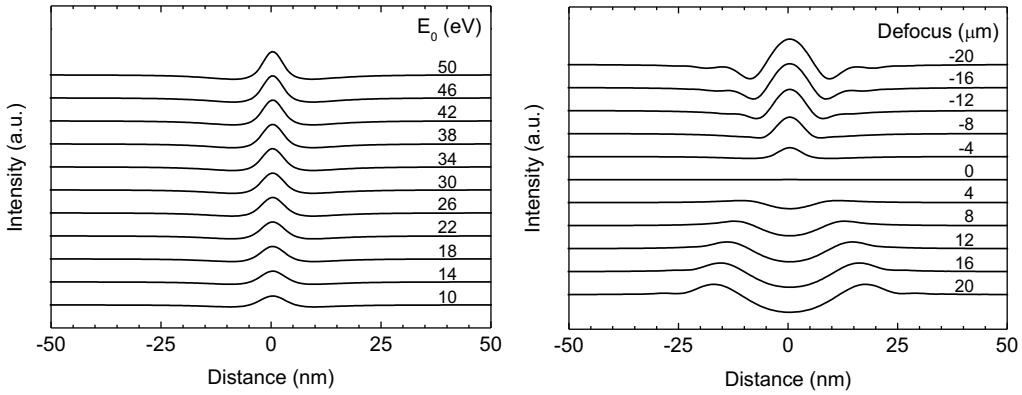

Figure 3.23: Simulated energy (left) and focus (right) series of LEEM contrast profiles of sub-surface misfit dislocations with parallel orientation of the Burgers vector. A focus of 1 μm was set in the energy series, while the focus series was performed with E_0 = 29 eV. $|\mathbf{b}|$ = 2 Å, d = 10 nm.

lization defects occur inside the thin film or even at the interface film/substrate, whereas the related strain field generates a surface deformation; such displacement produces a peculiar contrast in LEEM, very different from the usual atomic step and can be easily recognized.

As is generally known, magnetite thin films produces several kinds of crystallographic defects: for example, misfit dislocations were found in magnetite films epitaxially grown on $SrTiO_3(001)$[72] and $MgAl_2O_4(001)$[73]. Moreover, other defects such the antiphase domain boundaries (APBs) were observed. The antiphase domains are regions of a crystal in which the atomic positions of one domain can be transformed into the atomic positions of the other by a translational operation which does not belong to the space group of the crystal. The boundary between these domains is a plane in which the atoms have a special geometrical configuration that differs from the usual one in the crystal. Such APBs can be formed mainly by two processes. The first is the merging of growing domains with equivalent nucleation sites on the substrate separated by non-translational vectors of the film lattice. In the second, their formation can be attributed to the generation of misfit dislocations[73]. In fact, the strain field created by a misfit dis-

location can generate a glide process of the film above the same dislocation. If the glide shift, which is the strength of the dislocation, is only a fraction of the unit cell size, an APB can be generated. The glide plane can in principle spread through a part or even the entire film thickness, reaching the surface and generating protrusions or special steps[71]. APBs on magnetite thin films have been extensively studied in the past[48,74–82], mainly with dark field TEM, which gives information about the bulk structure. Less is known about their intersection with the surface: only APBs at the Fe_3O_4(001) surface were investigated with STM[83]. APBs in magnetite thin films have attracted the attention of the scientific community due to their influence on the electromagnetic properties. They are in fact responsible for an enlargement of the saturation field[74] and an increase in resistivity[76]. The local configuration of the atoms in an APB can deeply influence the band structure and the superexchange that are responsible for the general electromagnetic properties of the magnetite, such as the half metallicity and the ferromagnetism. Moreover, this aspect is also very important for the catalytic properties of the surface; it is generally accepted that, for transition metal oxides, crystallization defects such as APBs and rotational domain boundaries are a preferential adsorption site for molecules, an important diffusion channel for deposited atoms and a nucleation center for metal nanoparticles[83–86].

In Fe_3O_4(111) thin films, APBs were found with a shift of 1.86 Å and 2.35 Å, i.e. 3/8 and 1/2 unit cell, along the [111] direction[48] (see **Fig. 3.24**). The atomic model of the antiphase boundary (APB) shows that for the first shift the Kagomé plane in one domain corresponds to one of the tetrahedrally-coordinated Fe atoms in the MixTrigonal plane of the other domain, while the second shift is compatible with a switch between the two kind of iron planes, with a conservation of the oxygen planes. HRTEM did not provide information about the kind of surface step that can be generated by such APBs and if the boundaries crossed the entire film thickness, from the substrate interface to the surface. This glide plane can be crucial for the understanding of the motion of the isolated line defects during the deposition.

LEEM simulations have shown that the contrast profile is compatible with the surface distortion generated by dislocations located at least 3 nm below the surface. This result seems to be in contradiction with the fact that isolated line defects could flow like normal steps during the Fe deposition in oxidation conditions. In fact, in the first model, no

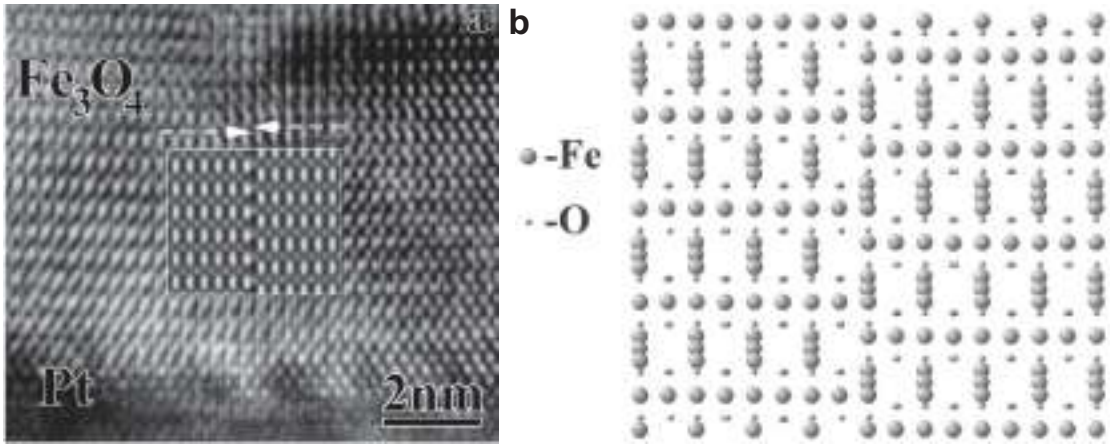

Figure 3.24: HRTEM cross-section image of an APB with a shift of 1.86 Å along the [111] direction. In the inset a simulated image is shown. (b) Projection of the corresponding atomic model of the APB along [$\underline{1}12$]. From Ref. 48.

surface discontinuity is taken into account, but only a smooth and gradual distortion of the lattice above the dislocations. Furthermore, it has to be taken into account that only the isolated line defects moved, while the line network remained still, and that such movement was a consequence only of the Fe deposition and not of the high temperature. This deadlock can be overcome with a particular model of the dislocations with vertical Burgers vectors (**Fig. 3.25a**). In this model the dislocation line does not necessary lie on the film/substrate interface, but could be at the top of a glide plane (in the figure, for simplicity, the shift and the Burgers vector are half unit cell along the [111] direction). The dislocation line is covered by the film like a carpet; in this part the lattice is distorted over the dislocations in agreement with the LEEM simulation model. On the other hand, the line network can be modeled as a system of line dislocation on the film/substrate interface with a Burgers vector parallel to the interface plane (**Fig. 3.25b**). The lattice distortion, different from the other case, is responsible for the particular LEEM contrast of the network.

The model presented for the isolated line defects can explain the growth process, by admitting that the deposited material (Fe and O atoms) can segregate through the film and reach the dislocation line. This kind of film growth, which is complementary to the normal step flowing, can be articulated in four stages (**Fig. 3.26**).

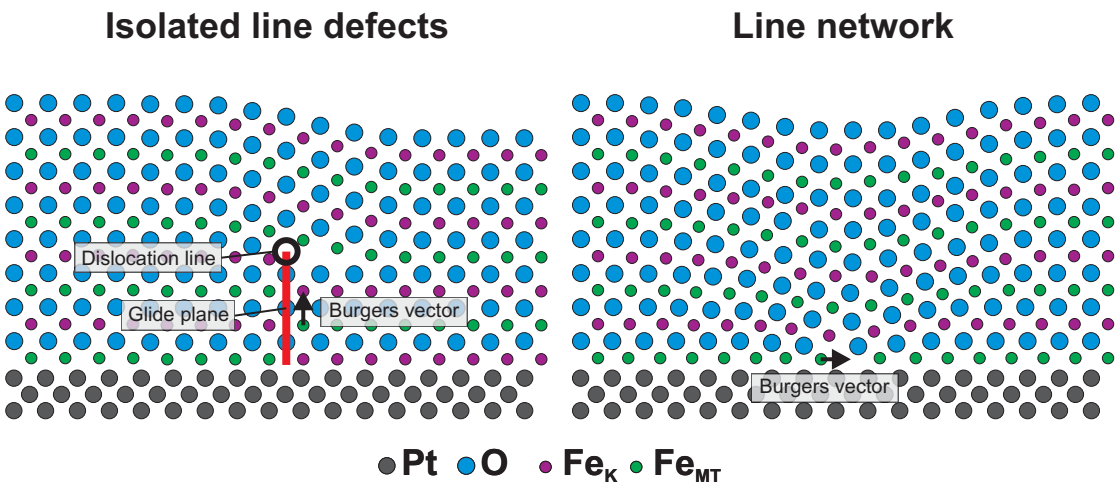

Figure 3.25: Simplified side view of the atomic models for the isolated line defects and the line network. The dislocation line and the glide plane are perpendicular to the side view. In both cases the dislocation strength is half unit cell.

1. The film surface is covered by Fe and O atoms;

2. Due to the high temperature and the lattice distortion above the dislocation line, the Fe and O atoms can segregate into the film and reach the locus of the dislocation;

3. The new atoms crystallize with the lattice geometry of the ”carpet” that cover the dislocation and induce eventually a rearrangement of the atoms underneath (in the case depicted, it is necessary only to shift Fe atoms from octahedral to tetrahedral site and vice versa);

4. The dislocation and the eventual glide plane underneath result shifted.

The proposed model can explain every feature seen in the experiment for the isolated line defects. The line moves only when Fe atoms are deposited and stops moving when the deposition is interrupted. The dislocation differs topologically from an atomic step, so that an atomic step can flow through the dislocation line like on a wave. On one hand, two dislocations with the same Burgers vector but opposite growth direction can annihilate each other. On the other hand, two dislocations with the same Burgers vector and same growth direction cannot annihilate, but only if the sum of the Burgers vector is not

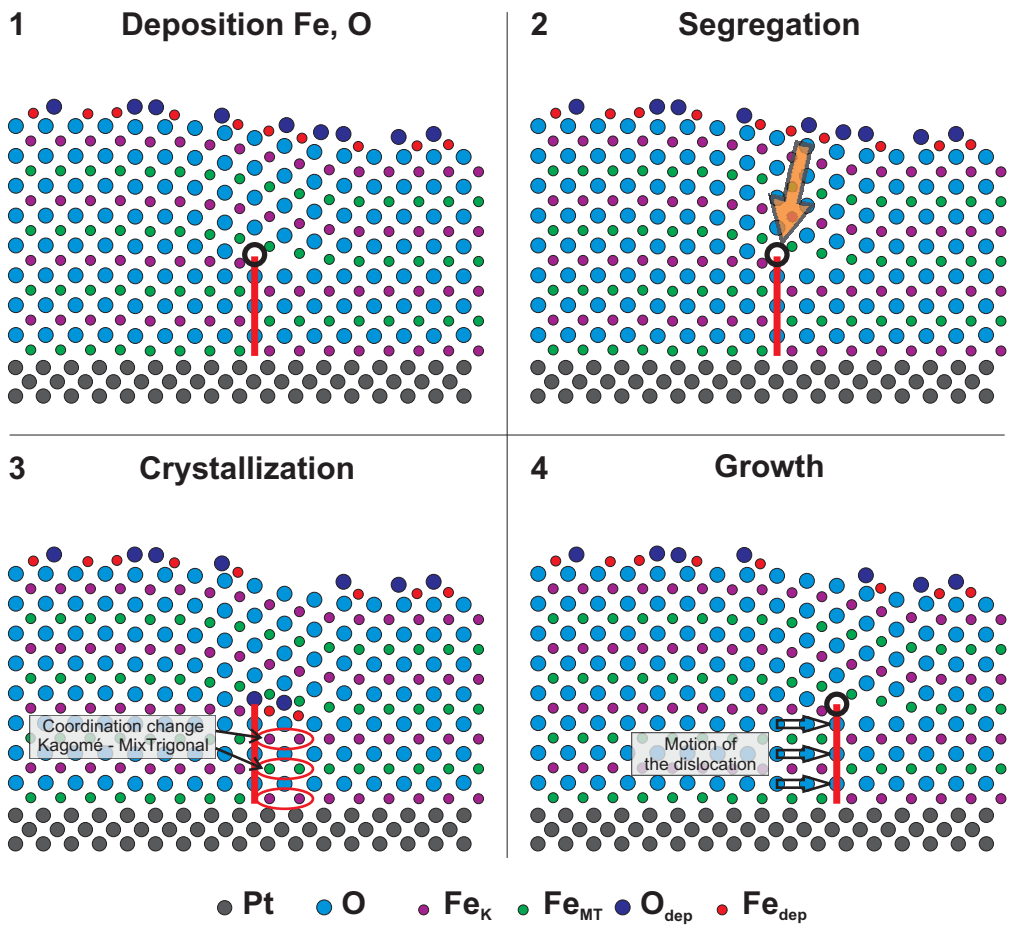

Figure 3.26: Model of the dislocation propagation during the thin film growth. The four stages are discussed in the text.

equal to a translation vector of the film lattice (otherwise they generate a normal step). The passage of a vertical dislocation line that lies on the film/substrate interface, or a glide plane that intersect the interface, can impose a rearrangement at the atomic level of a dislocation line with horizontal Burgers vector, with a sort of ”cancellation” and ”regeneration” process of the misfit dislocation in another area of the film. The constant creation of new isolated line defects can be seen as a sub-surface fracture of the film close to the substrate interface and the creation of a glide plane that goes through part of the film in order to accommodate the strain energy accumulated during the growth.

In conclusion, with the conjugation of *in-situ* and real-time LEEM observation and computer simulation via CTF formalism, a consistent model of the different types of crys-

tallization defects in the $Fe_3O_4(111)$ thin film was built. Such model explain in detail what turns to be a new growth channel for the $Fe_3O_4(111)$ thin film, which can be of great help for the explanation of the processes that govern the thin film properties.

3.2 Rotational domains

Another relevant aspect that could be investigated during the layer-by-layer growth process was the formation and evolution of the rotational domains. In general, rotational domain boundaries (RDBs) are very similar to the already discussed APBs: while antiphase domains transform into each other by a translational operation, rotational domains transform into each other by a point symmetry operation. It has been already pointed out that RDBs have great importance in the study of the catalytical properties of the oxide thin film. As pointed out in Section 2.2.1, $Fe_3O_4(111)$ grown on a Pt(111) surface presents two twin domains rotated against each other by 180°, with non-identical surface coverage. The predominance of one of the rotational domains ranges from 75%/25% to 98%/2%. The size of the domains often exceeds the size of the terraces produced with the standard recipe. This peculiar lack of RDBs can in principle indicate an anomalous electric and magnetic behavior, like in the case of APBs. In general, the RDBs are an intrinsic consequence of the nucleation and growth mechanism on the film on a certain substrate. In first analysis, it can be related to the energy required to produce a stacking fault during the pristine formation of the magnetite film respect to the fcc stacking sequence of the substrate (i.e. ABCBAC instead of ABCABC). It has been shown that the predominance of one rotational domain is preserved after further deposition cycles; this demonstrates that the asymmetry is generated in the pristine creation of the magnetite film. In the initial phase, the iron deposited on the FeO(111) layer forms $Fe_3O_4(111)$ islands that coalesce into a closed film. The orientation of the domains is therefore a consequence of the orientation of the initial islands. In this sense, the substrate could play a crucial role, not only for the energy to form a stacking fault during the pristine magnetite growth, but also for inducing stacking faults by substrate step bunches, especially the step direction may prefer one of the different stacking faults. In order to analyze this phenomenon, it is necessary to study in detail the thin film growth in every stage.

3.2.1 Interplay film/substrate

The role of the substrate for the formation of the antiphase domains is already indicated in the experiment described at the beginning of this Chapter, in which triangular Fe_3O_4 islands grown in layer-by-layer mode on a closed FeO(111)/Pt(111) film exhibit a preferential orientation with a ratio 75%-25% (**Fig. 3.1**). This is a confirmation that the stacking fault is produced mainly at the film/substrate interface. However, a more careful analysis at this stage can reveal more details about the interplay between film and substrate, with particular attention on the substrate morphology. The layer-by-layer growth created a relatively small number of magnetite islands because of the high temperature and the slow deposition rate. These conditions enabled the migration of the deposited material and favored the enlargement of the existing island compared to the creation of new ones. With this technique, it was possible to control in the finest way the thickness of the islands, but at the price that the substrate surface was not covered uniformly. On the contrary, the original recipe, with separate stages of Fe deposition at room temperature and subsequent annealing in an oxygen environment, led to higher density of smaller Fe_3O_4 islands, which were more uniformly distributed on all surface features of the substrate. Therefore, for this analysis the standard technique is preferred to form the islands, even if this does not permit a complete control over the thickness. **Fig. 3.27a** shows the final result of the oxidation of 3 ML of Fe deposited at room temperature on a closed FeO(111) single layer. Several hundreds of isolated Fe_3O_4 islands (in white) were formed by the ubiquitous crystallization of iron and oxygen in a field of view of 12.4 μm. Whereas the islands grown on large substrate terraces had mainly a regular polygonal shape (triangular or hexagonal), the ones decorating substrate step bunches were more irregular. The largest islands were about 500 nm wide, while the majority was about 200 nm. Beside these Fe_3O_4 islands, other islands with similar shape and size (in dark) populated the substrate terraces. Their nature will be clarified afterwards. Dark field images (**Fig. 3.27c** and **d**) exhibit that the (in plane) crystal orientation of the magnetite islands was strongly influenced by the substrate morphology. The two possible configurations were almost perfectly separated: one type existed only on the terraces, while the other on the step bunches. Clearly, the substrate steps induced a preferred stacking order in the epitaxial growth of Fe_3O_4, while on flat terraces this did not occur easily. Surprisingly, there is no indication that the orientation of the sub-

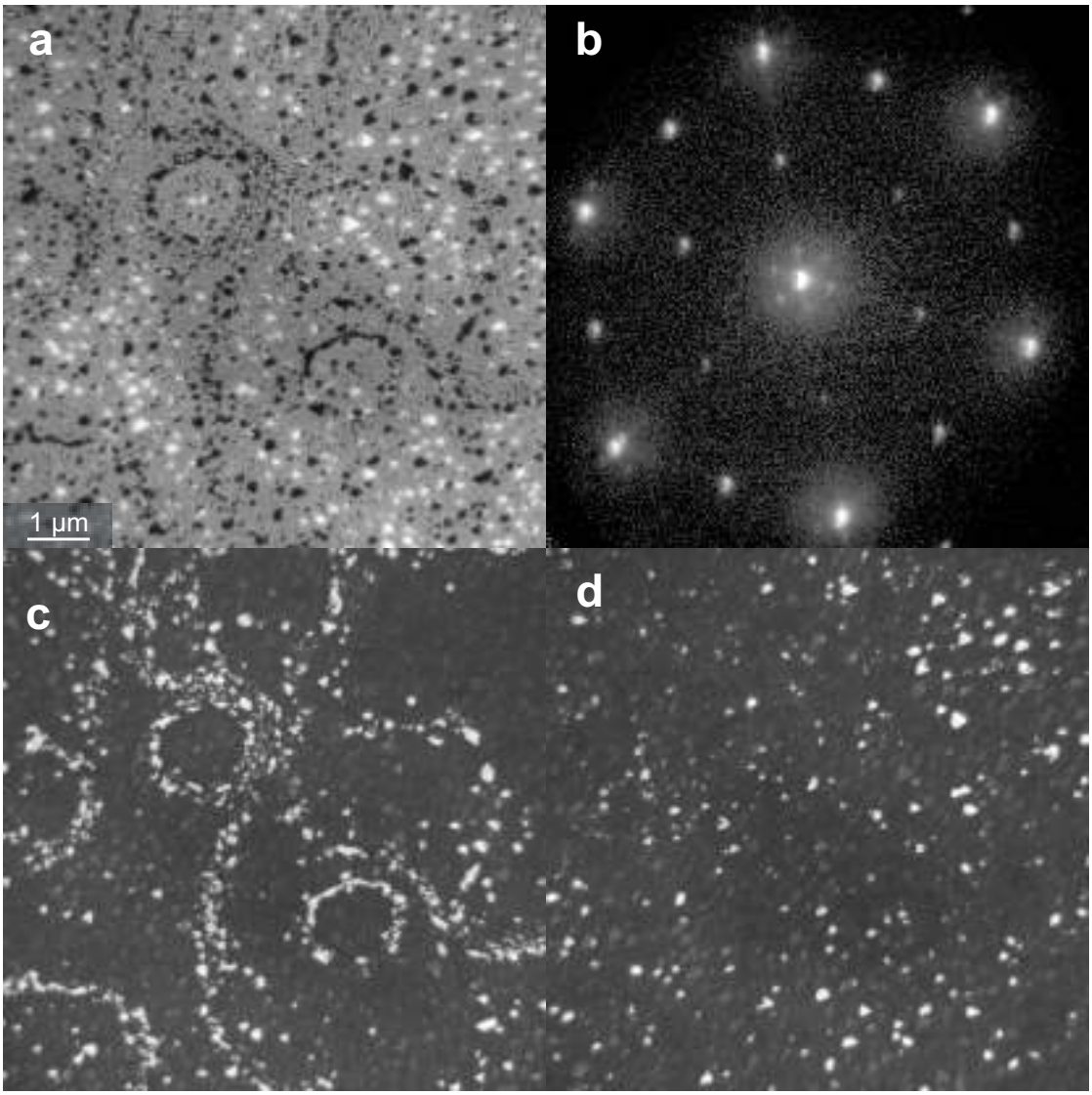

Figure 3.27: Distribution of the Fe_3O_4 islands grown with different stacking sequence over a FeO/Pt(111) thin film. (a) bright field image of the (monolayer) FeO surface (in gray) with thicker FeO_x islands (in white) and Fe_3O_4 islands (in black). E_0 = 24 eV. (b) LEED pattern of this surface area; the FeO extra spots are visible around the central (0;0) spot, as well as the ones for a normally-terminated Fe_3O_4. E_0 = 39 eV. (c) and (d) Dark field images of the surface using the (1/2;0) and the adjacent (0;1/2) spot, respectively. The substrate atomic steps (the wavy and circular structures) are decorated by Fe_3O_4 islands with only one orientation.

strate step made a whatsoever effect; the magnetite islands with stacking fault decorated almost uniformly the steps of the circular protrusions that characterized the substrate morphology, with no visible orientation preference. It is important to notice, also, that all the Fe_3O_4 islands consisted of one single rotational domain, i.e. no islands with RDBs were detected. At this stage, therefore, the orientation of the triangular island shape was a good benchmark for deducing their stacking sequence even without dark field techniques.

In addition, dark field LEEM and LEED images (**Fig. 3.27b**) permit to characterize the islands populating the substrate terraces and which appear dark in bright field. In dark field using the half-order Fe_3O_4 diffraction spots, they were not detected; this excludes the possibility of Fe_3O_4 with canonical termination. Furthermore, the local LEED images excluded that they were made by Fe_3O_4 terminating with the "biphase". Therefore, the only remaining possibility is that the islands consist of FeO_x agglomerates. The coexistence of Fe_3O_4 and FeO_x islands with same shape and size, on the same substrate, might indicate that the Fe_3O_4 is created by re-crystallization of such FeO_x agglomerates, i.e. the FeO_x islands are the precursors of the Fe_3O_4 islands. The formation of metastable FeO_x seems to be a necessary step in the process that leads from a single layer of FeO to a thick Fe_3O_4 film.

3.2.2 Dynamic evolution for increasing thickness

With the standard recipe, the thicker Fe_3O_4 thin film closes by coalescence of islands. If some of the islands crystallize with a stacking fault, antiphase boundaries will be created between these and other islands with proper stacking sequence. The evolution of the shape of the RDBs is driven by the minimization process of the configurational energy of the atoms at the boundaries, usually expressed in energy per surface unit. The RDBs are then high-energy areas, and the minimization process reduces the system energy by rearrangement of the atoms in a more energetically favored spatial configuration; their relative movement can be activated not only with high temperatures, but also with changes in the chemical potential or stimulation by electromagnetic fields. In order to study these aspects, the dynamic evolution of the RDBs during the growth was observed in real-time during the layer-by-layer deposition.

A completely closed, 7 nm thick Fe_3O_4(111) thin film was grown on Pt(111) with the standard recipe. In the following, this template was exposed to 1x10^{-6} mbar of O_2 and kept at 1000 K. The dark field mode using the (1/2;0) diffraction spot visualize the contrast between the twin kinds of domains. The initial sample surface exhibited a predominance of one rotational domain, with a ratio 79%-21%. In the following, the deposition of 9 ML of Fe was observed with a sampling rate of one image per second (**Fig. 3.28**). The images show clearly a gradual change of the shape of the domains, i.e. a rearrangement of the domain boundaries. Small domains (up to 300 nm large) gradually shrank in size and eventually disappear, while large domains assumed a more regular, hexagonal shape. When the Fe deposition was interrupted, the entire system froze. Therefore, this change was an exclusive consequence of the Fe deposition in oxidation conditions, and was not driven simply by the high temperature of the sample. From the observation in dark field and bright field mode of the surface features (RDBs, atomic steps and dislocations) during the layer-by-layer growth, it emerges that the motion of the RDB was not influenced by the flow of the atomic steps or the dislocations. The rotational domain boundaries were stable at the flow of a new layer, and dislocations could be created equally in both twin domains. This indicates that in the case of magnetite, when a new layer is formed on a RDB, the influence of the template underneath is stronger than the template on the side, i.e. it is more energetically convenient to create a RDB in the new layer than move the RDB by rearrangement of the atoms underneath. This mechanism is not valid universally, but depends on the very system. In other cases, such as Ag films on Ru(0001)[87], the opposite behavior was observed: during the film growth the step edges can move the twin boundaries. In the homoepitaxial growth of Ir(111)[88] the conversion of stacking-fault islands is thermally activated, and not stimulated by the step flow. The different behaviors can be ascribed to different structure of the RDBs, such as the nature of the bonds and the geometry of the atoms in the compound.

3.2.3 Discussion

The direct observation of the different growth stages of Fe_3O_4(111) thin films allows to clarify the mechanism beyond the formation and the evolution of the rotational domains

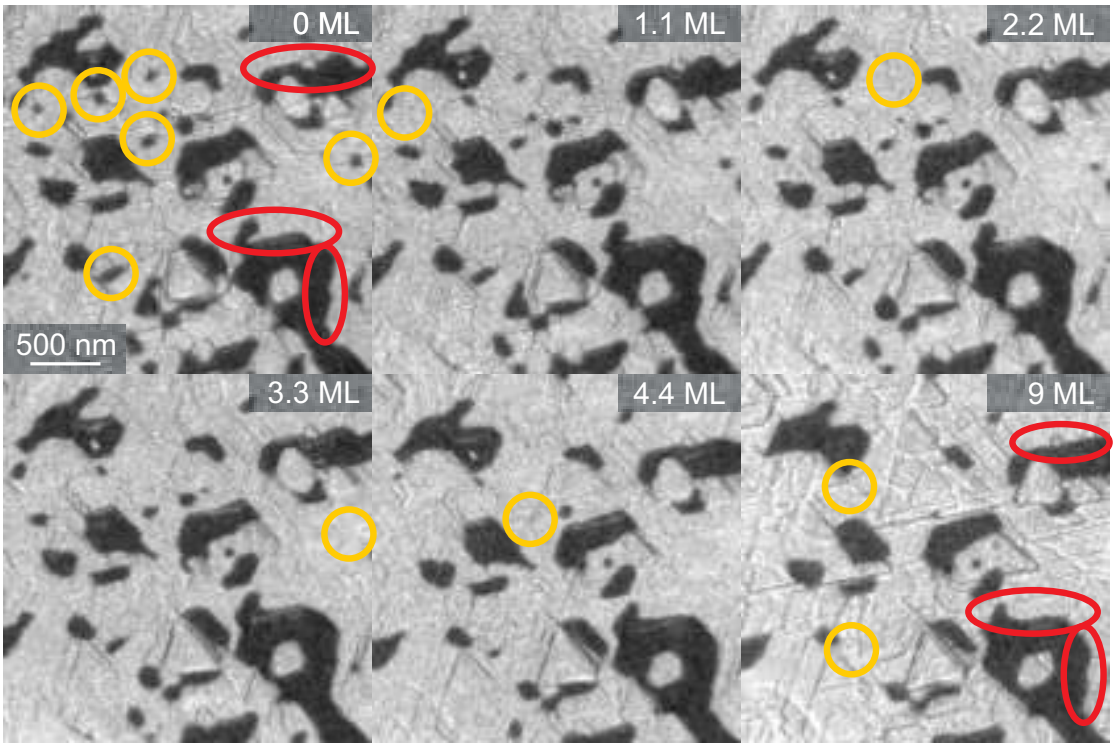

Figure 3.28: Dynamic evolution of the RDBs during Fe deposition in oxidation conditions. Small rotational domains (in yellow) shrank in size and disappeared, while the boundaries large rotational domains (in red) assumed a more regular form. E_0 = 24 eV, deposition rate 0.22 ML/min.

during the growth. The analysis of the relative coverage of the twin domains when the substrate is only partially covered by magnetite islands showed that the substrate morphology played a key role: the substrate step bunches and terraces seemed to trigger the stacking sequence of the magnetite. The fact that the majority of $Fe_3O_4(111)$ islands nucleated on the substrate terraces with one preferential direction could indicate that, in absence of steps, the fcc stacking sequence of Pt(111) is preserved in the stacking sequence of the magnetite oxygen planes. At this point it should be remembered that the Fe and O deposited on the substrate do not form directly magnetite islands, but first compose a $FeO_x(111)$ film. Such film forms a Moiré pattern with the Pt(111) surface; this means that in the unit cell of the 2D superlattice, both film/interface stacking sequence fcc and hcp are present (**Fig. 3.29a**). Therefore, the creation of the structural coherence

in the magnetite island should be a conversion process $FeO_x(111) \longrightarrow Fe_3O_4(111)$ that starts from a localized area in which the stacking sequence is preserved, and then propagates laterally through the island (**Fig. 3.29b** and **c**). This kind of mechanism could in principle work in the opposite way when a substrate atomic step is present. The experiment evidenced that magnetite islands formed on step bunches have the opposite stacking sequence. This could be explained by assuming that for a $FeO_x(111)$ film that covers a substrate step the $Fe_3O_4(111)$ conversion process starts from an area in which the stacking sequence has a fault. Unfortunately, the process described by this model happens in a scale beyond the resolution limits of SMART; a real confirmation (or a confutation) can be obtained only with investigation techniques that reach the atomic resolution, such as STM and AFM.

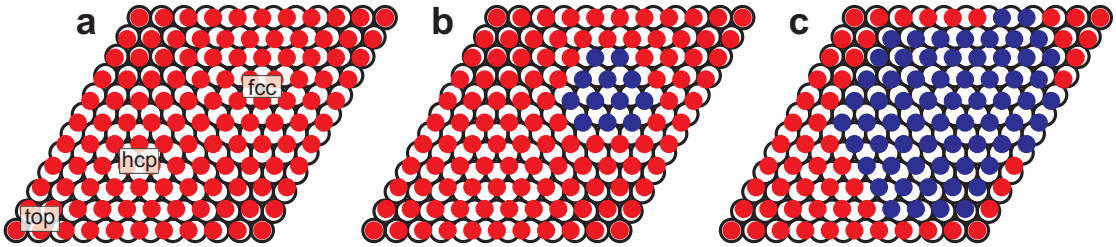

Figure 3.29: Sample scheme of the stacking configuration along the [111] direction in a Moiré pattern where 12 atoms of the substrate with fcc stacking correspond to 11 atoms of the adlayer. (a) areas with top, fcc and hcp stacking sequence. A film conversion might start from fcc areas (b) and propagate through the film (c).

The real-time observation of the $Fe_3O_4(111)$ RDBs during the layer-by-layer growth showed that such boundaries can change shape and length. The re-shaping of the RDBs for large domain is driven by the minimization of the total free energy, identical to the Wulff construction in the shape of crystals. In principle, the interface energy per unit length should depend on the orientation of the RDB. Experimentally it has been found that the domains shape tended to be hexagonal. The six orientations, due to the 120° symmetry of the single domain and the 180° symmetry between domains, should have the same density of free energy. Other configurations, i.e. different orientations, kinks and other corrugations should have a higher free energy. For large domains, it is reasonable to suppose that the volume within the RDBs might be treated as constant during the rearrangement. With these hypotheses, the Wulff rule is valid and a rotational

domain is forced to minimize its free energy modifying its shape. On the other hand, the total conversion of small domains could be consequence of the high surface/volume ratio. Their disappearance could be interpreted as a situation in which the domains are not big enough to survive at the settlement movement of the RDBs, i.e. the entire material with a different stacking is converted in the attempt to stabilize the RDBs, which have a higher density of kinks and other borders with high-energy configurations due to the small volume. In the conversion process, a crucial factor seems to be the deposition of Fe: only when the deposition occurred the RDBs were able to move. This phenomenon might be explained by the fact that RDBs are a preferential diffusion channel for the atoms deposited on the surface. Due to the high temperature, the Fe atoms can migrate through the RDBs and modify the local thermodynamic potentials in the RDBs; the newly introduced material changes the local chemical potential and could facilitate the rearrangement of the atoms in the boundary.

Chapter 4

Pt nanoparticles on Fe_3O_4/Pt(111)

Despite its specificity, metal deposits on oxides have wide and surprising applications over the centuries, e.g. from the manufacture of colored glasses in the rose window of medieval cathedrals to the information storage in magnetic discs[89]. Nowadays, metal/oxide heterojunctions are an active research field in material science, microelectronics and chemical applications[90]. In heterogeneous catalysis, many catalytic devices consist of nanosized metal catalysts supported on oxide films. As often shown[84,89], their activity critically depends not only on the composition, size and morphology of the metal particles, but also on the support itself, and, more noteworthy, on the interplay between them. The physical and chemical properties of such systems are not the sum of the properties of the separated components. The so-called *metal-support interaction* is of great importance in heterogeneous catalysis, though its origin is poorly understood in most cases. For oxidation reactions, for example, many different oxygen species may be present under reaction conditions: chemisorbed oxygen, sub-surface oxygen, interface oxide, surface oxide and bulk oxide (see e.g. Ref. 91 and references therein). Particular case is the so-called *strong metal-support interaction* (SMSI), which was first suggested by Tauster *et al.*[92–94] as an explanation for the decreased chemisorptions of CO and H_2 on transition metal particles supported on TiO_2. The systematic study of such phenomena involving metal-oxide model catalyst is of great importance for understanding the nature of the catalytic processes in real reactors. A more detailed knowledge on these topics may lead to a meditate design of a catalyst with improved selectivity for a desired chemical reaction.

In the following, the physical quantities that play a role in SMSI are briefly described

to give a general idea of the nature of this phenomenon. Two major factors contribute to the SMSI states: the perturbation of the electronic structure of the metal particles, originated by the charge transfer between metal and oxide, and the encapsulation (decoration) of the metal particles by a thin layer of reduced oxide. The latter is explained by Knözinger and Taglauer[95] in terms of wetting and spreading. In general, the thermodynamic conditions for wetting of a solid by a liquid can be expressed by the Young equation,

$$\gamma_{metal}\, cos\theta = \gamma_{oxide} - \gamma_{interface} \tag{4.1}$$

where θ is the contact angle between oxide support and metal adlayer (forming a "drop like" island) and γ denotes the specific surface free energy. The complete wetting occurs when θ approaches zero, i.e. when γ_{oxide} is greater than γ_{metal} + $\gamma_{interface}$. Combining this with the expression of the interface free energy,

$$\gamma_{interface} = \gamma_{metal} + \gamma_{oxide} - U_{interface} \tag{4.2}$$

with $U_{interface}$ indicating the work of adhesion, it results that in case of wetting

$$U_{interface} > 2\gamma_{metal} \tag{4.3}$$

The driving force for the encapsulation is therefore the surface energy. The encapsulation can be seen as a spreading effect of the support. For oxides in which γ_{oxide} values are relatively low, such in case of titania, vanadia, ceria and niobia, the ratio $U_{interface}/2\gamma_{metal}$ increases and SMSI can be observed. On the contrary, due to the higher surface energy, no SMSI can be usually found in silica, alumina, zirconia and magnesia. The enlargement of the interaction energy $U_{interface}$ can also enhance the encapsulation, for example with the reduction of the strain. This thermodynamic approach explains well the encapsulation conditions: in the interface between metal and oxide, the gradient of the surface free energy points towards the metal surface, and can have enough intensity to enable the migration of oxide molecules across the metal surface.

SMSI phenomena have been reported in magnetite-based systems very recently. In

2008 Shaikhutdinov and co-workers reported strong evidences for the encapsulation by a FeO monolayer of Pt particles supported on $Fe_3O_4(111)$ films[38]. The Pt nanoparticles (PtNP) were created via Pt deposition in UHV at room temperature and subsequent annealing to 850 K. Combined STM and CO TPD results provided direct evidence of the particle encapsulation, once the annealing occurred: STM showed that, after the annealing, the top facets of the largest Pt particles presented a Moiré superstructure with $\sim$ 25 Å periodicity, similar to the one found for FeO(111) monolayer film on Pt(111). CO TPD spectra presented a dramatic reduction of the CO uptake after the annealing; such reduction is much larger than the one expected for the nanoparticle sintering, and is explained in terms of SMSI. Further works explained more in detail the nucleation and the growth of Pt nanoparticles, and the behavior of the CO uptake in function of the particle thickness[96], as well as the CO adsorption and dissociation[97]. The Pt encapsulation by FeO showed also interesting catalytical properties in the low temperature CO oxidation[98] such reaction presented rate enhancement respect to the pure Pt case. The mechanism is an oxygen-induced transformation from Fe-O bilayer to O-Fe-O trilayer that catalyzes CO oxidation, in analogy with CO oxidation for FeO(111) thin film on a Pt(111) surface[99].

Furthermore, Pt on $Fe_3O_4(111)$ is a good example of a nanostructured model catalyst: the variety of phenomena which are involved in its formation and during a catalytic reaction makes this system worthy of further investigations, for a deeper understanding of the interplay mechanisms between metal nanoparticles and oxide support. In this sense SMART, offer a matchless possibility, the observation in real-time of the surface while the formation processes occur, from deposition to encapsulation. In principle, with SMART it would be possible to observe the behavior of a *single* nanoparticle in different conditions and with several investigation tools (microscopy, spectroscopy and diffraction) that can provide full control over the morphology and direct detection of the effects of the metal-substrate interaction. However, such analysis is a very challenging task, because it requires the best resolution performances SMART can achieve.

4.1 Pt deposition and calibration

The Pt deposition was performed by another Focus EFM3 evaporator, identical to the one used for the Fe deposition and mounted in the main chamber with equivalent position. Pt was evaporated from a rod of 99.99% purity. The deposition rate was calibrated by homoepitaxy on clean Pt(111) surface directly observed in LEEM. It is well known[100–102] that the Pt growth mechanism on Pt(111) depends on the temperature. Above 500 K the deposited Pt forms well ordered 2D islands that coalesce together in a layer-by-layer mode. Between 500 and 300 K, a transition to 3D island growth occurs. For even lower deposition temperatures, the growth mode change again, with the reentrance of layer-by-layer mode. This re-entrant mode is due to the dendritic form of the 2D islands created in the early stages of the low-temperature deposition. The high step density and the consequent reduction in the island size favorites the jump of the adatoms onto the lower lever over the nucleation on the top of growing islands. This occurs when the island size is smaller than the size of the depleted zone. The determination of the deposition rate in LEEM is performed by evaluation of the area of the growing 2D islands. It is therefore preferable to have a layer-by-layer growth mode. However, the low temperature 2D mode is not indicated, because the dendritic form of the islands introduces great uncertainty in such evaluation. The best situation is therefore at temperatures above 500 K, where the high mobility of the adatoms ensures regular shapes and clear growing fronts.

Fig. 4.1 shows LEEM images of Pt deposition on the Pt(111) sample at 720 K. The surface consisted of large terraces separated by step bunches. The sample was kept not completely clean on purpose; some carbon agglomerates, decorating the atomic steps, were visible as small black dots. The presence of such agglomerates helps to trace the initial position of the atomic steps after the growth, in order to estimate correctly the area covered by the step flow. Their influence on the growth was appreciable only at the initial stages; the steps flew only where not decorated. This indicates a suppression of the Pt nucleation rates on the carbon aggregates. Once the agglomerates were enclosed in the island, the steps recovered a regular shape. Interestingly, at 720 K the surface diffusion was so high that the homoepitaxy assumed mainly the form of step flow, while the creation of new islands was heavily suppressed. The formation of a new step occurred

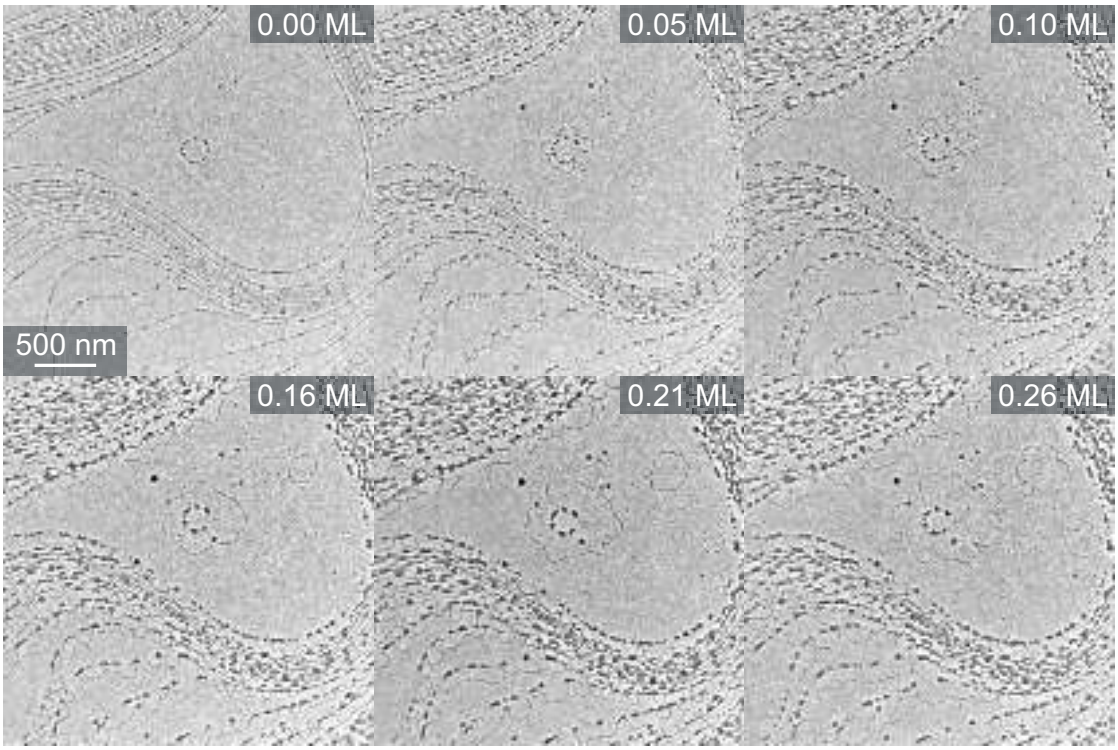

Figure 4.1: Homoepitaxy on Pt(111). The black dots on the atomic steps are carbon agglomerates. The coverage of 0.26 ML has been achieved with a continuous deposition of 46 min at the maximum flux. E_0 = 20 eV.

only if the terrace was larger than $\sim$ 1000 nm. The images analysis reports a maximum Pt deposition rate of 0.005 ML/min, i.e. 1 ML every 3 hours and 16 minutes. This value is very low, compared to the one achieved for the Fe deposition, and is due to the low vapour pressure of Pt when the temperature approaches the melting point (1.90x10^{-7} mbar at 2040 K), combined with the relatively large distance of 20 cm between sample and evaporant rod and the grazing incidence of 20°, corresponding to the flux reduction of a factor of 3.

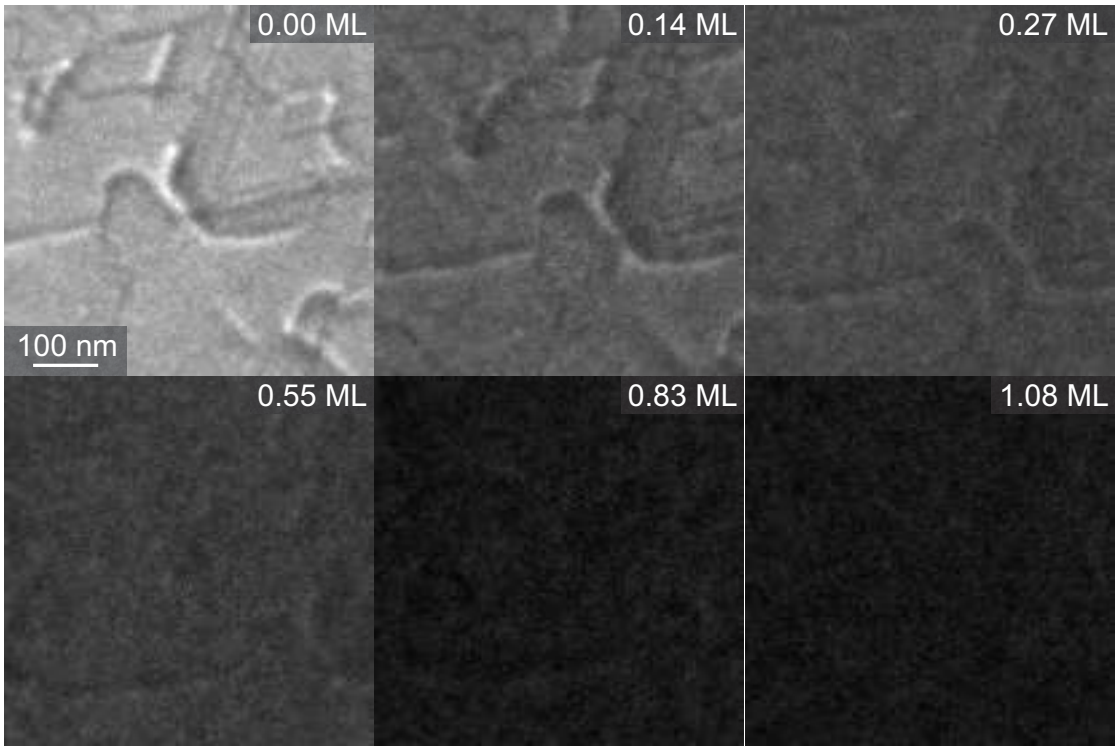

Figure 4.2: Room temperature deposition of Pt on Fe_3O_4(111) thin film. The LEEM image gradually loses contrast due to the small size and low crystallinity of Pt agglomerates. The image intensity scaling was not changed in the figure. Deposition rate 0.005 ML/min, E_0 = 19 eV

4.2 Pt deposition on Fe_3O_4(111) at room temperature

Fe_3O_4(111) film was created on Pt(111) with the preparation described in Chapter 3: the new recipe guarantee the creation of a magnetite film with very large terraces, low step density and some line dislocations. The lens alignment was optimized with the clean Pt(111) surface and then checked at every subsequent step. Single-layer FeO(111) and thick Fe_3O_4(111) films were fully characterized with spectroscopy and diffraction techniques, with the measurement of I/V-LEED, XPEEM images and XPS spectra of the Pt 4f and Fe 3p core levels, as well as the valence band. This database will be useful as a benchmark for the data analysis of the Pt nanoparticles.

4.2.1 Deposition

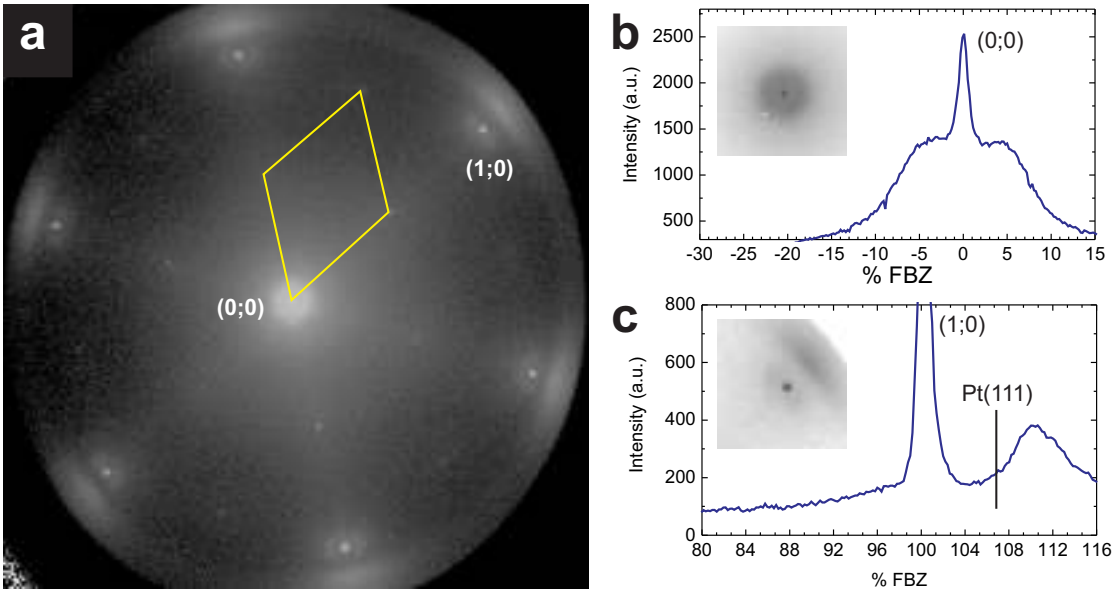

Figure 4.3: (a) LEED pattern of the $Fe_3O_4(111)$ thin film after deposition of 1.08 ML of Pt. The (2x2) structure of $Fe_3O_4(111)$ is highlighted in yellow. $E_0 = 42$ eV. LEED image with inverted contrast and SPA-LEED spectra of the (0;0) (b) and (1;0) (c) spots. The x axis is calibrated with the first Brillouin zone (FBZ) dimension of the (1x1) structure of $Fe_3O_4(111)$. The position of the bulk Pt(111) (1;0) spot is reported.

The deposition of 1.08 ML of Pt, performed at 300 K in UHV, was recorded in real-time in LEEM mode. **Fig. 4.2** shows frames of the LEEM images thus collected; the chosen field of view (1.5 μm) allows a resolution of about 5 nm. The Pt deposition decreases the intensity of the reflected electron beam by 74% and degrades the image sharpness. This is expected for a crystal surface gradually covered by objects too small to be detected with such resolution: the rough morphology or a not perfect crystallization reduced the backscattering of electrons. Additional information can be obtained by LEED analysis (**Fig. 4.3a**). The intensity of the $Fe_3O_4(111)$ spots was decreased whereas the background intensity was strongly increased. Around the (0;0) and the second order spots ((1;0), (0;1) and equivalents) rings are visible. This broadening is associated with small objects with ordered structure. Spot-Profile-Analysis of the (0;0)

LEED spot (**Fig. 4.3b**) demonstrates that the lateral periodicity of such objects is 4.9 nm. SPA-LEED performed on the (1;0) spot along the (1;0) direction (**Fig. 4.3c**) shows also a new broad feature at larger $|k_{||}|$ values. Its position in the LEED pattern is very similar to the (1;0) spot of the Pt(111) single crystal; therefore it is identified as the (1;0) diffraction spot of the PtNP. A more detailed insight on the position of this peak shows that it is centered at 110.4% of the First Brillouin Zone of Fe_3O_4(111), a value 3.0% larger than the one detected for the Pt(111) (107.2%). This denotes that the lattice constant in the PtNP is shorter than the bulk one, i.e. the average interatomic distance is compressed. This can be due to the very small size of the particle, not only in the plane directions but also in the thickness. STM analysis of PtNP[96] show that, for 1.0 ML of Pt deposited at 110 K, a large part of agglomerates consist mainly of one atomic layer. With such configuration, the strain induced by the under-coordination of the atoms and the heteronuclear bond can create great distortions in the crystal geometry.

4.2.2 Annealing at 850 K

As pointed out in Ref. 38, PtNP encapsulation does not occur during the deposition at room temperature, but is activated by annealing at 850 K. The sample was therefore heated up to 850 K with a rate of 4.5 K/s, kept at that temperature for 2 min and finally cooled down. LEEM images were recorded in-real-time every second. A larger field of view (6 μm) was chosen for this image set because of the thermal drift of the sample during the annealing, which blur the images if the magnification is too high. **Fig. 4.4a** shows an image series at different temperatures. Above 400 K the image intensity, i.e. the electron beam reflectivity, rises up fast (**Fig. 4.4b**) until the temperature reaches 610 K, and then slow down gradually to a plateau. This threshold can be interpreted as the completion of nanoparticle sintering and the starting of the encapsulation, in agreement with STM findings[96]. High resolution images of the final surface (**Fig. 4.5a**) at different electron kinetic energy show a partial recovering of the contrast. The Pt nanoparticles cannot be distinguished clearly from the substrate; the granular structure that is barely visible, however, has a spatial periodicity that coincides with the expected particle size ($\sim$ 10 nm). For comparison, a rescaled STM image of the PtNP from Ref. 38 has been inserted in the figure as an inlay. More detailed information came from the LEED pat-

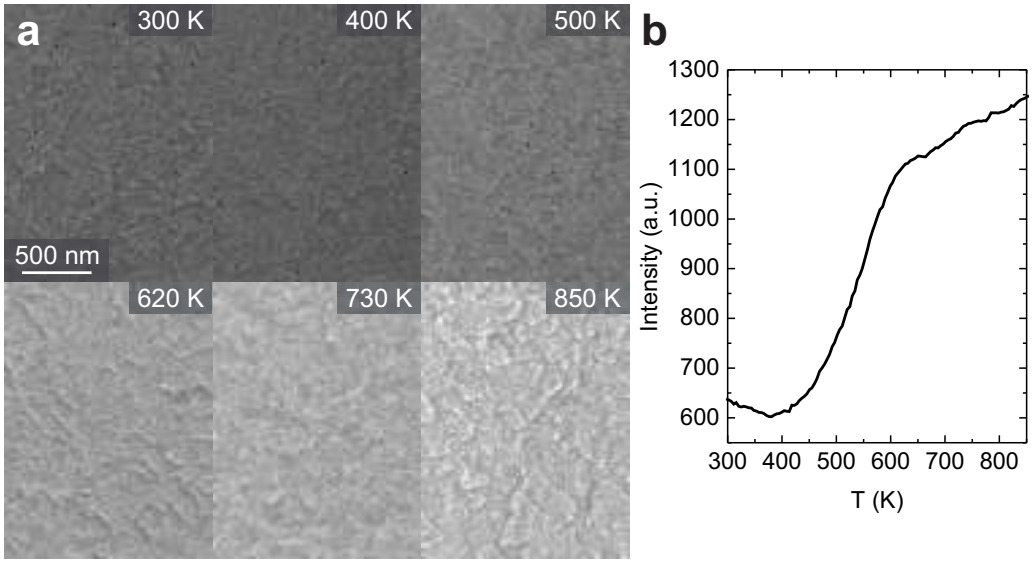

Figure 4.4: (a) LEEM images of the $Fe_3O_4(111)$ surface with 1.08 ML Pt during the annealing. Heating rate 4 K/s, E_0 = 19 eV. (b) LEEM image intensity as function of the temperature.

tern analysis (**Fig. 4.5b**). After the annealing the ring around the elastic and integer diffraction spots gave place to more structured features. SPA-LEED of the (0;0) spot shows the appearance of six very weak satellites (**Fig. 4.5c**). A comparison with the analogous profile taken for a FeO(111) monolayer on Pt(111) bring to the conclusion that the weak spots are the proof of the occurred encapsulation. LEED image analysis and spot profile analysis of the area surrounding the (1;0) spot show as well a new feature that can be ascribed as FeO(111)/Pt(111) (**Fig. 4.5d**). Two very weak lateral peaks stand beside the PtNP peak and can be correlated with the hexagonal structure surrounding the FeO(111) integer spot. The position of the PtNP peak indicates a convergence of the average lattice constant to the bulk value; the lateral lattice expansion is reduced from 3.0% to 1.4%.

4.2.3 XPEEM/XPS

The improved lateral resolution and transmission provided by the aberration corrector make SMART the only spectro-microscope capable to detect in principle single nan-

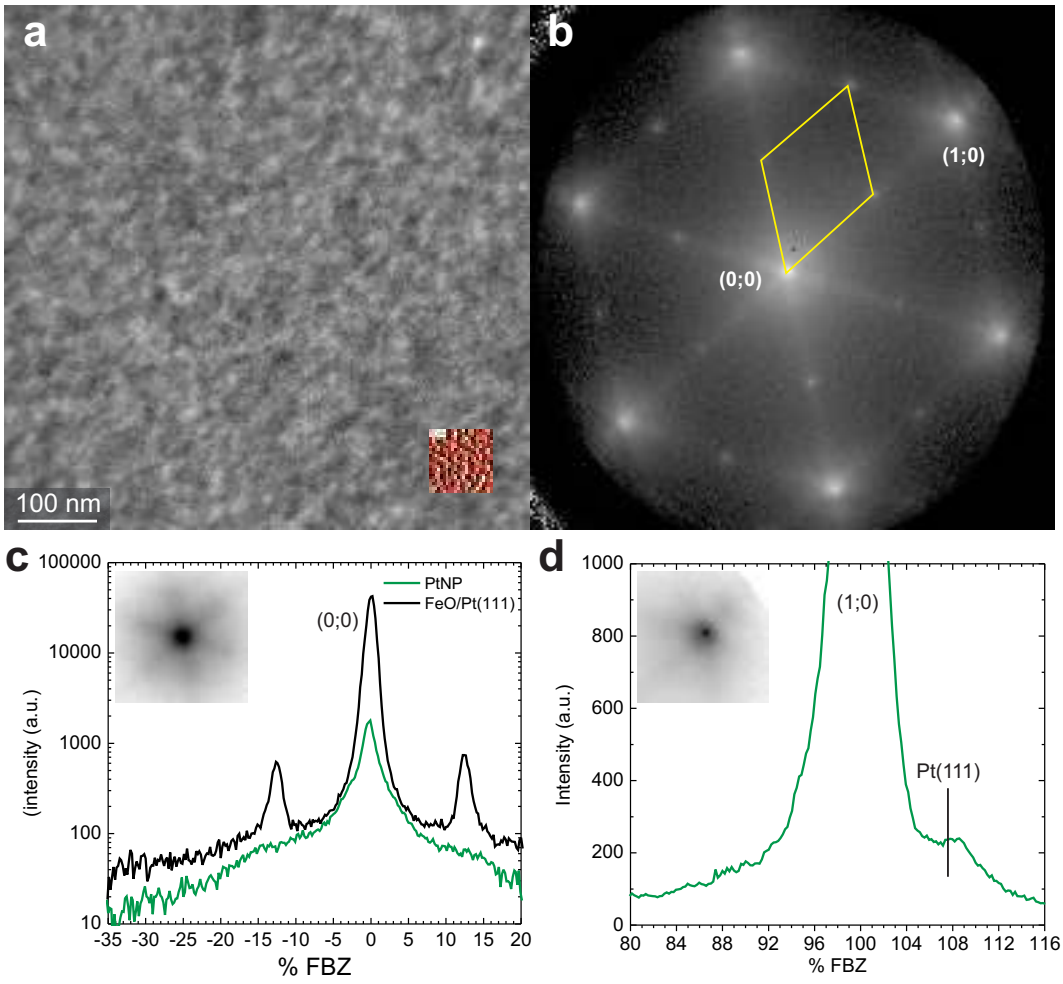

Figure 4.5: LEEM image (a) and corresponding LEED pattern (b) of the Pt nanoparticles on Fe_3O_4(111) thin film. In the inlay is reported a scaled STM image from Ref. 38. The (2x2) structure of Fe_3O_4(111) in LEED is highlighted in yellow. (a) E_0 = 16 eV. (b) E_0 = 38 eV. (c) SPA-LEED profile of the (0;0) spot of Pt nanoparticles, compared with the one from a single layer of FeO(111)/Pt(111). In the inlay is visible the (0;0) spot with inverted contrast. (d) SPA-LEED profile of the (1;0) spot of Pt nanoparticles. The position of the (1;0) spot of bulk Pt(111) is reported. In the inlay the (1;0) spot with inverted contrast is presented.

oclusters, and to perform spectroscopy and diffraction on them. Although it has been demonstrated a lateral resolution of 2.6 nm in LEEM, the space-charge effect reduces considerably the performances in XPEEM. As discussed in Section 1.4, the best lateral resolution achieved in XPEEM is 18 nm, which is still too large for a direct imaging of Pt nanoclusters on $Fe_3O_4(111)$. Typical XPEEM images of homogeneous surfaces, as well as surfaces with corrugations beyond the resolution limit, appear very smooth and with no visible feature. Nonetheless, information on the electronic status of the surface can be obtained via integration of the XPEEM image intensity on a certain range of electron kinetic energy, i.e. extrapolation of XPS spectra from a region controlled in LEEM. XPS spectra have been collected for the Pt 4f and Fe 3p core level, as well as the valence band spectra. The slit at the exit of the Omega-filter provided an energy resolution of 0.5 eV. The photon energy was selected in order to guarantee the maximum image intensity, in agreement with the atomic cross section of the selected lines and the brilliance of the beamline. Optimum values were 210 eV for Pt 4f and 90 eV for the valence band. During the measurement, the temperature of the sample was kept constant at 300 K.

Pt 4f core level emission line spectrum was measured after the Pt deposition, before and after the annealing at 850 K. The results are visible in **Fig. 4.6**, together with the spectra collected from clean Pt(111) surface and when such sample is covered by 1 ML of FeO(111). Every peak was fitted with one single Voigt function, except the Pt(111) with two Gaussian, in order to isolate the surface and bulk components. The energy shifts respect to the bulk component of Pt(111) are presented in the inlay table. Due to the high instrumental broadening ($\sim$ 0.5 eV), it was not possible to verify if the line shape of the other peaks consists of the sum of several components. The surface component of clean Pt(111) has a binding energy lowered by 0.40 eV with respect to the bulk component, in agreement with previous findings[103]. If such surface is covered by FeO, the clean surface component is replaced by an interface component with a positive shift of about 0.2 eV. This is generated by the heteronuclear bond with Fe atoms. In fact, for the used preparation conditions, FeO(111)/Pt(111) consists of a O layer at the surface that rest over a Fe layer at the interface with the Pt substrate[98]. The Pt 4f peaks measured after the Pt deposition at room temperature shows a minor positive shift of about 0.13 eV. Because of the thickness of the Pt aggregates, no components from the

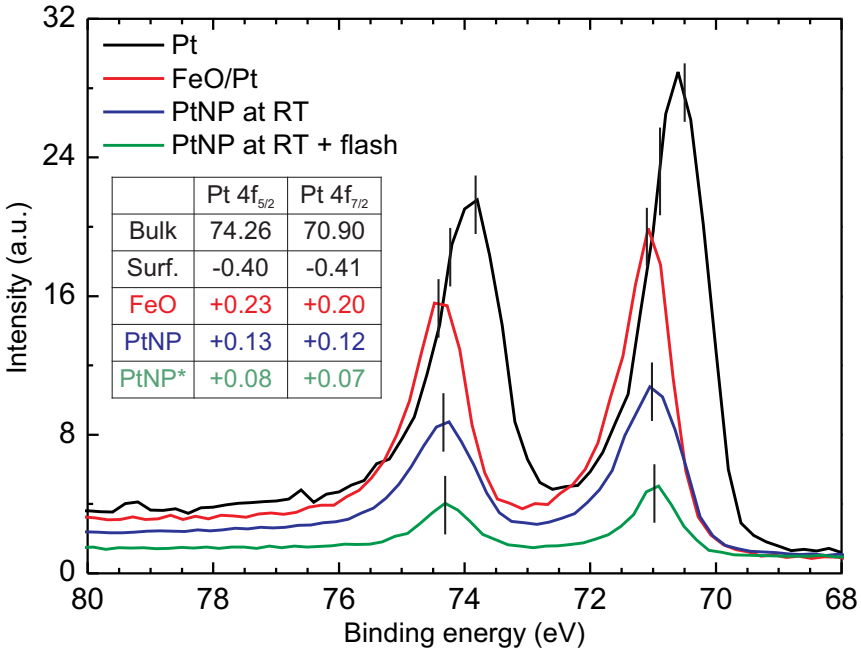

	Pt $4f_{5/2}$	Pt $4f_{7/2}$
Bulk	74.26	70.90
Surf.	-0.40	-0.41
FeO	+0.23	+0.20
PtNP	+0.13	+0.12
PtNP*	+0.08	+0.07

Figure 4.6: XPS spectra of Pt 4f core level for clean Pt(111) (black), single-layer FeO(111)/Pt(111) (red), Pt nanoparticles after deposition at room temperature (blue) and after the annealing (green). The position of the peaks is highlighted with a vertical line. hν = 210 eV.

bulk or from the bulk surface are expected to be visible at the chosen kinetic electron energy, but only the contribution from the Pt atoms at the surface and/or bound with the Fe_3O_4(111) substrate. The encapsulation, driven by subsequent annealing, changes slightly the binding energy of the Pt 4f peaks (the shift is 0.08 eV). Such effect can be related not only to the Fe-Pt bond that occurs in the encapsulation, but also the sintering of Pt nanoparticles, which changes the ratio between mono- and bi-layer agglomerates and create new facets, in which Pt atoms have a different coordination.

An analogous comparison is presented in **Fig. 4.7** for the valence band (VB). The spectra were collected with a contrast aperture of 50 μm inserted (corresponding to an angular spread of $\pm 6.0°$), in order to collect only electrons close to Γ. The VB displayed in the figure regard clean Pt(111) surface, 1 ML FeO(111)/Pt(111), Fe_3O_4(111)/Pt(111),

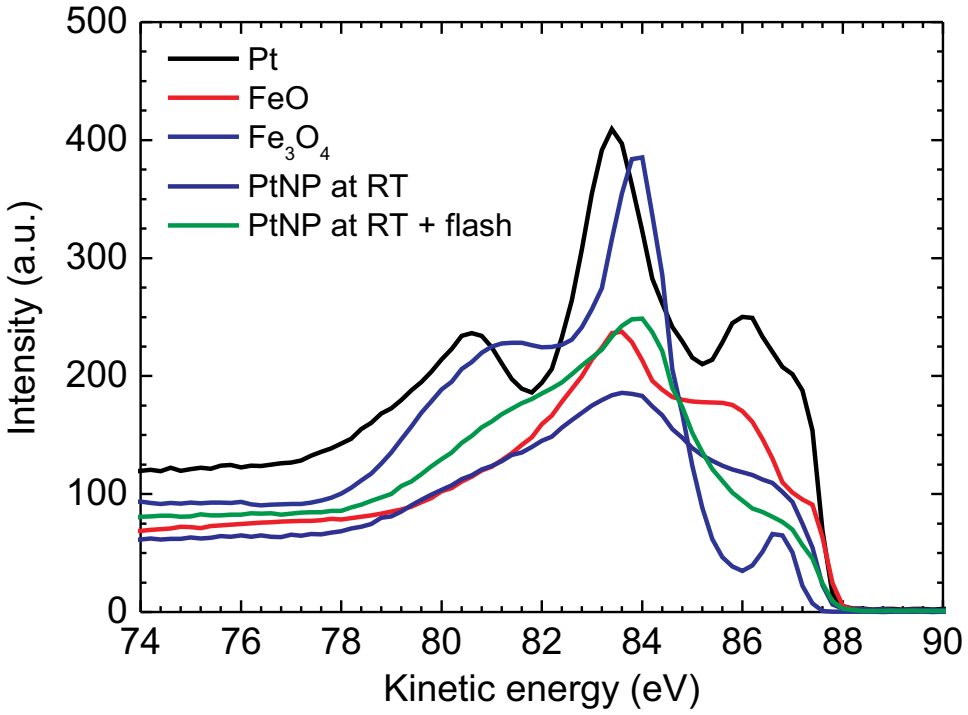

Figure 4.7: XPS spectra of the valence band for clean Pt(111) (black), single-layer FeO(111)/Pt(111) (red), $Fe_3O_4(111)$ thin film (blue) Pt nanoparticles after deposition at room temperature (dark blue) and after the annealing (green). hν = 90 eV.

PtNP freshly deposited at room temperature and annealed at 850 K. The calibration of the Fermi edge position has been made with the clean Pt(111) surface and checked after every preparation step. It can be noticed that $Fe_3O_4(111)$ thin film has no density of states around the Fermi energy in the region surrounding Γ; the VB starts at about 0.4 eV. This is in agreement with the particular half-metallic character of magnetite. The density of states (DOS) around the Fermi energy E_f is dominated by the d electrons of Fe_{oct} ions [104,105]. The VB structure is therefore highly polarized due to the magnetic interaction and can be thought in terms of spin-up ($\uparrow$) band and spin down ($\downarrow$) band, separated by the exchange energy. Due to the symmetry of the possible spatial configuration of Fe_{oct} sites, the five d levels are split in two degenerated t_{2g} levels and two

degenerates e_g levels. The entire majority spin band is below E_f and occupied by five ($\uparrow$) electrons, while the t_{2g} level of the minority spin band is located on E_f and accommodates one ($\downarrow$) electron. The dispersion analysis of the minority spin band (Ref. 106, Fig. 3) shows that, for photon energy between 40 and 80 eV, no states are located close to E_f, while the first experimental feature is located at 0.6 - 0.9 eV. Although the photon energy used in our experiment differs from that range (90 eV), the behavior can be easily extrapolated by noticing the periodicity of the dispersion in function of the photon energy. The features at 0.6 and 4.1 eV are usually associated with Fe d band, while the peak above 6 eV is related with O 2p band. The deposition of 1.08 ML Pt at room temperature changes substantially the VB of the system. New states are created close to E_f and the sharp peak associated with the minority carriers of Fe_3O_4 is overlapped by the contribution of Pt d band. The overall d-band center is shifted towards lower binding energy. The annealing and consequent encapsulation of Pt NP does not change significantly the VB structure; however, a partial depletion in the DOS at binding energies closed to E_f is detected.

4.3 Pt deposition on Fe_3O_4(111) at 700 K

In the experiment seen so far, Pt deposition and encapsulation are performed in two separate stages. The encapsulation occurs when Pt nanoparticles are already formed on the surface; the process, activated by annealing, modifies the structure, the size and the atomic termination of the nanoparticles. Observing in real time the encapsulation via annealing is very difficult: the thermal expansion of the sample and the sample holder causes not only a lateral drift of the sample, making high magnification imaging imappropriate, but also perpendicular expansion of the sample holder, so that the objective lens focus has to be adjusted continuously. It is therefore preferable to have a stable temperature when the spectro-microscope is used at high magnification. For this reason, we studied the deposition of Pt on Fe_3O_4(111) set fixed at 700 K. With this experiment we hoped to see the formation of larger Pt nanoparticles (due to the enhanced mobility of Pt atoms) and to verify if the encapsulation occurs while the deposition takes place.

4.3.1 Deposition

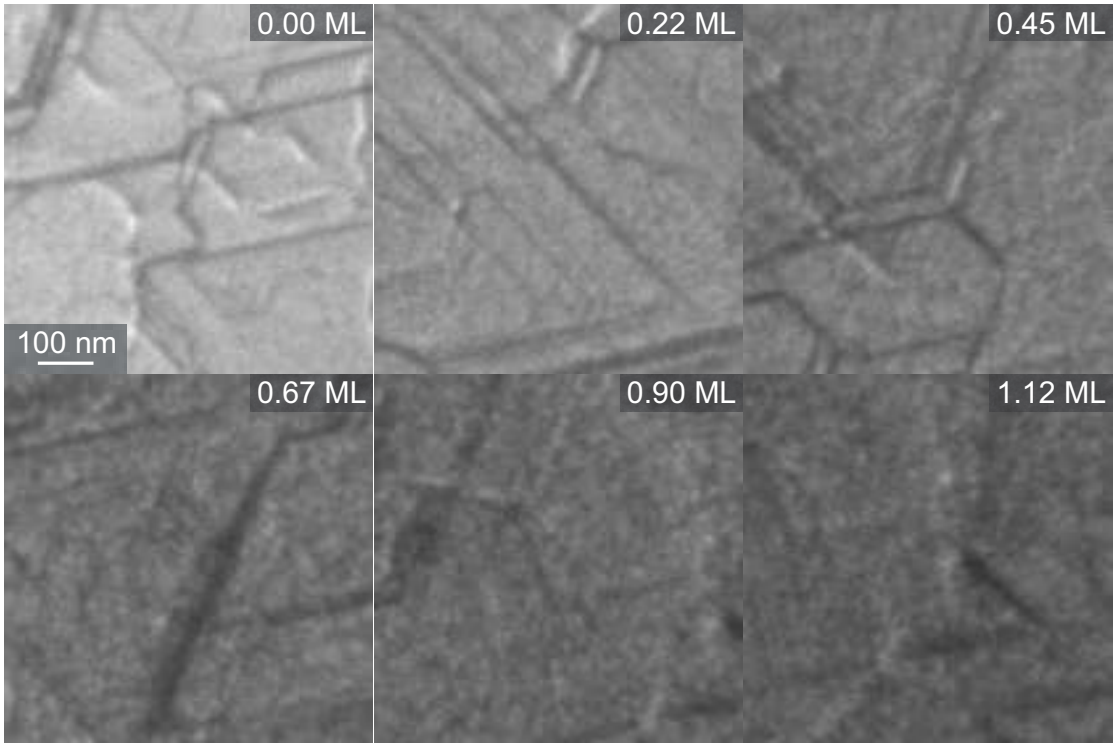

Figure 4.8: LEEM images of deposition of 1.12 ML Pt on $Fe_3O_4(111)$ thin film. The image intensity scaling was not changed in the figure. Deposition rate 0.005 ML/min, E_0 = 29 eV.

In analogy with the previous case, the deposition of 1.12 ML of Pt was recorded in-real-time with LEEM imaging. **Fig. 4.8** presents selected frames of the surface while the deposition occurs. The differences with the deposition at room temperature are evident. After the deposition, the intensity of the electron beam is decreased only by 52% and a decent level of contrast is still maintained. This supports a crystalline order of the deposited material. Surface details as atomic steps and line dislocations are still visible. Moreover, the entire surface is covered by objects up to 20 nm wide (**Fig. 4.9a**). As before, a rescaled STM image of the PtNP from Ref. 38 has been inserted in the figure as an inlay for comparison. From LEEM analysis, it is obvious that Pt deposition at 700 K produces a more ordered surface: the surface details captured with LEEM are more visible than in the case of Pt deposition at room temperature and annealing at 750 K. It

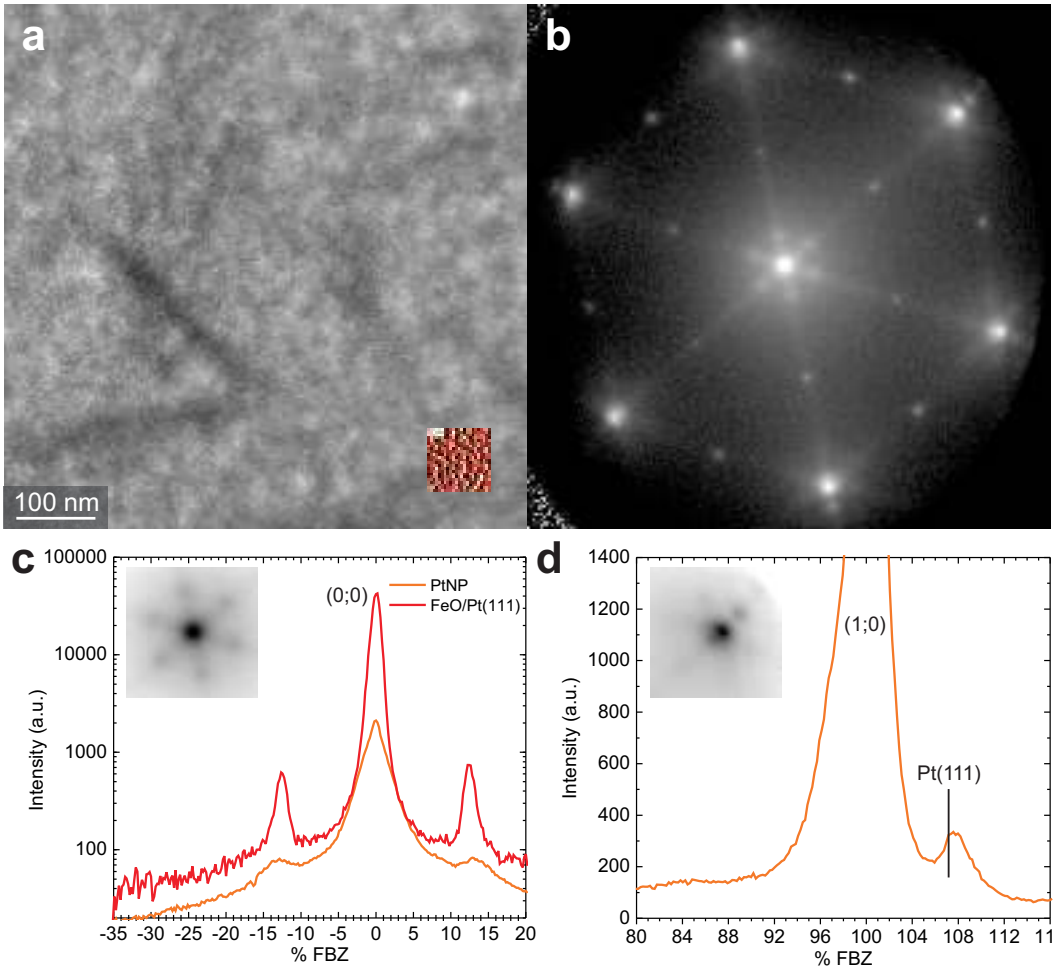

Figure 4.9: LEEM image (a) and corresponding LEED pattern (b) of the Pt nanoparticles on Fe_3O_4(111) thin film. In the inlay is reported a scaled STM image from Ref. 38. (a) E_0 = 16 eV. (b) E_0 = 38 eV. (c) SPA-LEED profile of the (0;0) spot of Pt nanoparticles, compared with the one from a single layer of FeO(111)/Pt(111). In the inlay is visible the (0;0) spot with inverted contrast. (d) SPA-LEED profile of the (1;0) spot of Pt nanoparticles. The position of the (1;0) spot of bulk Pt(111) is reported. In the inlay the (1;0) spot with inverted contrast is presented.

is not possible, however, to distinguish every single nanoparticle present of the surface, due to their mutual proximity. In LEEM imaging, the best conditions to visualize a nanoparticle smaller than 10 nm is when no other particles are around in a radius of at least 30 nm. If this requirement is not fulfilled, the LEEM image displays the surface as uniformly corrugated and cannot differentiate between substrate and nanoparticles. Despite the high temperature and the very low deposition rate (1 ML every three hours), the distance between nanoparticles seems to be too small to allow a clear imaging of every single nanoparticle. It is therefore not possible to perform analysis over the shape and the nucleation site.

LEED analysis provides again more information about the encapsulation status (**Fig. 4.9b**). The appearance of satellite spots around (0;0) and the first-order spots proof the encapsulation. Spot profile analysis of (0;0) and (1;0) spots (**Fig. 4.9c** and d respectively) and comparison with the profiles obtained for FeO(111)/Pt(111) confirm that the PtNP are encapsulated by FeO. It can be noticed that the FeO extra spots are sharper than in the case of Pt nanoparticle created at room temperature and then annealed; this testifies a higher structural order of the system and a larger nanocluster size. The position of the PtNP (1;0) peak reveals a lattice expansion of 0.4% respect to Pt(111), a value smaller than the one detected with the original recipe.

4.3.2 XPEEM/XPS

XPEEM images of the surface in question were collected using Pt 4f core level and VB photo-emitted electrons. The microscope was set with the same parameters of the previous experiment. XPS spectrum of the Pt 4f line is displayed in **Fig. 4.10**; analogous spectra of clean Pt(111) surface and FeO(111)/Pt(111) are shown for comparison. The binding energy shifts with respect to the bulk component of Pt(111) are presented again in the inlay table. The peaks measured after the Pt deposition at 700 K present a positive shift of 0.07 eV, almost identical to the one found for PtNP deposited at room temperature and annealed (0.08 eV). This suggests that the structure of the nanoparticles created at high temperature could be very similar. **Fig. 4.11** shows VB spectrum of the same surface, in comparison with Pt(111), FeO(111)/Pt(111) and PtNP created at room temperature and annealed. Clearly, the different preparation recipe of the nanoparticles

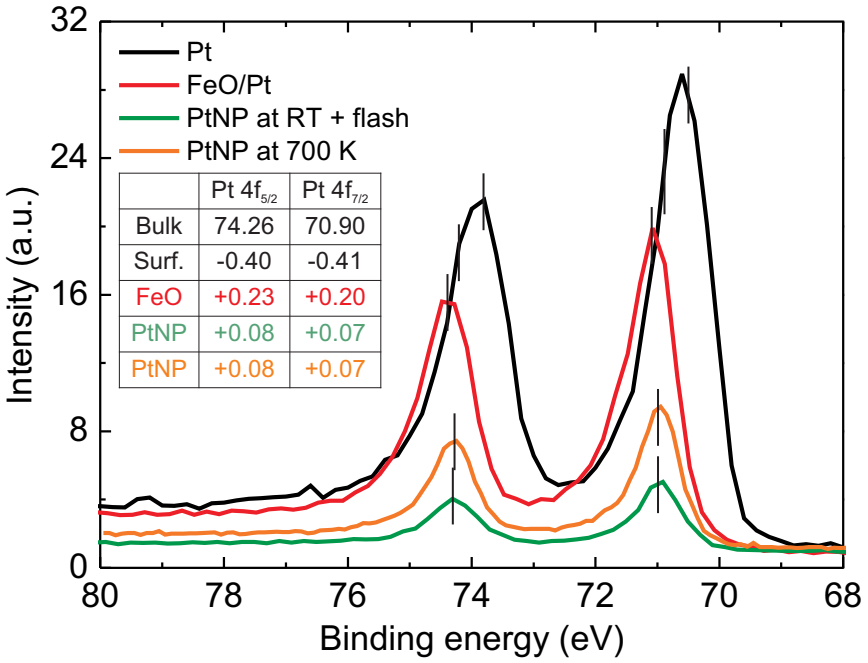

	Pt $4f_{5/2}$	Pt $4f_{7/2}$
Bulk	74.26	70.90
Surf.	-0.40	-0.41
FeO	+0.23	+0.20
PtNP	+0.08	+0.07
PtNP	+0.08	+0.07

Figure 4.10: XPS spectra of Pt 4f core level for clean Pt(111) (black), single-layer FeO(111)/Pt(111) (red), Pt nanoparticles after deposition at room temperature and annealing (green), Pt nanoparticles after deposition at 700 K (orange). The position of the peaks is highlighted with a vertical line. hν = 210 eV.

has no influence in the valence band structure: the spectra are essentially identical, so the considerations about the VB structure taken in the previous case are still valid.

4.4 Discussion

In this experiment, SMART has demonstrated the capability to follow in every step the preparation of highly complex nanostructured surfaces. The combination of microscopy, spectroscopy and diffraction techniques clarify new aspects in the formation of transition-metal nanoparticles via physical vapor deposition and in phenomena such the strong metal-support interaction. Two different preparation recipes have been tested:

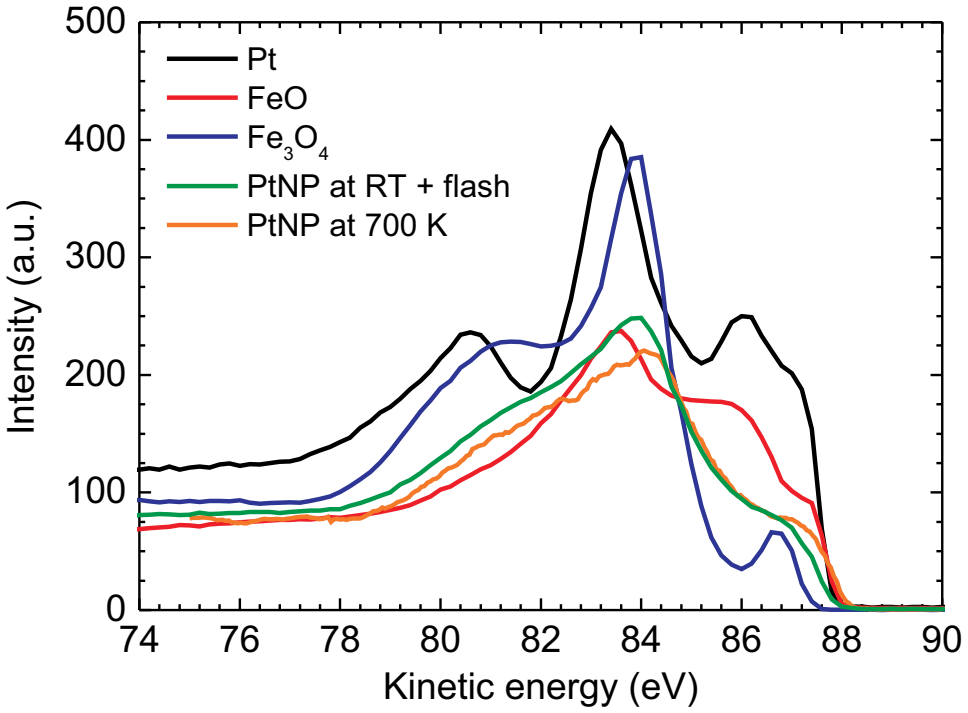

Figure 4.11: XPS spectra of the valence band for clean Pt(111) (black), single-layer FeO(111)/Pt(111) (red), Fe_3O_4(111) thin film (blue), Pt nanoparticles after deposition at room temperature and annealing (green), Pt nanoparticles after deposition at 700 K (orange). hν = 90 eV.

deposition of Pt at room temperature with subsequent annealing at 850 K and deposition of Pt at 700 K. In both cases LEED and XPS proved the occurred encapsulation of Pt nanoparticles by a layer of FeO. The latter preparation method, unpublished before, guarantees a direct encapsulation of the nanoparticles and a change in their morphology. LEEM images show much more details of the surface decorated by encapsulated Pt nanoparticles if the deposition is performed at higher temperature. Higher degree of crystallization can be explained by the different formation mechanism. If the deposition is performed at room temperature, the kinetic energy of the adsorbed atoms is too low to overcome the diffusion activation barrier; this leads to the formation of highly irregular

2D islands[96]. Annealing at 850 K enables, together with the encapsulation, the sintering of the adsorbed material and the creation of nanoparticles via Ostwald ripening, i.e. migration of atoms from smaller to larger particles. If the atoms are deposited at 700 K, the diffusion process enables the direct formation of nanoparticles. In this case, morphological properties such the size and the shape, are depending on the abundance of nucleation centers (point defects, steps. . .), the temperature and the deposition rate. In particular, the deposition rate used in this experiment (1 ML every 3 h) guarantee larger in size and more regular-shaped nanoparticles, as confirmed by LEEM and LEED. Interestingly, both formation processes (ripening versus diffusion and nucleation) lead to the encapsulation of the particles. This can help to figure out more details about the encapsulation mechanism. In principle, the gradient of the surface free energy can drive the material necessary for the skin both from the side and/or through the particle. Pt and Fe are well known to be capable to form alloys; several studies have been performed on FePt at different concentrations, reporting strong interdiffusion above 535 K[107] and segregation of Pt towards the surface on $Pt_{80}Fe_{20}$(111) surface[108]. However, an O spillover onto Pt seems however to be hardly possible, since the affinity of Pt for oxygen is much lower than the one for Fe. Therefore, possible mechanisms for the formation of the encapsulating FeO layer would be the migration of O atoms from the substrate over the nanoparticle surface, or the gradual sinking of the nanoparticle under the first oxygen layer and the rearrangement of Fe atoms from the bulk to form a ”skin” with the right stoichiometry (**Fig. 4.12a**). In this matter, the fact that with deposition of Pt at high temperature the nanoparticles are formed already encapsulated tells that Pt atoms diffusing on the surface are able to pass through the FeO ”membrane” of the already existing nanoparticles, created in the initial stages of the deposition, and enlarge them (**Fig. 4.12b**). This consideration leads to be rather in favor of the segregation process: the migration of Pt atoms through the first oxygen and iron layer of Fe_3O_4(111) seems to be energetically favored. However, this experiment is not exhaustive: more evidences should be collected in order to clarify this aspect with the requested rigor. One possibility would be to have XPEEM images of single nanoparticles: real-time images with chemical sensitivity would be the perfect tool to see in detail the growth stages of the encapsulating layer. Up to now, this kind of experiment cannot be performed: factors like lateral resolution, high acquisition time and thermal drift limit strongly such possibility, even with the unmatched capabilities of SMART.

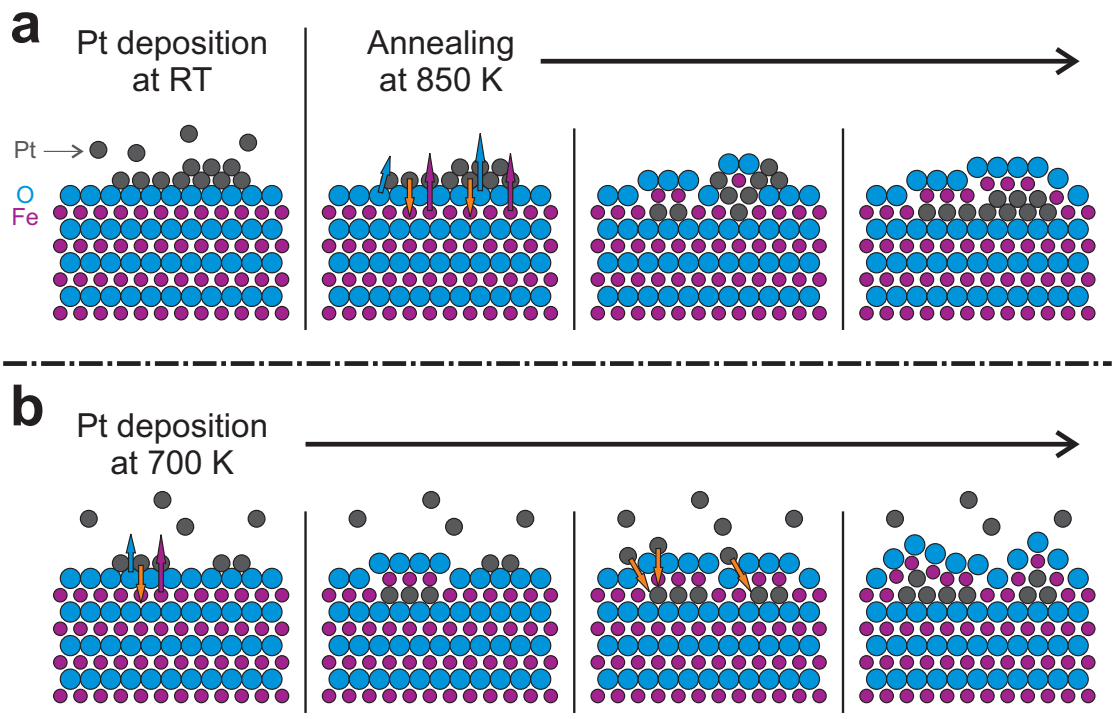

Figure 4.12: Scheme of the FeO encapsulation mechanism for (a) Pt deposited at room temperature and subsequently annealed to 850 K and (b) Pt deposited at 700 K. In (a) the encapsulation is produced during the annealing, in which O and Fe atoms create the encapsulating layer by passing through the nanoparticle. In (b) small nanoparticles are formed on the surface and encapsulated in the pristine stages, then they grow in size by continuous segregation of Pt atoms through the encapsulating membrane.

Chapter 5

Summary and outlook

The aim of this work was a systematic study of model catalysts by applying the powerful capabilities of SMART. Therefore, part of the efforts during my doctorate were directed to improve the usability and the performance of SMART, especially concerning the lateral resolution in XPEEM mode resulting in an improvement of a factor of two. However, tests with ultrathin Au films on W(110) showed the current limitations of the optics: space charge phenomena affected the photo-emitted electrons, limiting the lateral resolution to 18 nm. A complete analysis about the origins and the possible interventions to overcome such effect was discussed. We are confident that this result, which is already the best worldwide for XPEEM, can be further improved in the near future, especially with the updated technical solutions that will be implemented in SMART-II.

The main topic of scientific interest was the characterization of Fe_3O_4(111) thin films. The possibility to test in real-time and *in-situ* the sample during the preparation unveiled several important aspects that are usually hidden to other investigation tools. With this work, it could be clarified how crucial the preparation conditions are for the formation of a high quality magnetite thin film on Pt(111) single crystal. Parameters like oxidation temperature and pressure, annealing temperature and cooling rates produce thin films with different surface properties, which can present inhomogeneities of different nature. In particular, the magnetite thin film showed an anomalous abundance of one rotational domain, with consequent lack of antiphase domain boundaries. Changes in the oxidation temperature led to a de-wetting of the Fe_3O_4(111) thin film, with the formation of deep holes in which the substrate is covered by only an atomically thin FeO(111) film. After the last oxidation step, the cooling in oxygen atmosphere caused the formation of

FeO_x agglomerates a few nanometers wide, which rest upon the canonically-terminated surface. Such objects could be removed only by annealing at 900 K and can explain some discrepancies in the literature findings regarding the surface termination and its catalytic properties.

SMART was extremely useful to show direct effects of changes in the preparation conditions. With this knowledge, a new preparation recipe has been developed, which consists of Fe deposition on a rough $Fe_3O_4(111)$ thin film in oxidation conditions. This new procedure allowed the creation of flatter and more regular $Fe_3O_4(111)$ thin films. Moreover, the consequent activation of layer-by-layer growth mode permitted to consider additional surface features like isolated line defects and a line network, and to study their dynamical behavior during the growth. With the aid of LEEM simulations performed with the Contrast Transfer Function algorithm, it turned out that such defects are subsurface misfit dislocations with different orientation of the Burgers vector, and that their appearance in LEEM is due to the surface distortion induced by the strain field. Moreover, dislocations with Burgers vector perpendicular to the surface participate to the thin film growth: basing on the experimental findings, an atomic model of such growth channel was developed to explain in detail the mechanism. This new investigation method - the conjugation of LEEM simulation and experiment - has revealed itself as a very powerful tool, which can be applied in principle for a great variety of systems and can be used to determine physical quantities inaccessible before. The layer-by-layer growth gave also the possibility to observe directly the evolution of the rotational domains in every stage of the thin film growth. It turned out that the anomalous abundance of one rotational domain is deeply connected with the substrate morphology: the stacking fault is produced mainly with the nucleation of $Fe_3O_4(111)$ over the substrate step bunches. An attempt to give an atomic view of such phenomenon was made. Furthermore, in closed thin films, the rotational domain boundaries showed a motion during the layer-by-layer growth. The reshape of the rotational domains appears to be ruled by a Wulff-like construction and governed by the diffusion of Fe atoms through the boundaries.

After this complete characterization, $Fe_3O_4(111)$ has been used as support for Pt nanoparticles. Again, different preparation recipes were tested in real-time and *in-situ*. This approach brought new insight into particular phenomena such the strong metal-support

interaction and the encapsulation of Pt nanoparticles by a FeO monolayer. In particular, the nanoparticle formation was studied at different deposition temperatures and the properties of the final system were analyzed. The nanoparticles formation was displayed in real-time in LEEM with unmatched precision for this kind of technique. A comparison between microscopy, spectroscopy and diffraction results suggested that the encapsulation mechanism could be the progressive sinking of the deposited material under the first oxygen layer of the bulk.

Bibliography

[1] R. Fink, M.R. Weiss, E. Umbach, D. Preikszas, H. Rose, R. Spehr, P. Hartel, W. Engel, R. Degenhardt, R. Wichtendahl, H. Kuhlenbeck, W. Erlebach, K. Ihmann, R. Schlögl, H.-J. Freund, A.M. Bradshaw, G. Lilienkamp, Th. Schmidt, E. Bauer, G. Benner, J. Elec. Spec. Rel. Phen. **84**, 231 (1997)

[2] H. Rose, D. Preikszas, Optik **92**, 31 (1992)

[3] S. Lanio, H. Rose, D. Krahl, Optik **73**, 56 (1986)

[4] H. Marchetto, PhD Thesis, Freie Universität Berlin (2006)

[5] O. Scherzer, Z. Phys. **101**, 593 (1936)

[6] Th. Schmidt, U. Groh, R. Fink, E. Umbach, O. Schaff, W. Engel, B. Richter, H. Kuhlenbeck, R. Schlögl, H.-J. Freund, A. M. Bradshaw, D. Preikszas, P. Hartel, R. Spehr, H. Rose, G Lilienkamp, E. Bauer, G. Benner, Surf. Rev. Lett. **9**, 223 (2002)

[7] E. Bauer, Ultramicroscopy **17**, 51 (1985)

[8] M. Lenc, I. Mullerova, Ultramicroscopy **41**, 411 (1992)

[9] G. F. Rempfer, W. P. Skoczylas, O. H. Griffith, Ultramicroscopy **36**, 196 (1991)

[10] R. Tromp, Ultramicroscopy **111**, 273 (2011)

[11] Th. Schmidt, H. Marchetto, P. Lévesque, U. Groh, F. Maier, D. Preikszas, P. Har-

tel, R. Spehr, G. Lilienkamp, W. Engel, R. Fink, E. Bauer, H. Rose, E. Umbach, H.-J. Freund, Ultramicroscopy **110**, 1358 (2010)

[12] S. M. Schramm, A. B. Pang, M. S. Altman, R. M. Tromp, Ultramicroscopy **115**, 88 (2012)

[13] X. J. Zhou, B. Wannberg, W. L. Yang, V. Brouet, Z. Sun, J. F. Douglas, D. Dessau, Z. Hussain, Z. X. Shen, J. Elec. Spec. Rel. Phen. **142**, 27 (2005)

[14] G. A. Massey, IEEE J. Quantum Elec. **19**, 873 (1983)

[15] L. Gregoratti, T. O. Mentes, A. Locatelli, M. Kiskinova, J. Elec. Spec. Rel. Phen. **170**, 13 (2009)

[16] A. Locatelli, T. O. Mentes, M. A. Nino, E. Bauer, Ultramicroscopy **111**, 1447 (2011)

[17] G. A. Massey, M. D. Jones, B. P. Plummer, J. App. Phys. **52**, 3780 (1981)

[18] J. C. Lovgren, G. A. Massey, Microscopy and Microanalysis **3**, 214 (1997)

[19] T. Schmidt, S. Heun, J. Slezak, J. Diaz, K.C. Prince, G. Lilienkamp, E.D. Bauer, Surf. Rev. Lett. **5**, 1287 (1998)

[20] E. Bauer, private communication (LEEMPEEM5, Heimeji 2005)

[21] R. Cornell, U. Schwertmann, "The Iron Oxides", Wiley and Sons, New York (1997)

[22] K. Kato, S. Iida, J. Phys. Soc. Jpn. **51**, 1335 (1982)

[23] M. I. Katsnelson, V. Y. Irkhin, L. Chioncel, A. I. Lichtenstein, R. A. de Groot, Rev. Mod. Phys. **80**, 315 (2008)

[24] E. Verwey, Nature (London) **144**, 327 (1939)

[25] Z. Zhang, S. Satpathy. Phys. Rev. B **44**, 13319 (1991)

[26] W. Eerenstein, T. T. M. Palstra, S. S. Saxena, T. Hibma, Phys. Rev. Lett. **88**, 247204 (2002)

[27] J. J. Versluijs, M. A. Bari, J. M. D. Coey, Phys. Rev. Lett. **87**, 026601 (2001)

[28] R. Schlögl, in G. Ertl, H. Knözinger, J.Weitkamp, ”Handbook of Heterogeneous Catalysis”, Wiley-VCH, New York (1997)

[29] G. Ertl, in J. R. Jennings, ”Catalytic Ammonia Synthesis: Fundamentals and Practice, Fundamental and Applied Catalysis”, Plenum Press, New York (1991)

[30] G. Ertl, J. Vac. Sci. Technol. A **1**, 1247 (1983)

[31] W. Weiss, W. Ranke, Prog. Surf. Sci. **70**, 1 (2002)

[32] A. Barbieri, W. Weiss, M. A. Van Hove, G. A. Somorjai, Surf. Sci. **302**, 259 (1994)

[33] M. Ritter, W. Weiss, Surf. Sci. **432**, 81 (1999)

[34] C. Lemire, R. Meyer, V. E. Henrich, Sh. Shaikhutdinov, H.-J. Freund, Surf. Sci. **572**, 259 (2004)

[35] N.G. Condon, F. M. Leibsle, T. Parker, A. R. Lennie, D. J. Vaughan, G. Thornton, Phys. Rev. B **55**, 15885 (1997)

[36] Sh. Shaikhutdinov, M. Ritter, X.-G. Wang, H. Over, W. Weiss, Phys. Rev. B **60**, 11062 (1999)

[37] I. V. Shvets, N. Berdunov, G. Mariotto, S. Murphy, Europhys. Lett. **63**, 867 (2003)

[38] Z.-H. Qin, M. Lewandowski, Y.-N. Sun, Sh. Shaikutdinov, H.-J. Freund, J. Phys. Chem. C **112**, 10209 (2008)

[39] W. Weiss, M. Ritter, Phys. Rev. B **59**, 5209 (1999)

[40] Th. Schmidt, E. Bauer, Phys. Rev. B **62**, 15815 (2000)

[41] G. Meyer, M. Michailov, M. Henzler, Surf. Sci. **202**, 125 (1988)

[42] B. Santos, E. Loginova, A. Mascaraque, A. K. Schmid, K. F. McCarty, J. de la Figuera, J. Phys.: Condens. Matter **21**, 314011 (2009)

[43] D. I. Jerdev, B. E. Koel, Surf. Sci. **513**, L391 (2002)

[44] M. Ritter, W. Ranke, W. Weiss, Phys. Rev. B **57**, 7240 (1998)

[45] W. Ranke, M. Ritter, W. Weiss, Phys. Rev. B **60**, 1527 (1999)

[46] N. G. Condon, F. M. Leibsle, A. R. Lennie, P. W. Murray, D. J. Vaughan, G. Thornton, Phys. Rev. Lett **75**, 1961 (1995)

[47] M. Paul, M. Sing, R. Claessen, D. Schrupp, V. A. M. Brabers, Phys. Rev. B **76**, 075412 (2007)

[48] V. V. Roddatis, D. S. Su, C. Kuhrs, W. Ranke, R. Schlögl, Thin Solid Films **396**, 78 (2001)

[49] M. Bäumer, D. Cappus, H. Kuhlenbeck, H.-J. Freund, G. Wilhelmi, A. Brodde, H. Neddermeyer, Surf. Sci. **253**, 116 (1991)

[50] J. Wollschläger, D. Erdös, H. Goldbach, R. Höpken, K. M.Schröder, Thin Solid Films **400**, 1 (2001)

[51] K. Kochlöfl, in G. Ertl, H. Knözinger, J.Weitkamp, "Handbook of Heterogeneous Catalysis", Wiley-VCH, New York (1997)

[52] S. Shaikhutdinov, W. Weiss, J. Mol. Cat. A **158**, 129 (2000)

[53] J. B. Pendry, J. Phys. C: Solid St. Phys, **13**. 937 (1980)

[54] M. A. Van Hove, http://www.ap.cityu.edu.hk/personal-website/Van-Hove_files/leed/leedpack.html

[55] R. Pentcheva, W. Moritz, J. Rundgren, S. Frank, D. Schrupp, M. Scheffler, Surface Science **602**, 1299 (2008)

[56] L. Zhu, K. L. Yao, Z. L. Liu, Phys. Rev. B **74**, 035409 (2006)

[57] M. S. Altman, W. F. Chung, Z. Q. He, H. C. Poon, S. Y. Tong, App. Surf. Sci. **169-170**, 82 (2001)

[58] W. F. Chung, M. S. Altman, Ultramicroscopy **74**, 237 (1998)

[59] L. D. Landau, E. M. Lifshitz, "Theory of Elasticity", Pergamon Press, London (1986)

[60] Op de Beeck, M. Dyck, D. V. Coene, Ultramicroscopy **64**, 167 (1996)

[61] J. C. H. Spence, ”High Resolution Electron Microscopy” third ed., Oxford University Press, Oxford (2003)

[62] M. S. Altman, W. F. Chung, C. H. Liu, Surf. Rev. Lett. **5**, 1129 (1998)

[63] A. B. Pang, Th. Müller, M. S. Altman, E. Bauer, J. Phys.: Condens. Matter, **21**, 314006 (2009)

[64] S. M. Kennedy, N. E. Schofield, D. M. Paganin, D. E. Jesson, Surf. Rev. Lett. **16**, 855 (2009)

[65] R. P. Yu, S. M Kennedy, D. M. Paganin, D. E. Jesson, Micron **41**, 232 (2010)

[66] G. Rempfer, O. H. Griffith, Ultramicroscopy **47**, 35 (1992)

[67] J. H. Van der Merwe, F. C. Frank, Proc. Phys. Soc. **7**, 239 (1949)

[68] J. W. Matthews, A. E. Blakeslee, J. Cryst. Growth **27**, 118 (1974)

[69] K. A. Jackson, ”Kinetic Processes”, Wiley-VCH Verlag GmbH, Weinheim, (2004)

[70] P. Hirth, J. Lothe, ”Theory of Dislocations”, McGrawhill, New York (1985)

[71] G. Springholz, Appl. Surf. Sci. **112**, 12 (1997)

[72] J. G. Zheng, G. E. Sterbinsky, J. Cheng, B. W. Wessels., J. Vac. Sci. Technol. **25**, 1520 (2007)

[73] M. Luysberg, R. G. S. Sofin, S. K. Arora, I. V. Shvets, Phys. Rev. B **80**, 024111 (2009)

[74] D. T. Margulies, F. T. Parker, F. E. Spada, R. S. Goldman, J. Li, R. Sinclair, A. E. Berkowitz, Phys. Rev. B **53**, 9175 (1996)

[75] D. T. Margulies, F. T. Parker, M. L. Rudee, F. E. Spada, J. N. Chapman, P. R. Aitchison, A. E. Berkowitz, Phys. Rev. Lett **79**, 5162 (1997)

[76] W. Eerenstein, T. T. M. Palstra, T. Hibma, S. Celotto, Phys. Rev. B **66**, 201101(R) (2002)

[77] M. L. Rudee, D. T. Margulies, A. E. Berkowitz, Microsc. Microanal. **3**, 126 (1997)

[78] F. C. Voogt, T. T. M. Palstra, L. Niesen, O. C. Rogojanu, M. A. James, T. Hibma, Phys. Rev. B **57**, R8107 (1998)

[79] T. Hibma, F. C. Voogt, L. Niesen, P. A. A. van der Heijden, W. J. M. de Jonge, J. J. T. M. Donkers, P. J. van der Zaag, J. App. Phys. **85**, 5291 (1999)

[80] W. Eerenstein, T. T. M. Palstra, T. Hibma, S. Celotto, Phys. Rev. B **68**, 014428 (2003)

[81] A. M. Bataille, L. Ponson, S. Gota, L. Barbier, D. Bonamy, M. Gautier-Soyer, C. Gatel, E. Snoeck, Phys. Rev. B **74**, 155438 (2006)

[82] R. G. S. Son, S. K. Arora, I. V. Shvets, Phys. Rev. B **83**, 133416 (2011)

[83] G. S. Parkinson, T. A. Ma. Z. Novotny, P. T. Sprunger, R. L Kurtz, M. Schmid, D. S. Sholl, U. Diebold, Phys. Rev. B **85**, 195450 (2012)

[84] M. Bäumer, H. J. Freund., Prog. Surf. Sci. **61**, 127 (1999)

[85] S. Stempel, M. Bäumer, H. J. Freund, Surf. Sci. **402-404**, 424 (1998)

[86] K.Højrup Hansen, T. Worren, S. Stempel, E. Lægsgaard, M. Bäumer, H.-J. Freund, F. Besenbacher, I. Stensgaard, Phys. Rev. Lett. **83**, 4120 (1999)

[87] W. L. Ling, N. C. Bartelt, K. F. McCarty, C. B. Carter, Phys. Rev. Lett. **95**, 166105 (2005)

[88] C. Busse, T. Michely, Surf. Sci. **552**, 281 (2004)

[89] H.-J. Freund, Surf. Sci. **500**, 271 (2002)

[90] Q. Fu, Th. Wagner, Surf. Sci. Rep. **62**, 431 (2007)

[91] T. Schalow, M. Laurin, B. Brandt, S. Schauermann, S. Guimond, H. Kuhlenbeck, D. E. Starr, S. K. Shaikhutdinov, J. Libuda, H.-J. Freund 2005, Angew. Chem. Int. Ed. **44**, 7601 (2005)

[92] S. J. Tauster, S. C. Fung, R. L. Garten, J. Am. Chem. Soc. **100**, 170 (1978)

[93] S. J. Tauster, S. C. Fung, R. T. K. Baker, Science **211**, 1121 (1981)

[94] S. J. Tauster, Acc. Chem. Res. **20**, 389 (1987)

[95] H. Knözinger, E. Taglauer. in G. Ertl, H. Knözinger, J.Weitkamp, "Handbook of Heterogeneous Catalysis", **2.4.7**, p. 555, Wiley-VCH, New York (1997)

[96] Z.-H. Qin, M. Lewandowski, Y.-N. Sun, Sh. Shaikhutdinov, H.-J. Freund, J. Phys.: Condens. Matter **21**, 134019 (2008)

[97] Y.-N. Sun, Z.-H. Qin, M. Lewandowski, Sh. Shaikhutdinov, H.-J. Freund, Surf. Sci. **603**, 3099 (2009)

[98] M. Lewandowski, Y.-N. Sun, Z.-H. Qin, Sh. Shaikhutdinov, H.-J. Freund, Appl. Catal A **391**, 407 (2011)

[99] Y.-N. Sun, Z.-H. Qin, M. Lewandowski, E. Carrasco, M. Sterrer, Sh. Shaikhutdinov, H.-J. Freund, J. Catal. **266**, 359 (2009)

[100] R. Kunkel, B. Poelsma, L. K. Verheij, G. Cosma, Phys. Rev. Lett. **65**, 733 (1990)

[101] M. Bott, T. Micheley, G. Comsa, Surf. Sci. **272**, 161 (1991)

[102] Th. Schmidt, PhD thesis, Universität Hannover (1994)

[103] L. Bianchettin, A. Baraldi, S. de Gironcoli, E. Vesselli, S. Lizzit, L. Petaccia, G. Comelli, R. Rosei, J. Chem. Phys. **128**, 114706 (2008)

[104] Yu. S. Dedkov, M. Fonin, D. V. Vyalikh, J. O. Hauch, S. L. Molodtsov, U. Ruediger, G. Guentherodt, Phys. Rev. B **70**, 073405 (2004)

[105] V. I. Anisimov, I. S. Elfimov, N. Hamada, K. Terakura, Phys. Rev. B **54**, 4387 (1996)

[106] Y. Q. Cai, M. Ritter, W. Weiss, A. M. Bradshaw, Phys. Rev. B **58**, 5043 (1998)

[107] N. Zotov, J. Feydt, A. Savan, A. Ludwig, J. Appl. Phys. **100**, 073517 (2006)

[108] P. Beccat, Y. Gauthier, R. Baudoing-Savois, J. C. Bertolini, Surf. Sci. **238**, 105 (1990)

List of publications

A. Sala, H. Marchetto, Z.-H. Qin, S. Shaikhutdinov, Th. Schmidt, H.-J. Freund, *Defects and inhomogeneities in Fe_3O_4(111) thin lm growth on Pt(111)*, Phys. Rev. B **86**, 155430 (2012)

Th. Schmidt, A. Sala, H. Marchetto, E. Umbach, H.-J. Freund, *First experimental proof for aberration correction in XPEEM: Resolution, transmission enhancement, and limitation by space charge effects*, Ultramicroscopy **126**, 23 (2013)

Curriculum Vitae

Der Lebenslauf ist in der Online-Version aus Grnden des Datenschutzes nicht enthalten